Passivation characterisation of poly-Si based passivating contacts

Investigating the benefits of pinhole-enhanced passivation and a new method to extract metal-induced recombination

Remon Gram

TU Delft

Passivation characterisation of poly-Si based passivating contacts

Investigating the benefits of pinhole-enhanced passivation and a new method to extract metal-induced recombination

by

Remon Gram

to obtain the degree of Master of Science
at the Delft University of Technology,
to be defended publicly on Tuesday November 19, 2021 at 14:00 AM.

Student number:	4354915	
Project duration:	February 1, 2021 – November 19, 2021	
Thesis committee:	Prof. dr. ir. Olindo Isabella,	TU Delft | ESE-PVMD | Supervisor
	Dr. Guangtao Yang,	TU Delft | ESE-PVMD | Daily supervisor
	Dr. Amarante Böttger	TU Delft | 3mE-MSE | Professor
	Dr. Ivan Gordon,	IMEC | External

TU Delft

Preface

This thesis has originated from my deep interest in solar cell technologies. The greatest challenge for scientists in this field is to continue improving this technology and aim for the most efficient conversion of energy to fuel our future. It was my goal to gain understanding in this field and contribute to the optimization of solar cell technology. In order to achieve this, I needed all of my available knowledge, patience and energy, which were fueled by my motivation and curiosity.

Remon Gram
Delft, November 2021

Acknowledgements

My greatest thanks will go out to Dr. Guangtao Yang, which has guided me through my thesis project. I could always fall back on his expertise and ability to adapt. Since this adaptation was needed many times during the thesis, Guangtao helped me to achieve this finalization of the thesis project. In between the hard working days, there was also room for some fun and jokes, creating a safe and relaxed atmosphere.

Also many thanks to Dr. Olindo Isabella, who created the opportunity for me to perform my thesis within the PVMD group, while also supervising my thesis work. He opened my eyes on how to look at scientific work and create opportunities therein.
I want to thank my fellow group members from PVMD, which have provided me with a load of knowledge on photovoltaic technologies. By sharing our knowledge we can reach great heights in our field of research.

I could not have performed any experimental work in this thesis without the support and training from the Else Kooi Laboratory and all the employees. It was a pleasure to (temporarily) be a part of you, there is no place where I have learned more than in the lab. Special thanks to the PVMD technicians working in EKL, which were always around when the equipment was not working properly.

Final thanks to my parents and Esmé, which have supported me throughout my thesis. Because of them, I never gave up on my goals and put 200% in this thesis project. I could always come to them for advice and share my experiences.

Abstract

To meet the rapidly increasing global demand for energy, the potential of solar energy is being exploited towards its maximum capacity. The invention of poly-Si based passivating contacts has created an opportunity for c-Si solar cells to reach conversion efficiencies above 25%, while keeping the processing sequence relatively simple. Based on ultra-thin SiO_x and highly doped poly-Si, this contact structure combines chemical passivation with field-effect passivation to enhance the c-Si surface passivation. Ever since 2016, the carrier transport mechanism through pinholes in the SiO_x has been investigated, showing that the pinholes can aid in achieving a low contact resistivity (ρ_c) while maintaining a low recombination (J_0). In this work, the presence of pinholes and their impact on the passivation quality in poly-Si passivating contacts is investigated. Additionally, a method is explored to extract the metal-induced recombination ($J_{0,metal}$), without the need for fabricating a solar cell structure.

The pinhole detection was performed by creating etch pits at the pinhole site by anisotropic TMAH etching. This enlargement has led to the visualization of pinholes in the SiO_x, where the etch time was crucial for an accurate pinhole density measurement. The experiment involved flat samples with thermal oxide and LPCVD a-Si:H, which were annealed at 1000-1075^{o}C. The experimental results have shown an exponential increase of the pinhole density for increasing annealing temperature, with pinhole densities ranging from 10^6 to $2{\cdot}10^8$ cm^{-2}.

To investigate the passivation quality of poly-Si passivating contacts, two annealing treatments, before and after dopant implantation, were explored. The impact of pre-annealing before dopant implantation on the passivation quality in poly-Si based passivating contacts was investigated for textured symmetrical contacts with thermal oxide and LPCVD poly-Si, which are hydrogenated with SiN_x and FGA. A wide range of post-annealing conditions were compared by their thermal diffusion budget. For both n- and p-type contacts, pre-annealing has shown to improve the passivation quality in poly-Si passivating contacts. For the n-type contacts, the pre-annealing temperature (e.g. pinhole density) showed to impact the passivation quality, resulting in the best passivation after 1000-1025^{o}C pre-annealing, combined with a wide range (850-950^{o}C) of post-annealing conditions. Passivation degradation was only visible for 1075^{o}C pre-annealing (high pinhole density) and 1000^{o}C post-annealing (high thermal diffusion budget). The large difference in passivation quality when introducing a pre-annealing treatment can be explained by the enhanced field-effect passivation at the c-Si surface. It is proposed that local in-diffusion of phosphorus occurs through the pinholes, creating an increased internal electric field at the c-Si surface region surrounding the pinhole sites. This field will attract majority carriers, while repelling minority carriers from the highly defective pinhole sites.

In p-type contacts, the pre-annealing temperature did not show to significantly impact the passivation quality. The role of the thermal diffusion budget has shown to be extremely dominant, determining the passivation quality of the p-type contacts. ECV measurements have confirmed the excessive diffusion of boron into the c-Si, which limits the overall passivation quality. The pinhole density does not influence this in-diffusion, showing that the boron diffuses easily through the SiO_x layer. Experimental results have shown that the passivation of the p-type contacts degrades when the thermal diffusion budget exceeds $6{\cdot}10^{-12}$ cm^2. To be able to observe a larger impact of pinholes in p-type contacts, the boron diffusion into the c-Si should be limited.

By varying the metal fraction on symmetrically fabricated poly-Si based passivating contact structures, $J_{0,metal}$ has been extracted with photoconductance lifetime measurements. Exploring this new type of $J_{0,metal}$ extraction has revealed several pitfalls, which should be mitigated to be able to use this method to characterise $J_{0,metal}$ in poly-Si based contacts. Uniformity and reproducibility of the sample passivation are crucial in the extension of experimental investigations into $J_{0,metal}$. Using several identical samples and a precise determination of the metal fraction will minimize the uncertainty of the calculation, approaching the actual value of $J_{0,metal}$ as much as possible. In this study, the metal has shown to influence the photoconductance lifetime measurement, so determination of $J_{0,metal}$ is believed to be most accurate after removing the metal.

Contents

1

Introduction

In the search for increasingly effective sources of renewable energy, abundant solar energy plays a major role as renewable energy source. As the world population continues to grow, so does the world's energy demand. The sudden COVID-19 pandemic has halted this continuous trend in increasing energy demand, but it is expected that this trend will return to its original state at the end of 2021 [1]. As fossil fuel supplies are running out and governments are moving towards a higher renewable energy input, the demand for high efficient renewable energy sources becomes very important for the development of the international society.
Since the invention of silicon solar cells, this technology has dominated the solar energy market. At first, this market was almost completely occupied by multi-crystalline silicon solar cells (Figure 1.1), because of its cheap and easy production. Mono-crystalline silicon yielded much higher conversion efficiencies, so as the price per W_p decreased, mono-crystalline technology became the dominant technology, leaving the multi-crystalline production behind [2].

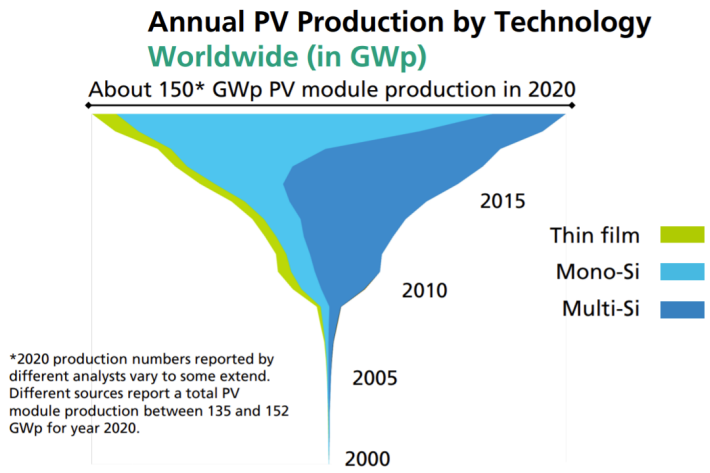

Figure 1.1: Annual PV production per solar cell technology [2].

Ever since photovoltaic technology has been commercialised, competition for the most efficient energy conversion has boosted the development of this technology. The 21^{st} century has been the time where renewable PV became affordable for households, but also where a 'green policy' has boosted companies to install large quantities of PV modules. These modules take up a large area, so the demand for increasingly more efficient PV technology is growing.
Many different concepts of photovoltaic technology have driven up the maximum achieved conversion efficiency of c-Si solar cells. Heterojunctions and TOPCon (tunnel oxide passivated contact) are the most promising technologies, already yielding over 25% efficient solar cells. The record solar cell conversion

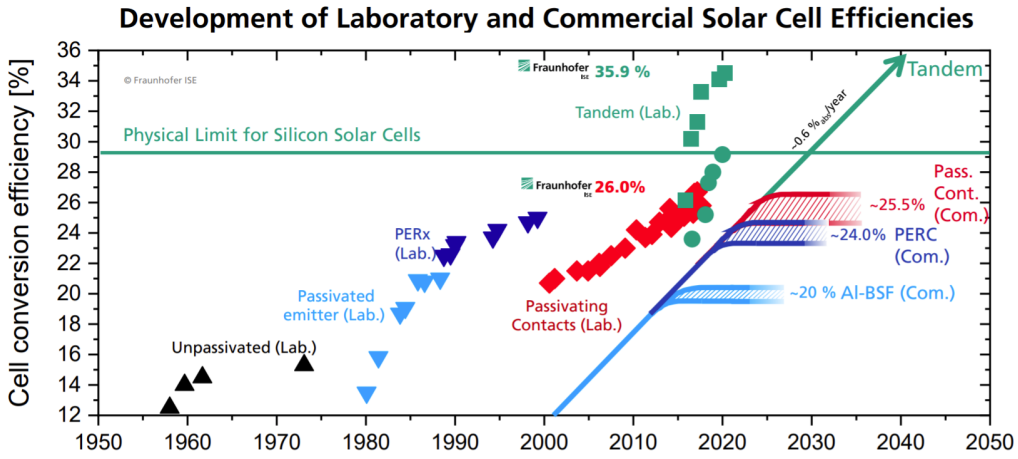

Figure 1.2: Development and prediction of conversion efficiencies of laboratory based solar cells [2].

efficiency is currently set at 26.3% by Kaneka ([3, 4]), where they used heterojunctions in the IBC (interdigitated back contact) configuration. By placing the contacts at the back, the light absorption can be maximized. This development shows that c-Si technology is already reaching its limits, because the theoretical efficiency limit is calculated to be 29.4% (Figure 1.2). This is reached when there is no surface or defect-related recombination and when the light trapping is at its optimum. However, one downside of heterojunction solar cells is that it can only work in a low temperature production line, which limits its processing applications. TOPCon technology, on the other hand, is compatible with the already existing high temperature production line [5].
The goal of this thesis project is to investigate the impact of the thermal budget of such high temperature processes on the contact performance and characterise the charge carrier transport in the contacts. These contacts could be used in several solar cell configurations (front-back contacted (FBC), IBC, hybrid) in the future, so understanding of the transport mechanisms is crucial for the development of this photovoltaic technology.

1.1. Solar cell principle

The working principle of a solar cell has originated from the discovery of the photovoltaic effect, first observed by Edmund Bequerel in 1893. The photovoltaic effect is based on the energy transfer from photons to electrons. In a crystal lattice (e.g. silicon), atoms are arranged and are held together by electrons that form bonds to neighbouring atoms. These electrons are bound, also called valence electrons. At temperatures above T = 0 K, there also exist mobile electrons, free electrons, which can move freely through the crystal lattice. The energy of an electron determines its state (free or bound), and thus its ability to act as a free charge carrier. For silicon, which is a semiconductor, there is a certain range of energies that the electrons cannot occupy, which is called the band gap E_G. This band gap is characteristic for each semiconductor material [6].
If the energy of the absorbed photon is higher than E_G, a valence electron can be excited to an energy level in which it is not bound. When excited into this conduction band, the electron leaves behind an unoccupied energy state, which can be considered as a positive charge, also known as a hole. This hole can also be considered as a free charge carrier that can move through the lattice. When a hole and an electron meet, they recombine and their energy is released. This can be either by a photon or lattice vibrations (heat).

To be able to convert light into electrical energy, it is important to separate the charge carriers before they recombine and to create an electrical circuit to harness power from this energy conversion. The carrier separation is done by using the charge of the carriers to draw the holes and electrons to opposite polarities of the solar cell. In principle, a solar cell works as a diode, which only allows electrons to flow in one direction, and holes in the other direction. After the electrons have reached the contact, they are eventually collected and used to perform work in the external circuit. When the electrons arrive at the other contact of the solar cell, they will recombine with the holes that have accumulated there.

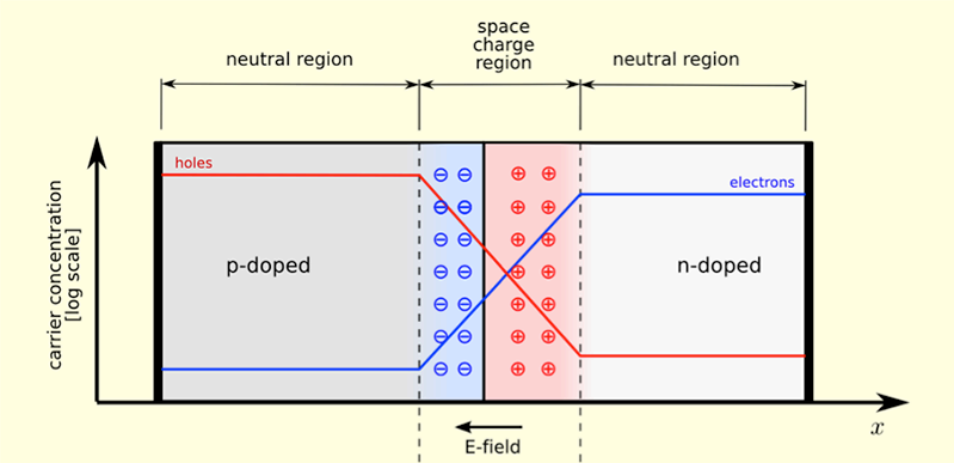

Figure 1.3: Schematic of a pn-junction in a solar cell that separates the electrons and holes. The space-charge region is depleted from charge carriers by recombination [7].

The separation of charge carriers is done by a p-n junction, which brings together two materials with opposite fixed charge. This opposite fixed charge results in an internal electric field, which will work on the charge carriers that are present in the solar cell. The principle is shown in Figure 1.3 [7]. p-Type or n-type materials are obtained by incorporation of atoms in the Si lattice that have a different amount of valence electrons in their outer shell. An additional valence electron will increase the concentration of electrons, while leaving a fixed positive charge behind. One valence electron less will result an unoccupied state, creating a hole and a negative fixed charge. This will decrease the concentration of electrons. High levels of these charge carriers will reduce the concentration of the opposite charge carrier, reducing the probability of recombination. It is critical to minimize the recombination and all other loss mechanisms in the solar cell to maximize the energy yield.
Some important parameters that define the performance of a solar cell are short circuit current density (J_{sc}), open-circuit voltage (V_{oc}) and Fill Factor (FF). J_{sc} is the maximum current that can be generated in a solar cell, when the applied voltage is zero. V_{oc} is the maximum voltage that the cell can produce, namely when the current through the solar cell is zero. The FF is defined by the ratio between the maximum operating voltage of a solar cell and the product of J_{sc} and V_{oc}. All three parameters define the maximum conversion efficiency of a solar cell.

1.2. Loss mechanisms

The energy conversion from light into electricity is not perfect, caused by many different loss mechanisms of the solar cell. To start, not all photons can be absorbed by the silicon and create an electron-hole pair. This is one of the optical loss mechanisms in that limit the conversion efficiency of a solar cell. As already mentioned, the electrons and hole can recombine, which is one of the electrical loss mechanisms that limit the solar cell performance. There are many different factors that causes losses in the solar cell, which is often referred to as the leaky bucket principle. The incoming light is the full bucket of energy, where in every step closer to carrier collection the bucket leaks out energy. Theoretically, only 29.4% remains for silicon, which is called the Shockley-Queisser limit. Below, all main loss mechanisms are described that occur in a solar cell. The losses inside a solar cell can be divided into two types, namely optical losses and electrical losses [6].

Optical loss mechanisms

Non-absorption

Due to the existence of a bandgap, photons with an energy lower than the bandgap will not be absorbed into the semiconductor material. The photons will pass through the semiconductor, which makes it energy loss from unused available energy.

Thermalization

The opposite happens when the energy of a photon is higher than the band gap energy. This photon will excite the electron to a high energy state, after which the electron will fall back to a lower state. The excess energy is released as heat in the lattice.

Reflection

As light passes through several interfaces in the solar cell before reaching the absorber layer, light is reflected from the surface. The reflection of each material and surface orientation is different, so reflection can be minimized by creating a textured surface and adding anti-reflection coatings (ARC).

Parasitic absorption

As light travels through layers that are not responsible for the charge carrier generation, photons are absorbed before reaching the absorber layer. It is thus crucial to optimize the layers in front of the absorber.

Shading

Metal contacts on a solar cell limit the amount of light that can enter the solar cell. All light that hits the metal is reflected, so the size and spacing of the metal fingers is crucial to maintain a maximum conversion efficiency.

Electrical loss mechanisms

Resistive losses

When charge carriers are transported through the layers of a solar cell, they will experience a finite conductivity of the subsequent material that they are in. This also includes interfaces where material properties change. This contributes to the series resistance of the solar cell. Minimizing the series resistance will result in a higher operating voltage of the solar cell.
Losses also arise from leakage currents, which are characterised by the shunt resistance of the solar cell. Maximizing the shunt resistance will maximize the operating voltage of the solar cell.

Radiative recombination

Radiative recombination is also called direct recombination, because an electron relaxes to its original energy state. The energy is then released as a photon, which makes it the opposite mechanism of photogeneration. In a direct bandgap material like InAs, radiative recombination is dominant. However, Si is an indirect bandgap material, so radiative recombination can be considered negligible. Figure 1.4a shows the principle of radiative recombination.

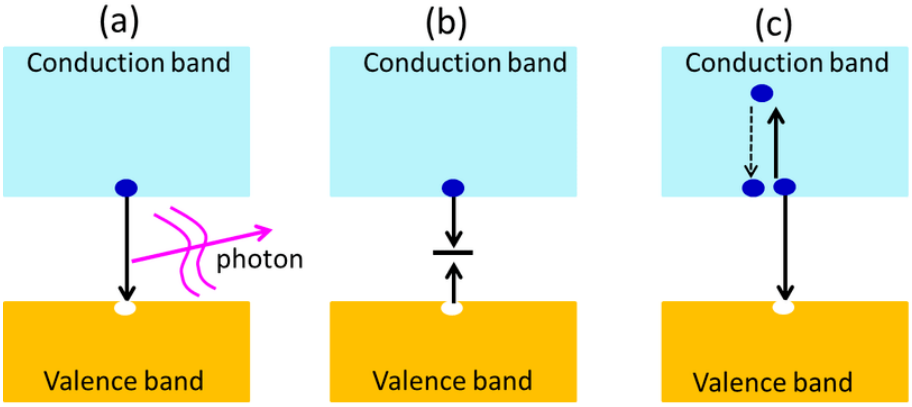

Figure 1.4: Main recombination mechanisms that occur in a semiconductor. (a) Radiative recombination, (b) SRH recombination and (c) Auger recombination [8].

Shockley-Read-Hall recombination

Figure 1.4b follows up with Shockley-Read-Hall (SRH) recombination. This type of recombination is facilitated by lattice defects or impurities. These defects or impurities create available energy states within the bandgap (trap states). An electron can get trapped in this energy state, where it can recombine with a hole that is attracted to it. SRH recombination is thus proportional to the trap state density (N_T) in a material.

Auger recombination

Auger recombination, as shown in Figure 1.4c, is a three particle process. It occurs when an electron and hole recombine and the energy and momentum is transferred to either an electron or hole. This makes Auger recombination dominant in the bulk of indirect bandgap materials. The energy of the excited electron or hole is lost as heat. Auger recombination depends strongly on the charge carrier concentrations in the material. These concentrations are manipulated by doping, so the doping level will strongly influence the Auger recombination. Auger recombination is proportional to the square of the doping level (N_{dop}^2).

Surface recombination

At the surface of a solar cell the silicon lattice ends, where many electrons were not able to create a covalent bond with another electron. This will result in many dangling bonds at the surface, which act as trap states. The trap states induce SRH recombination as described previously. Since charge carrier densities are large at the surface, the surface recombination is the largest contributor to the total recombination in a solar cell. A low surface trap density can be achieved by passivation, which will be explained in Section 1.3.

1.3. Surface Passivation

The concept of passivation is about minimizing the recombination losses in a solar cell. This includes recombination in the bulk and at the surface. The current silicon casting has made the bulk recombination negligible (minority carrier lifetime > 1ms) [9, 10], so tackling surface and contact recombination is the most important. Here, two types of passivation can be defined, namely: chemical passivation and field-effect passivation [10].

Chemical passivation

Chemical passivation is based on the reduction of the density of electrically active defect states (dangling bonds), which are mostly present at the surface or an interface. Since the surface recombination rate is proportional to the defect density, chemical passivation will dramatically decrease this surface recombination. This can be achieved by depositing a material layer on the c-Si wafer, creating bonds between the surface silicon atoms and the passivating layer. This is usually referred to as a capping layer. The concept of chemical passivation is shown in Figure 1.5 [12]. SiO_x passivates the dangling bonds of the c-Si, reducing the defect states at the surface. The remaining dangling bonds can be passivated by hydrogenation [13], where hydrogen atoms passivate many dangling bonds, lowering the defect density even further.

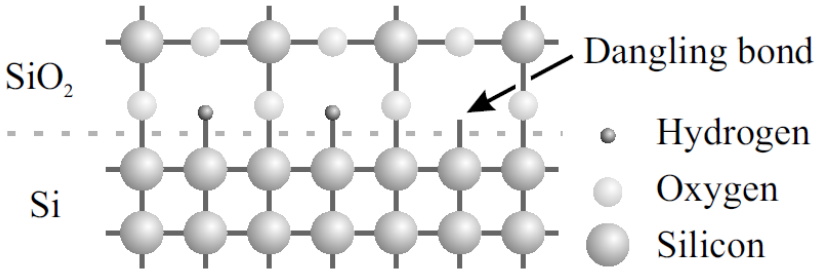

Figure 1.5: Chemical passivation of the c-Si surface with SiO_x and additional hydrogen bonding [11].

Field-effect passivation

Field-effect passivation is based on the reduction of the surface concentration of minority charge carriers. This can be achieved by highly doped layers in the cell that introduce an internal electric field at the contact interface. This is possible by implementing a doping profile below the surface of the silicon surface, by a doped additional layer, but also by adding fixed charges or using a work function difference to create the internal field. The band bending (internal electric field) will create a carrier selective barrier at the interface and simultaneously contribute to the electric field strength in the cell. High doping ensures a low minority carrier concentration at the contact, which reduces the possibility for recombination. Minority carriers can also be repelled from the contact by the introduction of fixed charges in the contact or at the surface. Certain capping layers used for chemical passivation have shown to contain fixed charges (either positive or negative), which can be beneficial for the collection of charge carriers. These fixed charges can repel minority carriers, but also attract majority carriers, enhancing the carrier collection.

1.4. Carrier-selective passivating contacts

As the loss mechanisms in solar cells are optimised further, the recombination losses at the contacts have become the largest limiting factor for high-efficiency lab-scale c-Si solar cells [14]. The PERx solar cell designs have proven to increase the conversion efficiency of the cells, but with this increase, the process complexity also increased [14, 15]. A different approach to tackle the contact recombination losses are passivating contacts. This consists of a layer that separates the metal from the c-Si wafer, (i) mitigating surface recombination by passivation and (ii) acting as a conductive carrier extraction layer towards the contact [14, 16].

To be effective at both of these functions, the interface between the silicon and the contact needs to be carrier selective. This implies that the carrier conductivity for one type of carrier needs to be higher than it is for the other type. As the passivating contact is an additional layer, the optical losses in this layer need to be optimized [18]. The selectivity of a contact in a c-Si solar cell is defined by the recombination current density (J_0) and the contact resistivity (ρ_c). Here, J_0 represents the recombination losses and ρ_c represents the resistive losses. Research aims to minimize both of these parameters, where one of the two can be more limiting than the other, depending on the contact configuration.

Poly-Si/SiO_x passivating contacts

The passivation of the c-Si surface can be done with SiO_x, which is usually deposited as an ultrathin layer. This ultrathin layer creates a potential barrier for charge carriers, but this can be overcome by tunnelling. An asymmetrical tunnelling probability for electrons and holes at the interface creates a carrier selective junction. On top of this passivating layer, there is a highly doped poly-Si layer, which creates the necessary field-effect passivation to repel minority carriers from the c-Si/SiO_x/poly-Si interface. An advantage of the excellent passivating properties of this contact structure is that a full area metal contact can be used for carrier collection. This creates a potential for simplified solar cell

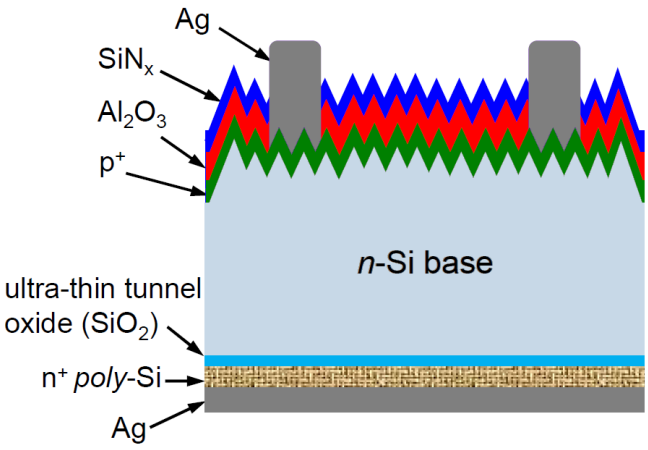

Figure 1.6: Example of a TOPCon solar cell with backside poly-Si/SiO_x passivating contact [17].

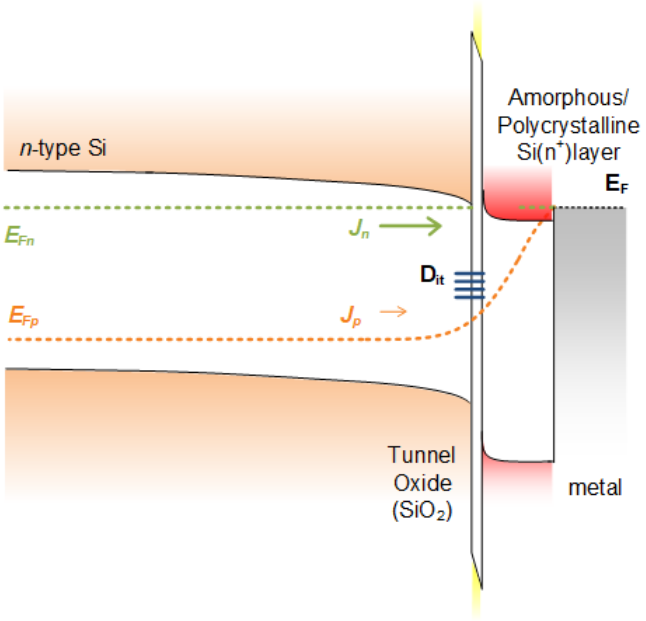

Figure 1.7: Band diagram of an n^+-poly-Si passivating contact on an n-type wafer [21].

fabrication.

Reducing the defect states at the c-Si/SiO_x/poly-Si can be enhanced by the hydrogenation of the remaining dangling bonds, as described in 'Chemical passivation'. This chemical passivation will result in a low recombination current density (J_0), while the field-effect passivation by the doped poly-Si will increase the open-circuit voltage (V_{oc}). The layered configuration of the SiO_x/poly-Si contact is shown in Figure 1.6, where the poly-Si contact is used at the backside of a solar cell. Until now, the highest efficiency for an industrial front-back contacted solar cell with poly-Si contact has been achieved in the TOPCon configuration [19], where the poly-Si passivating contact was implemented as n^+-doped full area back contact and the front emitter was p^+ diffused. Exploration towards double side passivating contacts is underway, but currently the device performance is limited by parasitic absorption in the poly-Si layer and the performance of p-type poly-Si/SiO_x contacts [20].

Carrier transport in the passivating contact

As mentioned, the principle of operation of poly-Si passivating contacts is based on the combination of chemical and field-effect passivation, while preventing direct contact between metal and c-Si. The charge carrier transport is based on the selectivity of the c-Si/SiO_x/poly-Si junction, which is facilitated by the doped poly-Si and the potential barrier created by the SiO_x. Figure 1.7 shows the band diagram of an n-type poly-Si contact on an n-type wafer. The highly doped poly-Si induces band bending at the tunnelling oxide, which creates a carrier selective electric field across the junction. The internal field will repel holes from the interface, reducing the hole concentration at the interface. On the other hand, electrons are pulled towards the contact.

At the p-type contact, a pn-junction is formed and the opposite carrier selective junction is formed at the SiO_x interface. The Fermi level will be close to the valence band, creating a band bending that repels electrons from the interface. When the cell is illuminated, Fermi level depinning occurs, as shown in Figure 1.7. The extent on this depinning will determine the total internal field and eventually the open-circuit voltage of the solar cell.

The tunnelling through the interfacial oxide is based on three tunnelling mechanisms, namely trap-assisted tunnelling (TAT), direct tunnelling and thermionic emission [10]. Trap-assisted tunnelling occurs when an electron passes through the insulator by hopping between defects in the material. Direct tunnelling is described by the probability of a particle passing the potential barrier and thermionic emission happens when an electron has a sufficient energy level to pass the barrier.
The theory of tunnelling was accepted and used to predict the carrier transport through the passivating

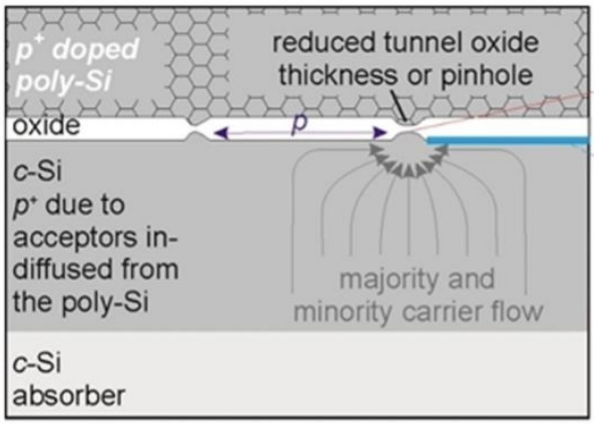

Figure 1.8: Schematic cross-sectional view of a poly-Si passivating contact with pinholes in the SiO_x [22].

junction, but when the technology improved, the tunnelling model was not sufficient anymore to meet the experimental data. Peibst et al. [22] suggested that the homogeneity of the oxide changes upon subjecting it to thermal treatments, changing its structure and thickness locally. The existence of pinholes in the SiO_x is discussed, which enhance the carrier transport at the interface. Ever since, the pinholes have shown to exist and positively impact the passivation quality of both n- and p-type poly-Si contacts.
Pinholes are considered to be actual holes or locally thinned regions of the SiO_x, which will both decrease the contact resistivity (ρ_c) of the junction. However, pinholes are extremely defective areas, which increases J_0 locally. It is thus of great importance to have a sufficient field-effect passivation at the pinhole sites to repel minority carriers from the interface. Posing a challenge to balance this decrease in ρ_c and increase in J_0 to obtain the best selectivity, many parameters need to be optimized in the poly-Si passivating contact.

Interfacial tunnelling oxide

From the tunnelling point-of-view, the thickness of the SiO_x is crucial for the carrier transport. Theoretically, efficient carrier transport by tunnelling can only happen up to an oxide thickness of ~2 nm [23]. However, making the SiO_x layer as thin as possible will not result in the best passivation quality. This is related to the diffusion of dopants from the poly-Si to the c-Si bulk, which happens during high temperature crystallization and activation treatments. A trade-off between dopant diffusion barrier, tunnelling transport and surface passivation has to be made to optimize the carrier transport and contact selectivity.
As mentioned, pinholes in the SiO_x can have a major impact on the carrier transport mechanisms at the interface. It is thus of great importance to create an advantage of this presence of pinholes to boost the carrier transport and reduce recombination at the interface. The pinhole density is a parameter that determines the trade-off between tunnelling transport and pinhole transport through the interface. The impact of the pinhole density on ρ_c and J_0 has been modeled by Wietler et al. [24], which has resulted in an optimal range of effective pinhole transport, while keeping the recombination low at the interface. These calculations have resulted in the optimal range of 10^5-10^9 cm^{-2} to achieve the best selectivity. It can be expected that this optimal pinhole density will be dependent on the oxide thickness, which determines the ratio of tunnelling transport and pinhole transport.
It has been shown by Lancaster et al. [25] that the pinhole density in the thin oxide layer depends on the annealing temperature. Around 900^oC, there is a fast increase of the pinhole density in the SiO_x. When the oxide layer is <2 nm, breakdown could occur at higher annealing temperatures (>900^oC) [26], depending on the oxide thickness. Kale et al. reported no pinholes when the annealing temperature was 850^oC [26].

Doped poly-Si layer

To achieve the best field-effect passivation and a high internal field, a high doping of the poly-Si is required. However, a downside is that these dopants can diffuse into the c-Si, creating defects and

reducing the field-effect passivation at the interface. It is thus important to get a sharp gradient in the dopant concentration at the SiO_x interface. This can be achieved by optimizing the thermal treatments of the poly-Si. Boron (used for p-type contacts) has a much higher diffusion coefficient than phosphorus (used for n-type contacts) [27], which has resulted in a structurally lesser passivation quality of p-type poly-Si passivating contacts.
To maximize the generated carriers, the parasitic absorption should be minimal. Poly-Si is highly absorptive, which limits the efficiency of a poly-Si based solar cell with a front junction [20]. This creates another trade-off, since a thick poly-Si results in the highest passivation quality and lateral conductivity, but induces the highest level of parasitic absorption. This creates a challenge to implement poly-Si passivating contacts in a full-area front-back contacted (FBC) configuration.

1.5. Thesis Research Objectives

The aim of this master thesis project is to investigate the impact of thermal treatments on the passivation quality of poly-Si based passivating contacts and understand the charge carrier transport mechanisms in the contact. The approach was based on the already existing concept of pinholes (and pinhole density) and a new look on the thermal budget of annealing treatments. These two concepts were approached separately, but can both help to explain the carrier transport in the contact structures. Furthermore, a new and simple approach was tested to extract the metal-induced recombination after contact formation.
The starting point of this thesis project was based on the findings of Feldmann et al. [20] and subsequently Wietler et al. [24], Polzin et al. [28] and many other publications where the carrier transport through the interfacial oxide by pinholes is discussed. The goal was to create these pinholes and find the optimal processing conditions to aim for an increase in V_{oc} and FF of solar cells with poly-Si based passivating contacts.

The first objective of this thesis project was to use the concept of pinhole-assisted carrier transport to improve the passivation in the poly-Si passivating contact. To be able to confirm and quantify the existence of pinholes in the tunneling oxide, high temperature annealing treatments above 1000^oC have been performed on poly-Si contacts to create the pinholes. An experiment was set up to observe and count the pinholes.
The second objective of this thesis project was to optimize the thermal treatments of poly-Si based passivating contacts to find an optimal process window for solar cell processing. This optimization was paired with the introduction of an extra annealing step before dopant introduction, so-called pre-annealing, which will be responsible for the formation of pinholes. After dopant introduction, another annealing step, so-called post-annealing, is required to diffuse and activate the dopants. To be able to explain the differences in passivation quality, the dopant profile is obtained in experiments, where the aforementioned pinhole density will also play a role.
The third objective is to investigate the metal-induced recombination in poly-Si passivating contacts. As recombination in the contact reaches almost the minimum, the recombination at the metal-semiconductor junction is one of the main areas where there is a lot of potential efficiency gain. The goal is to find a simple method to extract the metal-induced recombination and make a primary characterisation of this parameter for poly-Si based contacts. The influence of several thermal treatments will also be attempted to investigate to find out more about the origin of this recombination source. Contact annealing will be an important part of this experiment, where the time dependence of the metal-induced recombination will be sought for.

1.6. Outline

This thesis report consists of three main experimental chapters, as mentioned in 'Thesis Research Objectives'. Chapter 3 contains the investigation of pinholes in the tunnelling oxide, where Chapter 4 will investigate passivation for poly-Si passivating contacts with pinholes. Chapter 5 elaborates on a test to extract the metal-induced recombination.
Chapter 3 'Pinhole density in LPCVD poly-Si contacts' investigates pinholes in the tunnelling oxide of a poly-Si contact. The pinhole detection is tested and confirmed, after which the pinhole density is determined for several high temperature ($\geq 1000^oC$) annealing conditions.
Chapter 4 'Ion implanted LPCVD poly-Si passivating contacts' will elaborate on the passivation quality

of the same poly-Si contacts as described in Chapter 3 'Pinhole density in LPCVD poly-Si contacts'. Two separate thermal treatments will show at which thermal diffusion budget of contact fabrication the passivation will be optimal. This chapter is supported by 'Pinhole density in LPCVD poly-Si contacts', which could explain differences in passivation.
Chapter 5 'Extraction of metal-induced recombination in poly-Si based passivating contacts' will show a relatively simple method to extract metal-induced recombination ($J_{0,metal}$) after contact formation. After metal deposition, the contact will be formed by annealing, which will also induce a defect-rich junction between the poly-Si and the metal. In order to understand and minimize this recombination source, a method to extract this parameter is tested to be used in future research.

2

Experimental Method

This chapter will elaborate on the different processing steps that are used in contact fabrication and characterisation. Each element is described as it is performed in this thesis project. The first section will be focused on steps involved in the fabrication process and the second section will explain the setups used for characterisation by several measurements.

2.1. Fabrication

There are many steps involved in fabricating a contact structure or solar cell. Each of them are explained in this section, starting from the wafer characteristics and texturing to layer deposition and patterning with photo-lithography.

Wafers characterisation

In this thesis, the wafers that are processed are phosphorus doped (n-type), FZ <100> c-Si, resistivity range 1-5 Ω·cm, 100±0.2 mm diameter and with a thickness of 280±20 μm. The wafers are double-side polished, so a polishing step in not required in this research. To be able to start depositing the layered structure of a passivating contact, the c-Si wafer needs chemical treatments to: (1) obtain the desired light trapping capabilities by texturing and (2) maximize passivation quality by removing contaminants (organic and non-organic).

Texturing

The first step will be to texture the silicon wafer on both sides, which will improve the light trapping in the solar cell. The most efficient surface texture is random texturing, which can be obtained by wet chemical etching of the c-Si with tetramethyl ammonium hydroxide (TMAH, $(CH_3)_4NOH$). TMAH is especially effective, because its etch rate in the <100> and <111> direction differ strongly [29]. This phenomenon is called anisotropic etching, which is highly suitable for random texturing applications. It has been investigated that the <111>/<100> etch ratio is approximately 0.055 at 80^{o}C, which means that the etching in the <100> direction is 16-20 times faster than in the <111> direction. This will create randomized pyramidal structures at the surface.
In this work, a solution is prepared consisting of 1L 25% TMAH, 4L of DI water and 100ml of AT8 (ALKA-TEX 8). The temperature of the solution is raised to 80^{o}C to enhance the etching process. The AT8 that is added to the TMAH solution serves two purposes: (1) it extends the lifetime of the etching

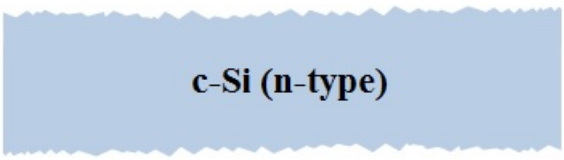

Figure 2.1: Silicon wafer after double-side texturing.

bath and (2) it reduces the etching time. The silicon wafers were etched for 15 minutes, followed by 5 minutes of rinsing with DI water. The wafers will resemble Figure 2.1.

Cleaning process

Contaminants can be present on the wafer surface after texturing, either from etching (residue), from air exposure (oxidants, dust particles) or elsewhere (organics, metals, etc.), so wafer cleaning is required to minimize the contaminants on the Si surface. Since the surface area has increased by the texturing, there are many more dangling bonds (defect states) at the surface. This surface is thus very susceptible to oxide formation.
To prevent contamination of the standard cleaning line, the first step is to remove the Si residue (Si+) and other contaminants that remained after the texturing process. To achieve this, the wafers are submerged into 99% HNO_3 for 10 minutes at RT, after which a 5 minutes rinsing step is performed. Now the wafer is clean from dust and residue, Standard Cleaning is performed on the wafers. The Standard Cleaning process that was performed in this research consisted of two steps:

1. Wafer cleaning with 99% HNO_3 at RT, followed by rinsing with DIW
2. Wafer cleaning with 69% HNO_3 at 110C, followed by rinsing with DIW

These processing steps will be referred to as Standard Cleaning, since some repetitions of these steps are required in the flowchart of the cell processing.
A downside of this cleaning step is the fast reactivity of the HNO_3 with the silicon, which can form a 0.7-1.4nm thick SiO_2 layer on top of the silicon [30]. Kobayashi et al. have proven that this oxide layer is already formed in 10 minutes at 25C in 61 wt% HNO_3, with a higher formation rate for higher temperatures. The chemical reaction that takes place in the HNO_3 solution is [31]:

$$2HNO_3 \longrightarrow 2NO^{2+} + H_2O + 3O^{2-}$$

Where the atomic oxygen ions are responsible for the formation of SiO_2. This oxide layer has been used many times as tunnel oxide in MOS structures (in transistors and solar cells), where the process is referred to as nitric acid oxidation of silicon (NAOS) or wet-chemical oxidation. NAOS oxide will also be used as tunnelling oxide in one of the experiments in this thesis. However, in some wafers this wet-chemically grown oxide layer is not desired, and previously formed oxide structures can be present at the surface, so all oxides are removed before the thermal oxidation step.

The removal of oxides on c-Si wafers can be done with two similar approaches. The first one is a quick dip (<30 s) in BHF (buffered hydrofluoric acid). BHF is a wet etchant, also referred to as Buffered Oxide Etch (BOE), which can etch away oxides or nitrides. It is a buffered solution of 49% HF (hydrofluoric acid) and 40% NH_4F (ammonium fluoride), commonly with a 1:7 ratio. The BOE process is based on the following chemical reaction [32]:

$$SiO_2 + 6HF \longrightarrow H_2SiF_6 + 2H_2O$$

which will only dissolve the SiO_2 at the surface.
The second approach is almost the same as BHF, since a solution of 0.55% HF is used to remove the oxides. This etching approach relies on the same chemical reaction, but the etch time is longer for the 0.55% HF solution. This is mainly because there is less HF present in the solution. The etching time for 0.55% is usually around 4 minutes to remove surface oxides, until the surface is hydrophobic. A minimum of 4 minutes rinsing with DI water is followed by one minute of isopropyl alcohol (IPA) to dry the wafer.

Rounding of pyramidal structures

When the wafers are cleaned, a very rough textured surface remains. This lay-out can be tricky in cell formation and structure build-up of several layers. A way to tackle this is to isotropically etch the pyramidal structures to smoothen and round them. This step will decrease the amount of defect states at the surface, as well as leaving only micrometer features [33]. An example of this rounding can be seen in Figure 2.2, displayed by Fesquet et al. in [33].
After rounding of the texture, Standard Cleaning is performed to remove the residue as well as organic

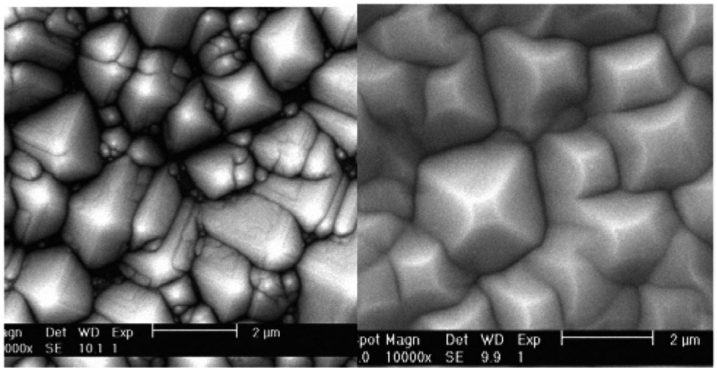

Figure 2.2: Rounding of pyramidal texturing of silicon wafers.

and inorganic contaminants. The steps in the cleaning process (exposure to HNO_3) has left the surface with a thin surface oxide layer, as mentioned in 2.1. For fast and complete oxide removal, an 0,55% HF solution is used. Submerging the wafers for 4 minutes will etch away the oxides. A hydrophobic surface will reveal when the oxides are completely removed. This part of cleaning process also includes the H-termination of the dangling bonds at the surface to mitigate oxidation of these defect states at the surface in contact with air.

Tunnelling oxide formation

To obtain an ultrathin oxide layer, two methods are commonly used. The first one is Nitric Acid Oxidation of Silicon (NAOS), where the oxide is formed in 69% HNO_3 at room temperature. The nitric acid reacts with the silicon and forms an oxide layer at the surface. In this thesis, clean wafers are immersed into 69% HNO_3 for 60 minutes. This will result in a uniform SiO_x layer with a thickness that is typically 1.5 nm [35].

The second method is Thermal Oxidation (ThOx), where the oxidation of silicon is initiated in an oxygen-rich atmosphere at elevated temperatures (675^oC). Here the oxygen binds directly with the silicon to form a SiO_x layer at the surface.
Previous research has shown that the formation of thermal oxides creates a denser SiO_x layer than for NAOS. This is especially important, since this will improve the SiO_x barrier for dopant diffusion into the c-Si. This has been experimentally proven by Geerligs et al. [34]. Figure 2.3 shows the a larger diffusion tail when NAOS is used as tunnelling oxide, compared to a thermally grown oxide.
The thermal oxidation process is performed at 675^oC for 3 minutes. This process involves stabilizing the furnace temperature to 675^oC in a N_2 atmosphere, after which O_2 is fed into the chamber to induce

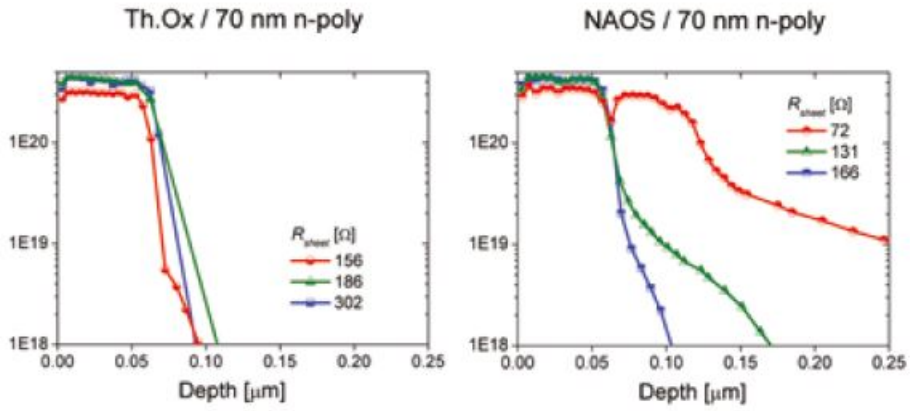

Figure 2.3: Doping profiles of poly-Si passivating contacts with an oxide layer formed with (left) thermal oxidation and (right) NAOS [34].

an oxidation reaction at the c-Si surface. The actual oxidation is performed for 3 minutes, which will create a SiO_x layer with thickness of approximately 1.5 nm [36]. The actual thickness will be determined by Spectral Ellipsometry.

Low-pressure chemical vapor deposition

One of the methods to create a poly-Si layer on top of the SiO_x layer is low-pressure chemical vapor deposition (LPCVD) of hydrogenated amorphous silicon (a-Si:H). The mechanism during this process is based on the overall chemical reaction stated below, as described by [37].

$$SiH_4(g) \longrightarrow Si(s) + 2H_2(g)$$

This reaction consists of six possible intermediate reactions, which mainly depend on the SiH_4 flux to the surface and the amount of reactive sites at the surface (dangling bonds). As the LPCVD implies, the reaction takes place at very low pressures (~150 mTorr), but also at an elevated temperature in a tube furnace.
Research inside the PVMD group of TU Delft has shown that 580^oC with a SiH_4 gas flow of 45 sccm is the most suitable for the LP-CVD of a-Si. The deposition rate of a-Si:H during LPCVD at 580^oC is approximately 2.2 nm/min [37], but the actual deposition rate is determined and monitored by EKL lab members. For the textured samples, the deposition time is 11.33 minutes, where the expected thickness of the a-Si:H layer is 20 nm on a textured substrate. The thickness for a textured surface will be less than a flat surface, since the surface area has increased by the texture. After deposition, the samples are annealed for another 60 minutes at 600^oC to reduce the stress in the a-Si:H layer.

Plasma-enhanced chemical vapor deposition

To deposit thin silicon-based films on a substrate wafer, radio-frequency plasma-enhanced chemical vapor deposition (rf-PECVD) can be used. The principle of this deposition technique relies on two mechanisms. The first one is the rf-plasma generated in the deposition chamber. Source gases are fed into the chamber, which can be dissociated when the molecules absorb energy from a rapidly oscillating magnetic field (radio frequency) between one electrode and the chamber walls. As the gases dissociate into ions, a highly energetic plasma is formed.
The second mechanism involves the navigation of the ions to the substrate, where they can react with the substrate to form the film. Since ions are charged particles, an electric field will impact the direction of the movement of the ions. In the deposition chamber, the substrate is attached to the grounded electrode, where the other electrode is placed at the opposite position. Important parameters that influence the quality of the layers and the deposition rate are the gas flows, the temperature of the substrate, the rf power and many other settings of the equipment. A schematic example of an rf-PECVD setup is shown in Figure 2.4 [38].

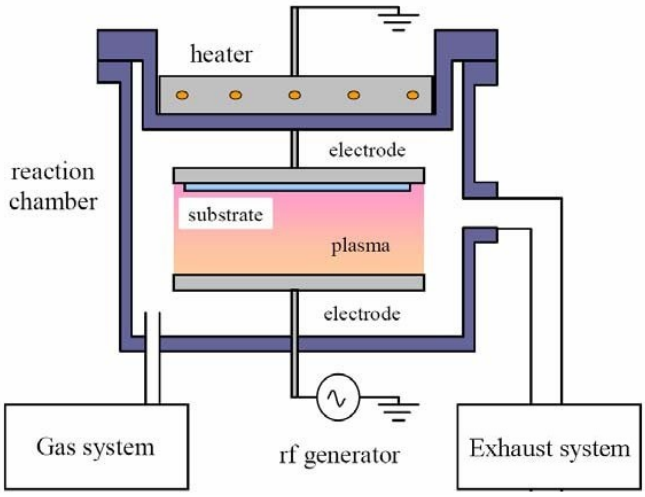

Figure 2.4: Schematic view of the rf-PECVD deposition chamber [38].

To prevent impurities in the film, the plasma is generated in a vacuum chamber. In some cases, the chamber is first purged with an inert gas (like argon), after which the chamber is pumped to remove the inert gas. Then, the gas flows should be stabilized to obtain a stable growth process. The substrate should be at an elevated temperature to facilitate the growth process, so a heater is present. Sometimes the heater is placed at a distance (like in Figure 2.4), but a setup where the substrate makes contact with the heater is also common.
In this research, several different rf-PE-CVD setups are used, with all different applications. (AMOR (a-Si:H), Novellus (SiN_x) and OXFORD (SiN_x))

Ion implantation

Ion implantation is used to introduce dopants in a substrate. This technique is extremely useful, since precise control over the depth and dose of dopants is possible. Dopant ions are generated by ionization, after which they can be sent towards the sample. The ions are accelerated with electromagnetic fields, towards an aperture to create an ion beam. The path is curved to select the ions with a particular mass from the ion beam. To maintain a linear path for the ions, the system should be kept at high vacuum, since the ions should not collide with ambient gas molecules. The ion beam is then focused on the substrate, where they will impact on the surface. The energy of the beam is varied, ranging from several keV to MeV. The energy will determine the depth profile of the dopant atoms at the surface. The setup of ion implantation is shown in Figure 2.5 [39].
When an ion hits the surface, its energy will determine the average depth it will reach inside the semiconductor lattice. As the ion collides with semiconductor atoms and bonds in the lattice, the path through the semiconductor becomes random, resulting in a Gaussian depth distribution of dopant atoms in the semiconductor. A Varian E500HP medium current implanter was used to implant phosphorus and boron in poly-Si contacts. For phosphorus, the beam energy was 20 keV and the implantation dose was $1{\cdot}10^{16}$ cm^{-2}. Similarly for boron, the beam energy was 5 keV and the implantation dose was $7.5{\cdot}10^{15}$ cm^{-2}.

High-temperature annealing

Annealing is performed in cell processing to change and improve the properties of the layers. Heating the materials to elevated temperatures can put the atoms in a more energetically favorable arrangement, often improving the passivation. In general, annealing is done in poly-Si passivating contact processing to crystallize the a-Si to form a poly-Si layer and drive the diffusion of dopants in the poly-Si. In fact, the annealing step transforms a layered structure into a carrier selective contact stack. This annealing step is always performed after the dopants have been introduced in the poly-Si. The initial conditions are

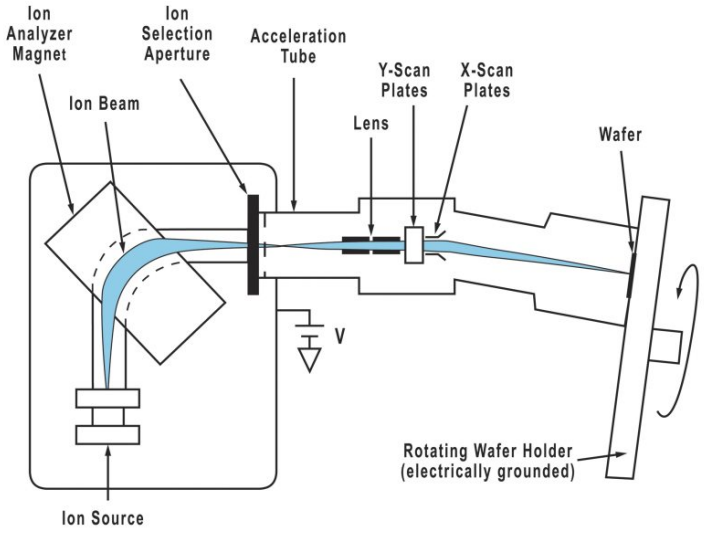

Figure 2.5: Experimental setup for ion implantation [39]. The figure show the curved ion beam that is directed and focused on the substrate.

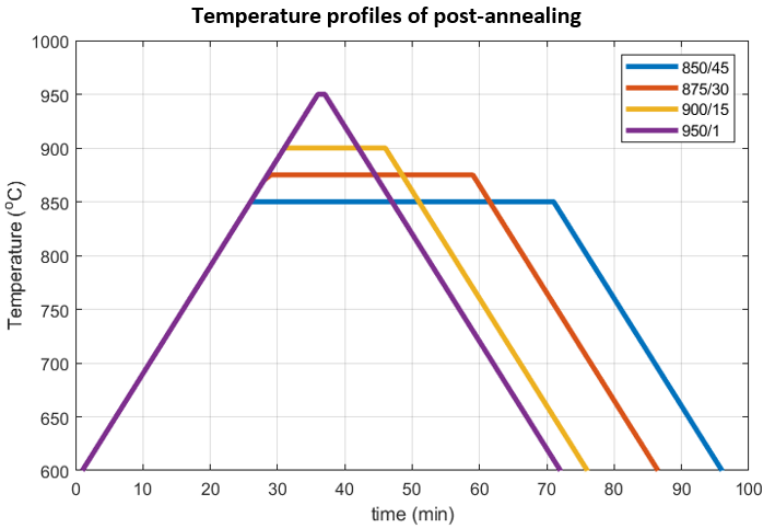

Figure 2.6: Temperature profile of the annealing processes with ramp up and ramp down time. Here, 850^{o}C annealing for 45 minutes is indicated by 850/45.

600^{o}C, where the ramp-up/ramp-down rate is 10^{o}C/min. The temperature profile of several annealing process is shown in Figure 2.6.

Hydrogenation

The hydrogenation process is often a combination of depositing a hydrogen-rich layer (a-SiN$_x$:H), which also acts as anti-reflection layer, and subsequent annealing in a hydrogen-rich atmosphere. This will maximize the chemical passivation of the interfaces in the poly-Si contact. Forming gas consists of a mixture of H_2 and N_2, where the mole fraction can vary. Forming Gas Annealing (FGA) can be performed at low pressures ~10^0 Pa, but also at atmospheric pressure (~10^5 Pa). An atmosphere with N_2 and H_2 is chosen, because of the the inert properties of N_2 and the passivating properties of H_2. Hydrogen is especially useful to passivate electronically active defects (dangling bonds). Annealing after a-SiN$_x$:H deposition will passivate any dangling bonds at the poly-Si/SiN$_x$ interface, but also at the c-Si/SiO$_x$ interface. The passivation is mainly facilitated by the Si-N bonds and the hydrogen atoms that attach to dangling bonds. FGA drives the hydrogen into the contact, where it will bond with any remaining dangling bonds.

Previous research in the PVMD group of TU Delft has found the optimal FG annealing conditions for poly-Si/poly-SiO$_x$ contacts with ~75 nm of SiN$_x$ [40]. The research has resulted in 30 minutes of annealing in a Forming Gas atmosphere at 400^{o}C in a tube furnace.

Photo-lithography

Photo-lithography is commonly used in the semiconductor industry to make complex structures with patterning. Its principle is based on using light to pattern a photosensitive layer that changes properties when illuminated. The photosensitive layer is often called photo-resist, which is applied to the surface of the wafer. Photo-resist is an organic polymer, which is sensitive to ultraviolet light. The application process is called coating, which can be done in several ways. The most common method is spin-coating, where the photo-resist is applied onto the surface while rotating the sample. The viscosity of the photo-resist and the rotational speed and time of the spin coater will determine the thickness of the layer. During this thesis project, a fixed thickness of 4 μm was used. To strengthen the resist layer, it is subjected to a baking step (110^{o}C).

After coating will follow the exposure of the photo-resist. The exposure time and intensity will be dependent on the type and thickness of the photo-resist. A mask will determine which parts of the wafer will be exposed to the UV light. Depending on the type of photo-resist, two results can be obtained from the exposure. For positive photo-resist, the exposed part of the photo-resist will eventually be removed in development. For negative photo-resist, the opposite will happen, where the non-exposed areas of the photo-resist will be removed.

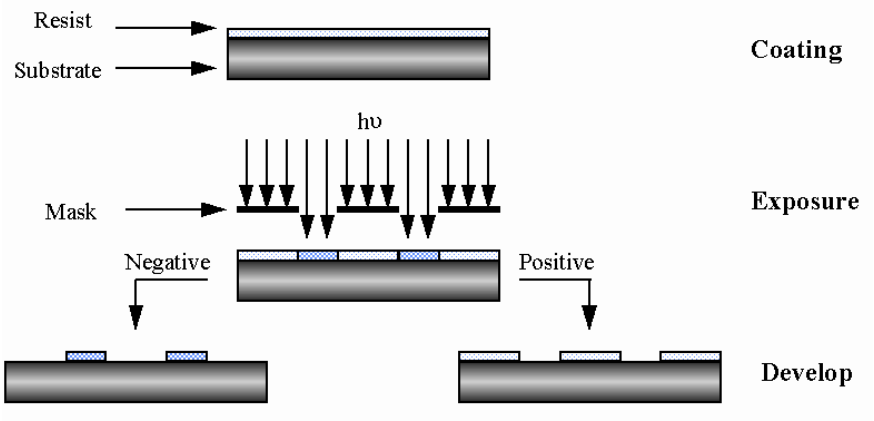

Figure 2.7: Steps involved in photo-lithography, where the figure shows the result after using positive and negative photo-resist [41].

The final step is to remove the exposed (or the non-exposed) photo-resist, while leaving the other area. This step is called development, which will open a certain area of photo-resist. The photo-resist is dissolved in a solution, specifically designed to be selective to the exposed and non-exposed photo-resist. The development step is followed by a post-bake at 110^{o}C. The open areas can now be subjected to etching or deposition steps to create patterned layer structures on the wafer.

E-beam evaporation

Metallization by evaporation is a form of physical vapor deposition (PVD), which can be done in four different processes, namely thermal evaporation, electron-beam evaporation, flash evaporation and resistive evaporation. These processes involve different mechanisms to heat the source material, where the source of heat for e-beam evaporation is an electron beam and for the other processes it is mainly done with a large current.

For e-beam evaporation, the source material is heated with an electron beam with an energy of several keV. A schematic view of the setup is shown in Figure 2.8 [42]. The figure shows the electron source under the source material, where the electrons are accelerated onto the source material. The kinetic energy of the electrons is transformed into thermal energy, which melts and evaporates the source material. An advantage of e-beam evaporation is the high controllability of the deposition rate [42]. The

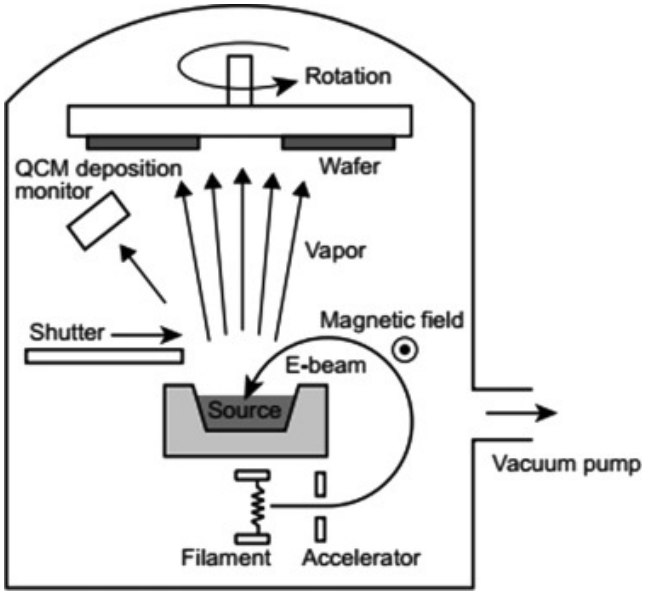

Figure 2.8: Schematic view of the electron beam evaporation setup [42].

deposition time is controlled by the shutter, which can close the source material from the substrate. The substrate(s) is(are) placed on a rotating disk, which ensures homogeneous deposition. It also provides the possibility to do the deposition on multiple substrates at the same time. The deposition process is done in a vacuum, which ensures that the amount of impurities in the deposited layer is minimized. In this research project the PROVAC PRO 500 High Vacuum PVD Coater is used [43].

2.2. Characterisation

This section will discuss the characterisation methods used in this thesis project. Characterisation involved the all measurements to determine the quality and performance of the fabricated structures.

Photoconductance lifetime measurement

To determine the passivation quality of a contact, it is important to know the effective lifetime of minority charge carriers (τ_{eff}). The effective lifetime is a measure of the effective recombination rate of these minority charge carriers, which defines the losses in a solar cell or contact structure. This effective lifetime can be derived by measuring the conductance, or excess photoconductance [44].
Under steady-state illumination, the recombination and generation in a semiconductor are equal, maintaining an equilibrium. However, this illumination creates an excess charge carrier density (Δn) in this material, defined by $\Delta n = G_L \tau_{eff}$ [6]. Where G_L is the carrier generation and $1/\tau_{eff}$ is the recombination rate. This relation can be rewritten into equation 2.1, which describes the recombination equal to the photogeneration.

$$J_{ph} = \frac{q\Delta n W}{\tau_{eff}} \tag{2.1}$$

Here, W is the thickness of the sample and q is the elementary charge. The excess carriers in the semiconductor result in an increase of the conductance of the sample, which is defined in equation 2.2. The excess carrier concentrations Δn and Δp are equal, which simplifies the expression.

$$\sigma_L = q(\Delta n \mu_n + \Delta p \mu_p)W = q\Delta n W(\mu_n + \mu_p) \tag{2.2}$$

μ_n and μ_p are the mobility of electrons and hole, respectively. Combining equations 2.1 and 2.2, the effective minority carrier lifetime can be defined by equation 2.3.

$$\tau_{eff} = \frac{\sigma_L}{J_{ph}(\mu_n + \mu_p)} \tag{2.3}$$

The conductance of the sample can be measured using the method of Sinton and Cuevas [44]. This method relies the contactless measurement of the conductance of a sample after a short light pulse. After the light pulse, the excess carriers will recombine, at a rate that is defined by the effective minority carrier lifetime. While the excess carriers recombine, the conductance of the sample decays according to the carrier densities. Using a calibrated reference cell and known values of the mobility of electrons and hole in the sample, the effective minority carrier lifetime can be determined.
To measure the conductivity, a coil in a bridge circuit is used. The light pulse that is generated should have a quick rise time, followed by a somewhat longer decay time. After the pulse the excess carrier density decreases exponentially. By monitoring the slope of the decay, the effective minority carrier lifetime can be determined for each level of excess minority carriers. The effective lifetime can also be defined as in equation 2.4, which is directly related to the excess carriers in the sample.

$$\tau_{eff} = \frac{\Delta n}{\frac{d(\Delta n)}{dt}} \tag{2.4}$$

In this thesis project, a Sinton WCT-120 Lifetime Tester is used to perform the lifetime measurements on the poly-Si contacts. The setup is shown in Figure 2.9, which shows a light source, reference cell and coil that form the basis of the experimental setup. The measurement tools are attached to a computer to process the conductance measurements and convert it into physical properties of the sample.

From the conductance measurement, several other parameters can be deducted that provide information about the passivation quality and recombination in the sample. As excess carriers are generated in the sample, these imply an open-circuit voltage in the sample. For a solar cell or contact on an n-type wafer, the implied open-circuit voltage (iV_{oc}) can be defined as in equation 2.5 [45].

$$iV_{oc} = \frac{k_B T}{q} ln\left(\frac{\Delta n(N_D + \Delta n)}{n_i^2}\right) \tag{2.5}$$

N_D is the doping concentration, which infuences the carrier concentrations. n_i^2 is the intrinsic carrier concentration in silicon and k_B is Boltzmann's constant. The iV_{oc} is then determined for 1 Sun

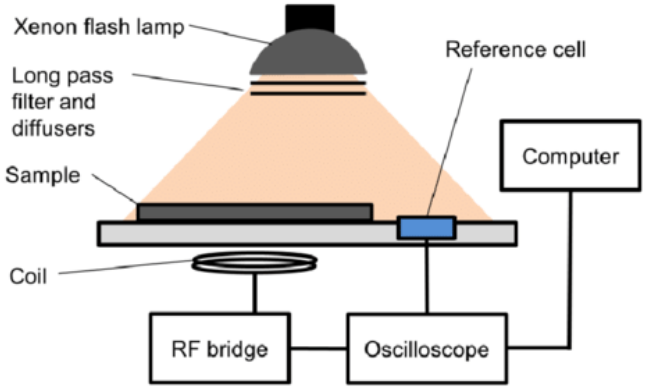

Figure 2.9: Experimental setup that was used for the photoconductance measurements [46].

illumination, which resembles actual current-voltage measurements at standard test conditions. The difference between the two is that for the iV_{oc}, several loss mechanisms are not considered. There is no current flowing through the sample, so resistive losses cannot be measured. It is assumed that the series resistance is zero and the shunt resistance is infinite. Now it is possible to analyze the recombination in the sample. Just like τ_{eff}, iV_{oc} is a measure of the passivation quality of the sample and a projection of the effective lifetime of the minority carriers.

The parameter to directly define the recombination inside a solar cell or semiconductor is the recombination current density (J_0), also called the leakage current. This J_0 in a solar cell or solar cell contact can also be extracted from the decay of excess charge carriers in the investigated sample. The method was first proposed by Kane and Swanson [47], which has proven to be strong and accurate. The advantage of this method is that it can be applied to symmetrically fabricated structures, which makes it possible to investigate one type of the contacts in a solar cell. The Kane and Swanson method relies on the assumption that the total recombination in a symmetrical sample can be written as in equation 2.6, which represents the recombination rate divided into separate parts.

$$\frac{1}{\tau_{eff}} = \frac{1}{\tau_{intr}} + \frac{1}{\tau_{SRH}} + J_{0,s}\frac{2(N_{dop} + \Delta n)}{qWn_i^2} \tag{2.6}$$

This shows the total recombination ($\frac{\Delta n}{\tau_{eff}} \iff J_{0,total}$) is assumed to be the bulk recombination ($\frac{1}{\tau_{intr}} + \frac{1}{\tau_{SRH}}$) and the surface recombination ($J_{0,s}$) of both sides of the sample. In the current quality of FZ silicon, SRH recombination is assumed to be negligible, so $\frac{1}{\tau_{eff}} - \frac{1}{\tau_{intr}}$ can be interpreted as the Auger recombination in the bulk. Taking the derivative of this $\frac{1}{\tau_{corr}}$ with respect to Δn, $J_{0,s}$ can be determined as described in equation 2.7.

$$J_{0,s} = \frac{qWn_i^2}{2}\frac{d}{d(\Delta n)}\left(\frac{1}{\tau_{corr}}\right) \tag{2.7}$$

$J_{0,s}$ is determined at high injection level, so the contribution of N_{dop} to the excess carrier concentration can be assumed to be negligible. An analysis of the inverse corrected lifetime as a function of Δn will reveal a linear increase, which slope is defined as J_{total}, the total recombination in the sample. Assuming that the surface recombination is much larger than the bulk recombination, it is assumed that $J_{0,total} = 2J_{0,s}$. Since $J_{0,s}$ is the specific property of the investigated contact, this is also referred to as J_0, which is the recombination contribution of a single contact.

When the lifetime curves are extracted with the photoconductance decay lifetime measurements, they can be interpreted according to the calculations from Cuevas and MacDonald [48]. These calculations involve the influence of diffused areas at the surface of the semiconductor. Their calculations have shown a direct relation between the dopant concentration at this surface to the effective lifetime and an inverse relation to the recombination current density (J_0). Their calculations have concluded in Figure

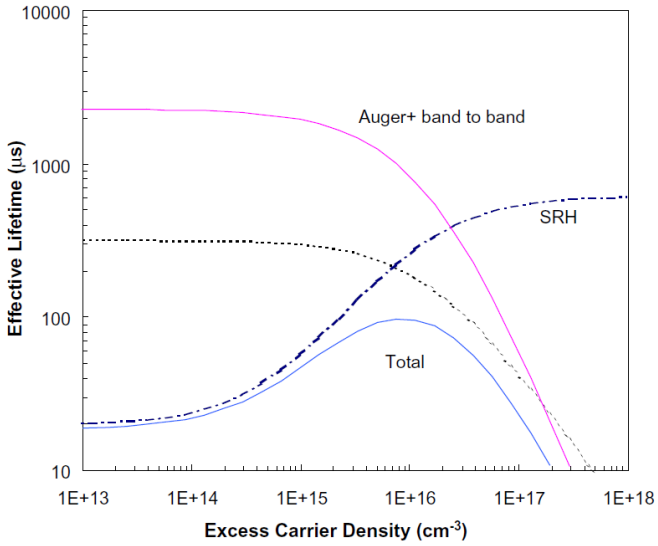

Figure 2.10: Contributions of Auger and SRH recombination to the effective lifetime curve of a semiconductor material [48].

2.10, which shows an example of the contributions of Auger and SRH recombination and the impact diffused dopants on the lifetime. As mentioned in 'Introduction' (Chapter 1), dopants can cause more Auger recombination, which is why the black and pink curves are similarly shaped.

Electrochemical Capacitance-Voltage profiling

The electrochemical capacitance-voltage (ECV) profiling is used to determine a depth profile of active impurities in the surface of an experimental sample. The measurement is based carrier profiling in connection with dopant profiling, which will provide information about the electrical activity of impurities [49]. Dopants as P, B, As, Sb and Al can be characterised in shallow doping profiles smaller than 100 nm.
The technique uses an electrolyte Schottky contact to create a depletion region inside the sample. This depletion region is free of conducting charges, but it contains activated dopants and electrically active defects. The depletion region acts like a capacitor, so measuring the capacitance of this depletion region will provide insight into the dopant density and electrically active defect density. By electrolytically etching the surface, a depth profile can be achieved.

The setup of the experiment is shown in Figure 2.11, where the entire experimental setup is displayed [50]. The sample is pressed against a sealing ring, closing the process chamber which will be filled with electrolyte. A platinum electrode is used to create a potential difference at the sample's surface, which is the working electrode. The potential difference induces a depletion region directly in the top layer of the sample. The counter electrode regulates the etching process, while the Calomel electrode acts as a reference for the platinum electrode.
Charged ions in the solution close to the surface will determine which charges are attracted to the surface of the sample. The other charges are repelled from the surface, creating a depletion region. To create this depletion region, the charges in the solution should be the same as the charge of majority carriers in the semiconductor. For example, in an n-type semiconductor the charges should be negative, depleting the surface of negative charges and attracting all positive charges. According to metal-semiconductor junctions, the capacitance and voltage are related as follows [50]:

$$\frac{1}{C^2} = \frac{2(\phi - V_a)}{qN_{dop}\varepsilon_0\varepsilon_r A^2} \tag{2.8}$$

where V_a is the applied voltage, ϕ is the contact potential and A is the area defined by the sealing ring. N_{dop} is determined by measuring C and dC/dV. During the measurement of C, the bias voltage V is changed slightly with frequency ω_c. This variation will reveal dC/dV, which is used to calculate N_{dop}.

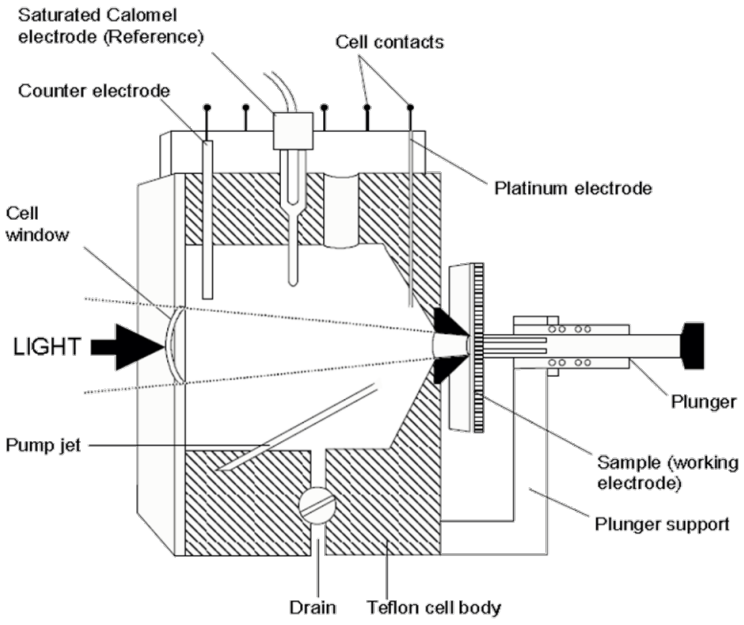

Figure 2.11: Electrochemical cell in the ECV measurement setup [50].

The etching process is completely electrolytically, which makes it a controllable process. The etching is based on the increasing separation of charge carriers, especially the accumulation of holes at the surface. For p-type semiconductors, the majority carriers at the surface are holes, so a forward bias is applied to enhance the accumulation of holes to the surface. With no electrons left to bond the Si^{4+}, the silicon will dissociate into the electrolyte as ions. For n-type semiconductors, the majority carriers at the surface are electrons, so holes are created by illumination of the etch area. Combining this with a reverse bias, the electrons get repelled from the surface and the silicon dissociates. A condition is that the energy of the incident photons ($\frac{hc}{\lambda}$) should be higher than the bandgap (E_g) of the semiconductor. The etched depth is is defined by the Faraday's law of electrolysis, describing the relation between the etched depth and the dissolution current I_{dis}.

$$W_{etch} = \frac{M}{zF\rho A} \int I_{dis} dt \tag{2.9}$$

This relation contains a pre-factor with the molecular weight (M), dissolution valency (z), Faraday constant (F) and semiconductor density (ρ). The actual measurement depth of the carrier density is not the etched depth, but the etched depth and the depletion depth combined ($W_{etch} + W_d$). The width of the depletion region is defined by [6]:

$$W_d = \sqrt{\frac{2\varepsilon}{q}\left(\frac{1}{N_A} + \frac{1}{N_D}\right)V_{bi}} \tag{2.10}$$

where V_{bi} is the built-in voltage, similar the the contact potential ϕ. Consecutive measurements of the carrier density at increasing measurement depth will reveal the doping profile at the surface of the measurement sample.

For the purpose of this thesis project, ECV profiles were measured to extract information about the doping profile for different annealing conditions (thermal budgets). The measurements were performed with a WEP wafer profiler CVP21 [51], at TNO Petten. The doping profiles of both n-type and p-type poly-Si contacts were measured in the process.

Optical Microscopy

An optical microscope is based on a series of lenses that can enlarge the image of a substrate. The substrate should then be placed in the focal plane of the lenses. The series of lenses comprises of an

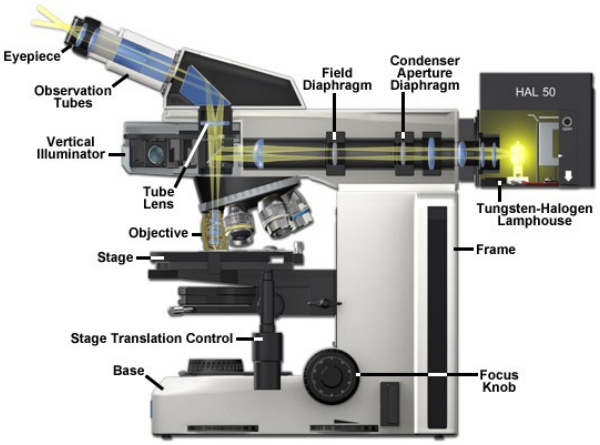

Figure 2.12: Classical setup of reflected light optical microscopy, where the image is also coupled to a computer to form a digital image [52].

objective lens, ocular lens and an eyepiece [53]. The objective is a very strong lens with a short focal length, so the substrate should be close to the lens. The ocular lens enlarges the image further to make it possible for the viewer to see the image. The eyepiece consists of two lenses that are positioned at the front and the back of the eyepiece. A virtual image is constructed in between the lenses, so the eye of the viewer can focus on the image.
The microscope that was used in this thesis could display a magnification of 100x, which was a sufficient range to observe μm features. A ZEISS Axiotron microscope was used [52], which could also display the image digitally. The scale of a certain region of interest was obtained by digital means. This microscope uses the reflected light microscopy, because the light cannot pass through the sample to generate an image. Figure 2.12 shows the components of a reflected light microscope.

Spectroscopic ellipsometry

Spectroscopic ellipsometry is a non-destructive way which is based on measuring the change in polarization of incident light onto a substrate. With information about the polarization, the thickness of films and their optical properties can be deducted with models. This is thus not a direct method to measure the film thickness, but existing models are often used to fit the measurement data.

When light hits the surface of a substrate, a part of it is reflected from the surface. The rest is refracted into the substrate, where it can reflect and refract again at the next interface. This creates a phase delay between the directly reflected light and the light that has passed the top layer. The delayed light will interfere with the reflected light, but only at specific wavelengths, measured by the ellipsometer. As the thickness of the layer increases, the interference oscillations will shift to higher wavelengths. A representation of this principle is shown in Figure 2.13. The EC-400 ellipsometer from J. A. Woollam Co. [54] was used for this thesis project and the data analysis was performed with the CompleteEASE software.

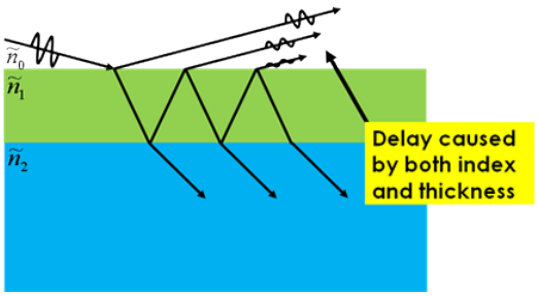

Figure 2.13: Schematic that show the principle of reflection and refraction of light at interfaces on which spectroscopic ellipsometry is based [54].

3

Pinhole density in LPCVD poly-Si contacts

This chapter will be focused on the actual detection of pinholes in the tunnelling oxide. Pinholes form during thermal processes, when the SiO_x rearranges in a configuration with a lower free energy. Pinholes are actually too small to see with a microscope, but the first section will explain a method to make this possible anyway. This method creates the possibility to analyze the pinhole density in the tunnelling oxide for different high temperature treatments. This chapter will start with an overview of the current findings on pinhole densities and their impact on the poly-Si contact performance.

3.1. Pinholes in poly-Si contacts

In 2016, the research into the carrier transport through the c-Si/SiO_x/poly-Si junction reached a point that the theoretical prediction models did not match the experimental data anymore. Peibst et al. [22] suggested that not only tunnelling transport, but also pinhole-assisted carrier transport occurs in the contact structure. The pinholes are present in the SiO_x, which rearranges under high temperature conditions. Peibst describes the pinholes as locally thinner regions of the tunnelling oxide, or even direct contact between the poly-Si and c-Si bulk. This theory can be understood easily when approached physically.
When deposited, the oxide is uniform and consists of many atomic layers of randomly organized Si and O atoms. When the oxide is exposed to a high temperature, the atoms rearrange into an energetically more favorable position where the free energy is lower(source). This causes the layer to become less homogeneous in terms of thickness with different types of pinholes forming.
When the oxide is completely removed locally, there will be an opening for the current to flow through with low resistivity. However, when the oxide has become locally thinner, the resistivity will be lower than with a thick oxide, since the tunnelling probability will be higher for the charge carriers. The locally thinned SiO_x areas can thus been seen as quasi-pinholes, because there is still a c-Si/SiO_x/poly-Si junction.

Ever since the suggestion of pinholes in the poly-Si/SiO_x contact, their role has been studied in the carrier transport in the contact. The study of Peibst et al. already created a model to predict the junction resistance and recombination current density for n-type and p-type contact, which showed to agree with existing experimental data from many research groups. This model predicted that the ideal amount of pinholes, the pinhole density, is a tradeoff between ρ_c and J_0. The predicted range for ideal carrier transport in the contact is proposed to be 10^5-10^9 cm^{-2}, where the pinhole density was approximated by directly linking it to the contact resistivity.
Experimental data on the relation between J_0, ρ_c and the pinhole density has confirmed the theory where J_0 increases and ρ_c decreases for a higher pinhole density [24]. An optimization of the pinhole density could result in a high selectivity of the contact.

It is important to note that the optimal pinhole density is not a universal value that all contact

types can aim for. The thickness of the oxide is crucial, but the type of oxide (thermal oxide [34], NAOS [30], PANO [55]) could also play a role. The thickness of the oxide will determine the dominant carrier transport mechanism(s), where tunnelling transport, pinhole transport and any combination thereof are possible. The pinhole density will then affect this carrier transport. The type of oxide could play a role, since each oxide has its own density and structure in the as-deposited form. The layer could then rearrange in a different manner during high temperature annealing.
Another factor that could have impact on the pinhole formation is the surface morphology, which could also be textured. Guthrey et al. [56] have found that the local thinning of the oxide occurs mainly in the valleys of the textured structure. This is probably related to stress in the SiO_x layer. The SiO_x grows perpendicular to the Si surface, concave or convex shapes can cause tensile stress in the layer. However, an extensive study on pinhole formation on randomly textured surfaces showed no preference for the location of the pinholes [57].

3.2. Experimental method

To find the pinhole density in the interfacial oxide, an experimental method from Tetzlaff et al. [58] was used. The experiment is based on the principle of selective etching and pinhole 'magnification', where the etch selectivity of (100)Si:SiO_x plays an important role. As is already known, TMAH can be used to anisotropically etch a (100)Si wafer to create a textured surface. As explained in 'Texturing', TMAH etches the (100) plane much faster than the other crystal planes, which assures the formation of pyramidal structures on the surface. An advantage of TMAH is that the etch selectivity of (100)Si:SiO_x can also be really high for certain conditions.
This is a perfect starting condition to design the pinhole experiment. When the poly-Si is etched away in TMAH, the SiO_x will act as an etch stop. But if there are pinholes present in the SiO_x, the etching will continue there, creating an underetch that enlarges the pinholes (Figure 3.1). If etched for the right time, the pinholes become visible while the SiO_x is still present.

MicroChemicals has found that the (100)Si:SiO_x selectivity is maximum for 5% TMAH at 70^{o}C, resulting in a selectivity higher than 9000 (Figure 3.2). This will then be used as etching solution in the experiment. To determine the right etching time, a test run is performed first, to see from which etching time pinholes become visible. It is also important to compare the pinhole densities at a range of etching times to observe in which range the pinhole density is constant. This test run will etch identical contact structures for 30-240 s with intervals of 30 seconds. It will be determined in which time interval pinholes can be counted accurately. The annealing temperature for this test run is 1050^{o}C, which was chosen because this condition has a high chance of forming pinholes.
The goal of this experiment is to see how much a high temperature treatment influences the pinhole density, so temperatures from 1000-1075^{o}C will be investigated. It is expected that the pinhole density increases for higher annealing temperatures and that pinholes will be present in all samples. This is based on the findings of Feldmann et al. [59], which reported the impact of pinholes already from 900^{o}C annealing.

The method to determine the pinhole density is based on making an approximation of the areal density of visible etch pits. Regular optical microscopy is used, with a magnification of 100x. Then, several regions of interest (ROIs) are chosen where the pinholes are counted manually. Depending on

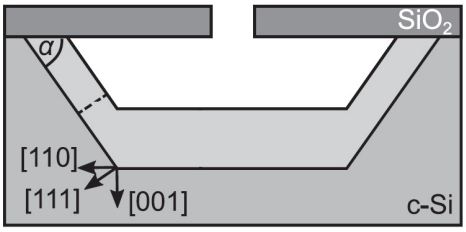

Figure 3.1: Schematic of pinhole underetching to enlarge the pinhole site [58].

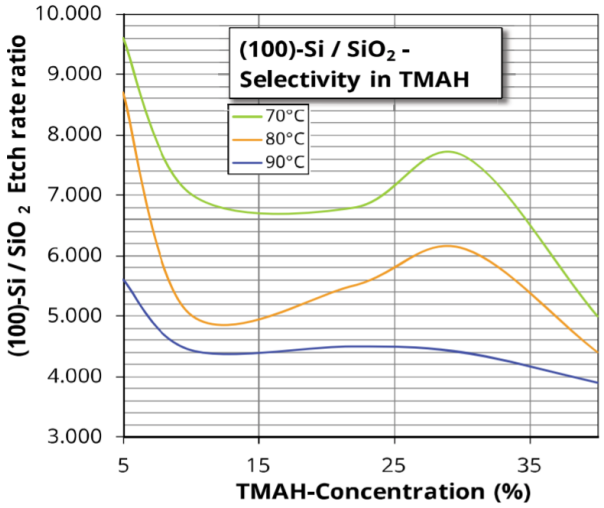

Figure 3.2: TMAH etch selectivity of (100)-Si:SiO_x as reported by MicroChemicals [60].

the pinhole density, the size of the ROI is adapted to still have a relatively accurate approximation. A description and visualization of the pinhole counting procedure can be found in Appendix A.

3.3. Sample preparation

The sample preparation for this experiment was based on the contacts from 'Ion-implanted LPCVD poly-Si contacts', but only half of the flowchart was needed to create the pinholes. A flat surface is considered here, because the pinhole detection can be done more accurately. This flat surface needed to be ultra clean before oxidation, so the samples have undergone two cleaning steps. The first one is wet chemical cleaning, which involved two steps of nitric acid (as described in 'Wet chemical cleaning', Chapter 2). This step removes all organic and inorganic contaminations on the surface, but leaves behind a 'native' oxide that is not desired before growing a tunnel oxide. This native oxide can be removed with an HF (0.55%) dip, followed by IPA drying (Marangoni). This will create an ultra clean surface, free from unwanted oxides.
To minimize any oxide formation between cleaning and oxidation, the maximum time between cleaning and oxidation was kept at 5 minutes. To create the tunnel oxide layer, dry thermal oxidation (Chapter 2) was used. This dry thermal oxide is dense and uniform, needed for diffusion blockage and degradation minimization. The recipe used for this oxide was already optimized in the PVMD group, so no time was spent on changing or optimizing this. The thermal oxidation was performed in a TEMPRESS tube furnace at 675^oC for 3 minutes. During these 3 minutes, the nitrogen and oxygen gas flow were 6.00 SLM and 0.60 SLM, respectively. The thickness of the oxide is determined to be 1.43 ± 0.007 nm, measured with spectral ellipsometry.

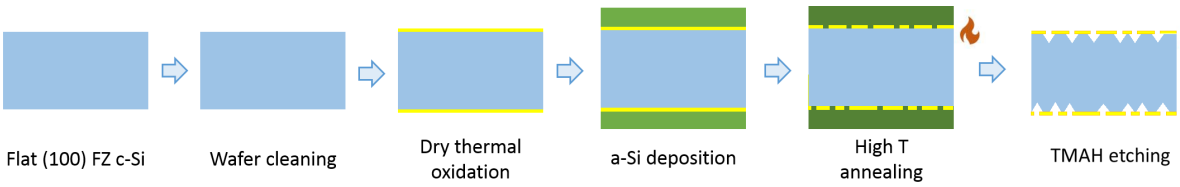

Figure 3.3: Processing steps involved in the sample preparation for pinhole detection.

Consecutively, an a-Si layer was grown with low-pressure chemical vapor deposition (LPCVD). To assure the quality of the contact, a limited time of 5 minutes between oxidation and poly-Si deposition was taken into account. The a-Si deposition was done in a TEMPRESS tube furnace at 580^oC in an atmosphere of silane (SiH_4) at a gas flow of 45 sccm. The deposition rate was extracted from log data,

which is around 2.21 nm/min. The aim of this experiment was 25 nm, because this experiment only required a capping layer of the oxide to create the contact configuration. The deposition time was thus set to 11.33 min.
The final step is to create the pinholes in a high temperature annealing process. The annealing process involved heating from 600^oC to the peak temperature (1000-1075^oC), where it only stays for one minute. Cooling down to 600^oC is also part of the annealing process. The high temperature annealing will also crystallize the a-Si, creating a poly-Si layer.
Figure 3.3 shows an overview of the processing steps, with a schematic of the samples. It can be seen that the samples are processed symmetrically, which is inevitable since thermal oxidation and LPCVD a-Si:H grow on both sides of the silicon wafer.

3.4. Results

The first results are from the test experiment, where a workable range of the etch time was determined for the comparison of pinholes in samples subjected to increasing annealing temperatures. Figure 3.4 shows the evolution of the sample surface for increasing TMAH etch time. It can be seen that pinholes are not visible at all for etching until 60 seconds, which could be explained by the fact that the etching through the pinholes happens more slowly, since the area is extremely small. From 90 seconds of etching the pinhole become visible, but still they are difficult to distinguish until 150 seconds of etching. The pinholes appear still as shadows, while being at the sharpest focus of the microscope.

However, after 180 seconds of etching the pinholes can be marked easily while they remain separated.

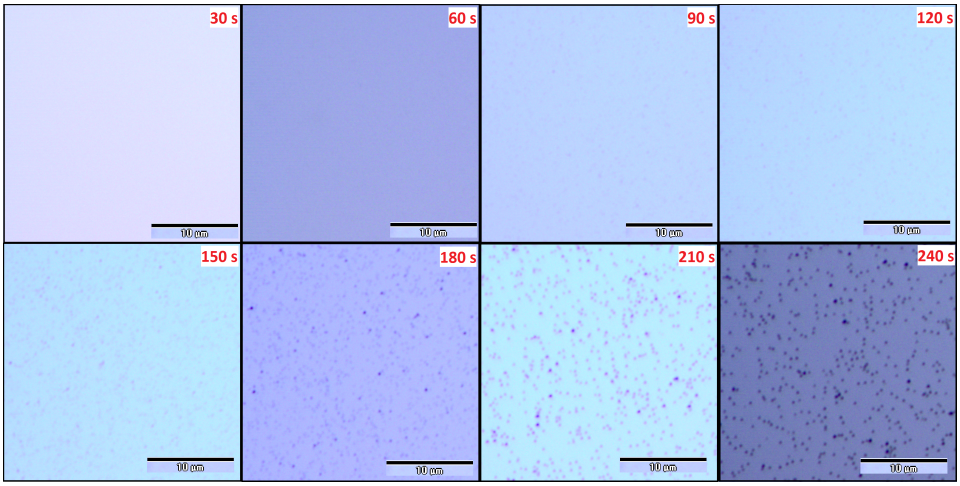

Figure 3.4: Microscopic images of the etch pits in the SiO_x layer after increasing etching times (100x). The annealing temperature for this test was 1050^oC.

For 240 seconds of etching, the pinholes become bigger, sometimes already merging with neighboring pinholes. This could disrupt the accuracy of the pinhole density, so an etch time longer than 240 seconds is not needed. The desired range for the determination of the pinhole density is thus 180-240 s.

Figure 3.5 shows the measured pinhole density for each etch time, where the uncertainty boundaries are defined by the standard error between the regions of interest. The measured pinhole density is in

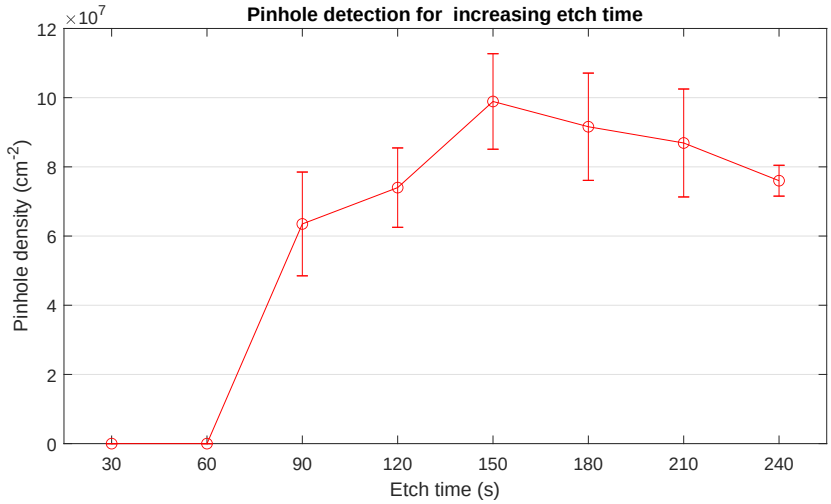

Figure 3.5: Pinhole density for increasing etch time to test the accurate detection range for pinholes in the SiO_x. Pinhole density was determined for 1050^oC annealing, where the error bars represent the 95% confidence intervals of the measurement.

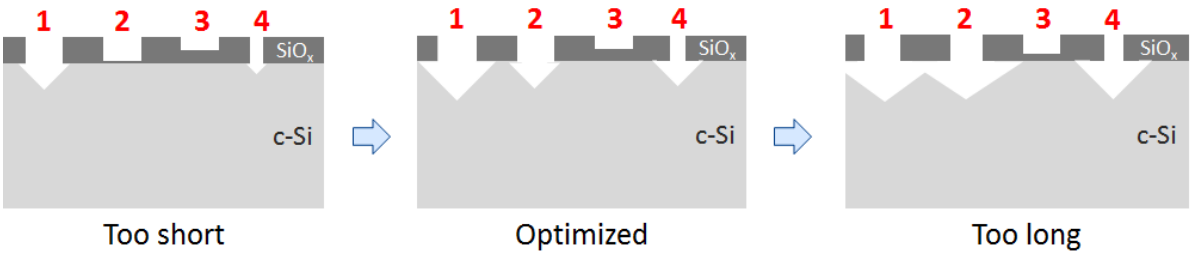

Figure 3.6: Example of four types of (quasi-)pinholes that can exist in the SiO_x layer. Etching for too short of too long will affect the pinhole density measurement. Types: (1) actual hole, (2) few atomic layers of SiO_x, (3) locally thinner SiO_x (4) narrow hole in the SiO_x.

the range of 10^7-10^8 cm^{-2}, which is in the optimal range of operation as described by Wietler et al. [24]. The pinhole density in these experimental samples will be different from Wietler et al., since the thermal oxide thickness is different (Wietler et al. [24] d=2.2nm; This work d=1.43nm). This test also shows clearly that pinholes have formed in the oxide, but the oxide layer itself is still intact. It will probably require more time or a higher temperature to break up the oxide. This will be dependent on the oxide thickness and density.
Figure 3.5 shows that the detection of pinholes first increases and from 240 seconds starts to decrease again. This can be explained by the fact that the actual surface of the SiO_x does not consist of solid areas with fixed thickness and actual holes through it. After annealing at high temperature, the SiO_x becomes an inhomogeneous layer with locally thinner regions. Actual holes will also form, but the locally thinner regions will also enhance the carrier transport through the interface. Several different types of pinholes can be identified that could affect the measurement of the pinhole density. All pinholes are expected to affect the carrier transport, either by a completely removed potential barrier, or by a more shallow potential barrier that will increase the tunnelling probability of charge carriers.
Figure 3.6 shows a schematic representation of four types of pinholes, of which 2 and 3 can be considered as quasi-pinholes, since there is no actual hole in the SiO_x. An exaggerated example is given of what happens during the etching process, where it is possible that some pinholes (2 and 4) become visible after a somewhat longer etch time. Two possible causes are either the pinhole is very narrow, which makes it harder for the TMAH to reach the c-Si, or there are still a few atomic layers of SiO_x left that slow the etching. Etching too short will result in an underestimation of the pinhole density. However, the pinholes can also merge (1 and 2), which will also affect the pinhole density measurement. Etching too long will result in an overestimation of the pinhole density. It is thus important to perform the experiment in the optimal etching range to obtain the most accurate pinhole density.

Using the etching range as determined in the test experiment, the pinhole density for four different annealing temperatures was determined. The results are shown in Figures 3.7 and 3.8a-b, where the average pinhole density is shown in Figure 3.8b for each annealing step and etch time. A range of etch times was chosen to determine the pinhole density, because the ideal etch time was not known for each annealing condition.

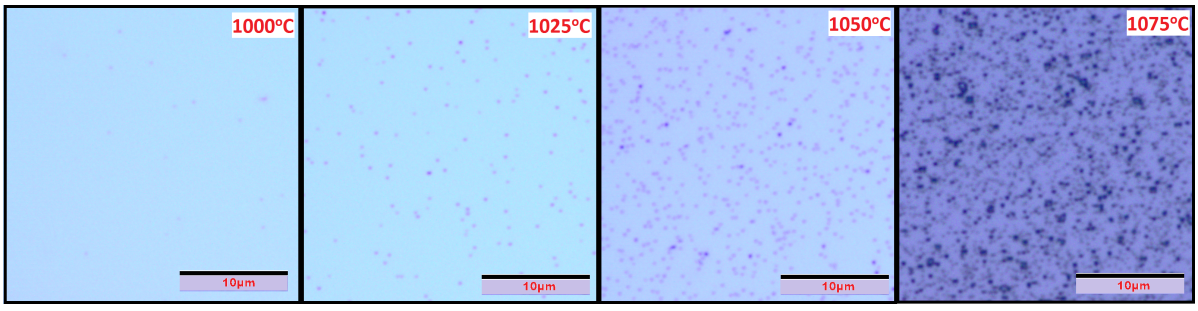

Figure 3.7: Microscopic images of the etch pits in the tunneling oxide at different annealing temperatures (100x).

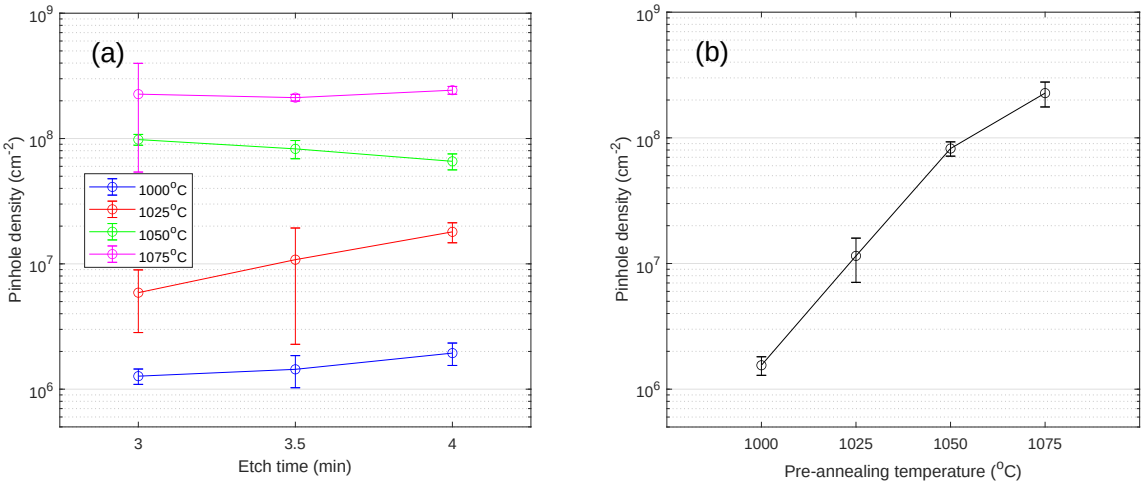

Figure 3.8: Pinhole density determined for (a) three different etch times and (b) averaged for each annealing temperature. The error bars provide the 95% confidence interval of the measurement.

The Figure 3.8a shows the pinhole densities for each individual etch time and annealing condition. It can be seen that the pinhole densities are relatively constant for each etch time, showing a slight increase for 1000^{o}C and 1025^{o}C for longer etch times. This can be explained with Figure 3.6, since the pinholes will probably be smaller for lower annealing temperatures and less actual holes will be present in the SiO_x. The difference in pinhole density between the thermal treatments has become clear, where the pinhole density ranges from 10^6 cm^{-2} at 1000^{o}C to $2{\cdot}10^8$ cm^{-2} at 1075^{o}C.
Figure 3.8b shows the averaged pinhole density for each condition, showing a logarithmic increase of the pinhole density from 1000^{o}C to 1050^{o}C. At 1075$^o C$, this logarithmic increase flattens, which can be explained with Figure 3.7. Figure 3.7 shows microscopic images of the etch pits at the pinhole sites for each annealing temperature at the same etch time. Large differences between the pinhole densities can be observed, while also the size of the etch pits are different. For higher temperatures, the etch pits show to be larger, sometimes merging with neighboring etch pits, which will result in an underestimation of the pinhole density. It shows that the SiO_x layer is almost saturated with pinholes, so an increase in temperature will probably result in complete break-up of the layer.

3.5. Discussion

Based on these results, the impact of a high temperature annealing step (>1000^{o}C) on the carrier transport in poly-Si passivating contacts can be estimated. At 1000^{o}C, the pinhole density is relatively low (~10^6 cm^{-2}), but according to Wietler et al. and Peibst et al. this pinhole density will already significantly influence the carrier transport [22, 24]. However, comparing the lower to the higher temperature range, the lower temperature range with smaller pinhole density will show a higher resistivity [59].
On the other hand, the samples prepared at 1050^{o}C and 1075^{o}C show a high pinhole density. This will result in a very low resistivity, but the recombination current density will be higher [59]. This will be especially for 1075^{o}C, since the microscopic images have shown that this annealing treatment has almost broken up the oxide. It is thus expected that J_0 will be relatively high if annealed at 1075^{o}C, due to the high pinhole density.
The pinhole density after 1025^{o}C annealing is in between, which could be the optimal amount of pinholes to balance J_0 and ρ_c in the contact. The pinhole density is approximately 10^7 cm^{-2}, which is in the range for pinhole-assisted carrier transport combined with tunnelling transport [24], since the oxide is only 1.43 nm.
Considering the dopant diffusion from the doped poly-Si into the c-Si bulk through the SiO_x, it is expected that more dopants can diffuse into the bulk when the pinhole density is higher. Thinner regions of the SiO_x or actual holes in the layer provide a path for the diffusion of dopants, so it is expected that differences can be seen in the shape of the dopant profiles.

3.6. Summary

Selective TMAH etching has shown to be an effective method to detect pinholes in the SiO_x layer of poly-Si passivating contacts. Flat samples with a 1.43 nm dry thermal oxide have shown to result in a pinhole density of ~$8{\cdot}10^8$ cm^{-2} when the contact is annealed for 1050^{o}C for 1 minute. The detection range for accurate pinhole detection was determined to be 3-4 minutes of etching, which mostly excludes the impact of quasi-pinholes or merging pinholes on the pinhole density measurement.
The pinhole density was determined for contacts that were subjected to annealing temperatures of 1000-1075^{o}C with steps of 25^{o}C. The measurement results have shown an exponential increase of the pinhole density for increasing annealing temperatures. The pinhole density range that was measured is 10^6-$2{\cdot}10^8$ cm^{-2}, which is in the optimal operation range for poly-Si contacts, according to simulations on pinhole-assisted carrier transport [24].
Following up on these findings, it is expected that the higher pinhole densities, created by 1050^{o}C and 1075^{o}C, will result in an increased recombination at the interface and will result in more excessive dopant diffusion into the c-Si bulk. Lower pinhole densities, as for the 1000^{o}C and 1025^{o}C, will probably result in less recombination at the interface compared to the higher temperature range. The chemical surface passivation will be better, since the oxide is more intact. If the tunnelling transport for lower pinhole densities is more than for higher pinhole densities, this could result in increasing values for the contact resistivity for contacts with decreasing pinhole density.

4

Ion implanted LPCVD poly-Si passivating contacts

Research has been ongoing for several years in many research groups to improve the poly-Si based passivating contacts towards industrial application quality. Since some processing steps that result in high quality contacts are not yet industrially applicable, optimal experimental conditions can be specific for each research group and piece of equipment. Optimal conditions are also strongly dependent on a certain contact configuration, including layer thickness, deposition type and temperature treatments.
This section comprises of the experimental investigation of poly-Si based passivating contacts processed by the implantation of dopants ions. The passivation quality was investigated for a wide range of annealing conditions. This included the formation of pinholes, which was performed by the introduction of an additional annealing step. First, the purpose and setup of this experimental section will be explained, after which the results and discussion will be presented.

4.1. Goals and experimental setup

In the fabrication of poly-Si based passivating contacts, a high temperature annealing step has always been crucial for contact formation. This high temperature annealing involved several physical means, for example the crystallization of the a-Si:H to poly-Si, but also the formation of pinholes in the SiO_x tunnelling layer. Furthermore, the dopants inside the a-/poly-Si layer need to be activated to become electronically active in the contact. While both P and B atoms require a relatively high temperature to be activated ($>800^oC$, [61]), the dopants will also diffuse at this temperature. A returning downside of this high temperature annealing after dopant introduction has been the dopant diffusion into the c-Si bulk. Excessive diffusion of the dopants will introduce defects and reduce the passivating effect of the SiO_x/poly-Si structure [62].
Considering this, it could be beneficial to separate the pinhole formation part from the dopant activation. This implies the introduction of an extra high temperature annealing step before doping of the a-/poly-Si. This could minimize the dopant diffusion into the c-Si bulk, but still use the concept of pinhole transport. Annealing after doping will be referred to as post-annealing, where annealing before doping will be referred to as pre-annealing to quickly relate to this processing step.
By changing time and temperature of these pre- and post-annealing steps, this experiment will try to show which combinations of these temperature treatments results in the best passivation for the chosen contact structure. As a comparison, a complete batch of samples is processed without performing this pre-annealing step. To explain the impact of the pre-annealing step on the passivation with respect to the tunnelling oxide, the results from 'Pinhole density in LPCVD poly-Si contacts' (Chapter 3) are used.

As mentioned, the post-annealing step is used to activate the dopants, but at high temperatures the dopants are also diffusing into the contact and c-Si. When too much dopants diffuse into the bulk, the functionality of field-effect passivation decreases. This causes the passivation quality of the contact to decrease. It is thus important to compare the measure of dopant diffusion when comparing the different post-annealing conditions. This makes the time and temperature profile of certain annealing conditions

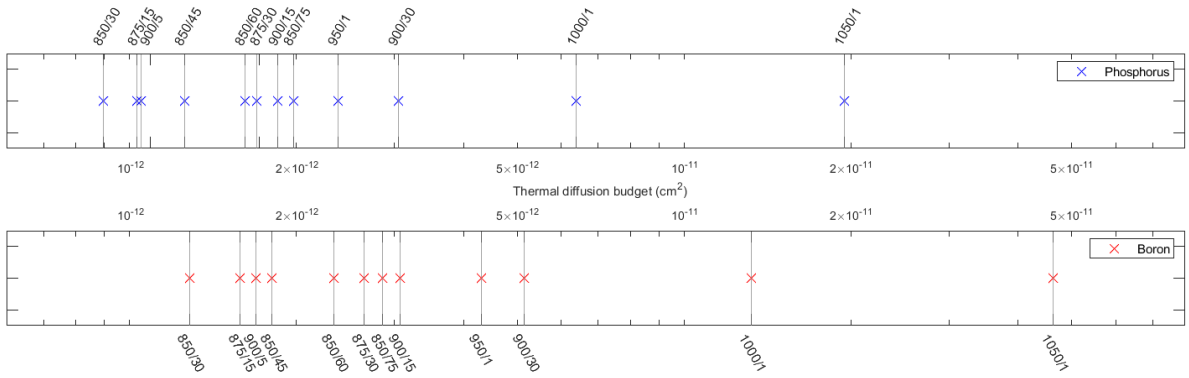

Figure 4.1: Thermal diffusion budget scale for all post-annealing conditions investigated in this experimental section.

important to define the thermal diffusion budget (TB) of a particular annealing condition.
It has been proposed by Regner et al. [63] that the thermal diffusion budget of a certain temperature treatment for a certain time window can be defined as:

$$TB_i = D_{0,B/P} e^{-\frac{E_a}{k_B T_i}} \cdot t_i \equiv L_D^2 \tag{4.1}$$

where $D_{0,B/P}$ is the diffusion constant for Boron or Phosphorus atoms, E_a is the activation energy of Boron or Phosphorus, t_i is the time window, k_B is Boltzmann's constant and L_D is the diffusion length. This equation shows that the thermal diffusion budget is actually expressed by the diffusion length squared (L_D^2), which is why the unit of TB will be cm^2. Considering the temperature profiles, starting from 600^{o}C and rising with 10^{o}C/min, the total thermal diffusion budget is calculated by the integral of every time step.

$$TB = \int_t D_{0,B/P} e^{-\frac{E_a}{k_B T(t)}} \cdot dt \tag{4.2}$$

For the calculation of TB, the temperature profiles are considered as described in 'Fabrication' (Chapter 2). With some post-annealing conditions varying in temperature and time, it can be difficult to compare the results to each other. With this definition of thermal diffusion budget, these conditions can be compared based on the measure of diffusion. Since P and B atoms have different diffusion constants and activation energy, the distribution of the chosen post-annealing conditions is much different for B and P. Figure 4.1 shows the calculated thermal diffusion budget of all post-annealing conditions, where 850/30 is short for a thermal treatment at 850^{o}C for 30 minutes at this peak temperature. Table 4.1 shows the diffusion constants and activation energies in c-Si that were considered in the calculation of the thermal diffusion budget [27].

Table 4.1: Input parameters D_0 and E_a of P and B in c-Si for the calculation of the thermal diffusion budget [27].

	D_0 (cm^2/s)	E_a (eV)
Phosphorus	$8{\cdot}10^{-4}$	2.74
Boron	0.06	3.12

It is expected that there will be a correlation between the passivation quality and the thermal diffusion budget of the post-annealing condition. Electrochemical Capacitance-Voltage (ECV) measurements could confirm this, by measuring the concentration profile of the activated dopant atoms in the contact and bulk. A high concentration of diffused dopants in the bulk could mean that the field-effect passivation has decreased and that there is a higher defect density causing a lower chemical passivation quality.
ECV measurements are performed to gain insight into the relation between dopant distribution and passivation quality and/or pinhole density. The passivation quality of the samples was measured using photoconductance lifetime measurements. A Sinton WCT-120 lifetime tester was used, where J_0 was determined with the Kane and Swanson method [47]. The implied V_{oc} was determined by the calculations proposed by Sinton and Cuevas [45].

4.2. Sample preparation

The processing sequence that has been followed here is based on the fabrication of symmetrical contact structures, where the same contact is built on both sides of the wafer. All samples have been textured first, to maximize the amount of light that is coupled into the solar cell. A schematic overview of the processing sequence is shown in Figure 4.2. As mentioned in 'Fabrication', rounding of pyramidal structures is a part of the texturing process. After texturing the surface has microstructures as well as nanostructures. Immersing the samples in an anisotropic Si etching solution, the sharp pyramids formed during texturing will be smoothened. This will result in a significant drop in defect states at the c-Si/SiO_x/poly-Si interface [33], while still keeping its anti-reflection properties.

To minimize the amount of contaminations and impurities, a standard wet chemical cleaning step is performed. After removing contaminations from the surface, the samples are immersed in HF (0.55%) followed by IPA drying (Maragoni) to remove the native oxide formed during the cleaning process. This ultra-clean surface is then ready to grow the tunnelling oxide on.
The tunnelling oxide is grown in dry thermal oxidation process, as explained in 'Fabrication'. Since the crystal orientation of the textured surface is (111), it could be that the thermal oxidation growth rate is different from the (100) surface. An identical thermal oxidation procedure has been performed on a flat (111) oriented wafer to measure the oxide thickness. Spectral Ellipsometry has determined the oxide thickness on (111) to be 1.36 $\pm$ 0.04 nm.
Immediately after oxidation, a-Si:H is deposited by LPCVD to cover the thermal oxide. The deposition rate on a flat surface is approximately 2.21 nm/min at 580^{o}C with 45 sccm SiH_4 flow, but the target surface is textured. Previous research in the group has proven that the ratio in deposition rate for LPCVD is approximately 1.25:1 for flat:textured, respectively. The target thickness for the a-/poly-Si layer is 100 nm, so the deposition time is chosen to be 60 minutes. In this experiment the exact thickness is not crucial, because all samples are identical. An approximate thickness of 100 nm is chosen, because a thick poly-Si layer results in the best passivation [20]. In this way the influence of the pinholes in the SiO_x on the passivation quality can be studied.

The pre-annealing treatment is done in a tube furnace at high temperatures (1000-1075^{o}C) which will create pinholes in the SiO_x and form poly-Si. Dopants are added into the poly-Si with ion implantation, which already creates a doping profile and breaks most the surface lattice bonds. Phosphorus doping is done with an implantation energy of 20 keV and a dose of 10^{16} cm^{-2}. Boron doping is done with an implantation energy of 5 keV and a dose of $7.5{\cdot}10^{15}$ cm^{-2}. The doping profiles are expected to be similar, calculated from [64].
To activate the dopants and recrystallize the poly-Si layer, post-annealing is done at 12 different conditions, which were already briefly discussed in 'Goals and Experimental setup'. Since both time and temperature of the process can have an impact on the contact quality, several combinations of temperature and time are considered to possibly differentiate between the thermal diffusion budget and

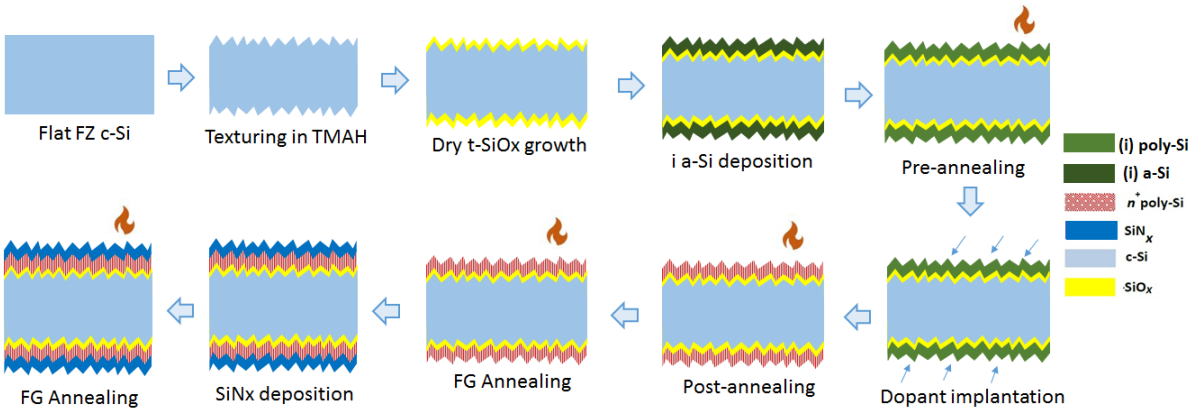

Figure 4.2: Processing sequence to fabricate symmetrical n-type poly-Si based passivating contacts with LP-CVD poly-Si doped by ion implantation. P-type contact were processed identically, where only the dopant implantation was different.

the peak temperature of the process. Table 4.2 shows all post-annealing conditions in this experiment. The passivation quality is determined by lifetime measurements after post-annealing, to monitor the passivation quality in the progress of contact fabrication.

Table 4.2: Post-annealing conditions to investigate the impact of thermal diffusion budget on the passivation of poly-Si passivating contacts.

Peak temperature (^{o}C)	Process time (min)
850	30/45/60/75
875	15/30
900	5/15/30
950	1
1000	1
1050	1

The hydrogenation of the contact involved three steps, Forming gas annealing (FGA) followed by a SiN_x:H deposition and subsequently a second step of FGA. FGA is done in a TEMPRESS tube furnace, for 30 minutes at 400^{o}C. FGA will provide hydrogen to the dangling bonds and defects in the contact and at the interfaces. The passivation quality is measured after the first FGA step to see the impact of hydrogenation on the passivation quality.
An a-SiN_x:H layer is then deposited to act as an anti-reflection layer and hydrogen source. SiN_x is deposited by plasma-enhanced chemical vapor deposition (PECVD) in an Oxford Instruments Plasmalab 80 Plus. The deposition takes place at 400^{o}C, with a SiH_4:NH_3 gas flow of 20:20 sccm. A deposition time of 8 minutes resulted in a 120 nm thick layer on a flat surface, which is comparable to a ~80 nm layer on a textured surface. An FGA treatment is performed immediately after the SiN_x deposition, which finalised the hydrogenation processes. The final passivation quality of the contacts is determined, which can be used to analyse the differences.

4.3. Phosphorus implanted n-type poly-Si based passivating contacts

This section will present the experimental results of n-type ion implanted poly-Si contacts. To compare the results from all different conditions, the proposed concept of thermal diffusion budget is used. Since the implied open-circuit voltage is a measure for the passivation quality, the different pre-annealing conditions are compared in a heat map, where the different post-annealing conditions are projected onto the thermal diffusion budget axis.

Passivation quality for a wide range of annealing conditions

These results are shown in Figure 4.3, where the red color indicates a higher implied open-circuit voltage (iV_{oc}). Mentioned earlier, the passivation was also measured with 1050^oC post-annealing. However, the passivation results from this batch were significantly lower than the other results, so much lower that the heat map could not show any differences between the other conditions. Thus not relevant, these results are left out of the heat map for analysis purposes.
The maximum iV_{oc} was found for the sample prepared with 1000^oC pre-annealing and 875/15 post-annealing and it resulted in an iV_{oc} of 729.8 mV. Table 4.3 shows the best obtained passivation for combinations of pre-annealing and post-annealing, where the corresponding J_0 is also noted. These results are compared to two experimental results from literature with similar process flows [65, 66]. This comparison shows that the passivation quality of the n-type contacts is comparable to literature, since this small difference of several mV could be explained by the thicker poly-Si that provides better passivation.

The obtained values for iV_{oc} are calculated from lifetime data, so there is always a measure of uncertainty. This makes it probably better to observe trends rather than only looking at the absolute maximum of these measurements. An important result from this experiment is that the passivation

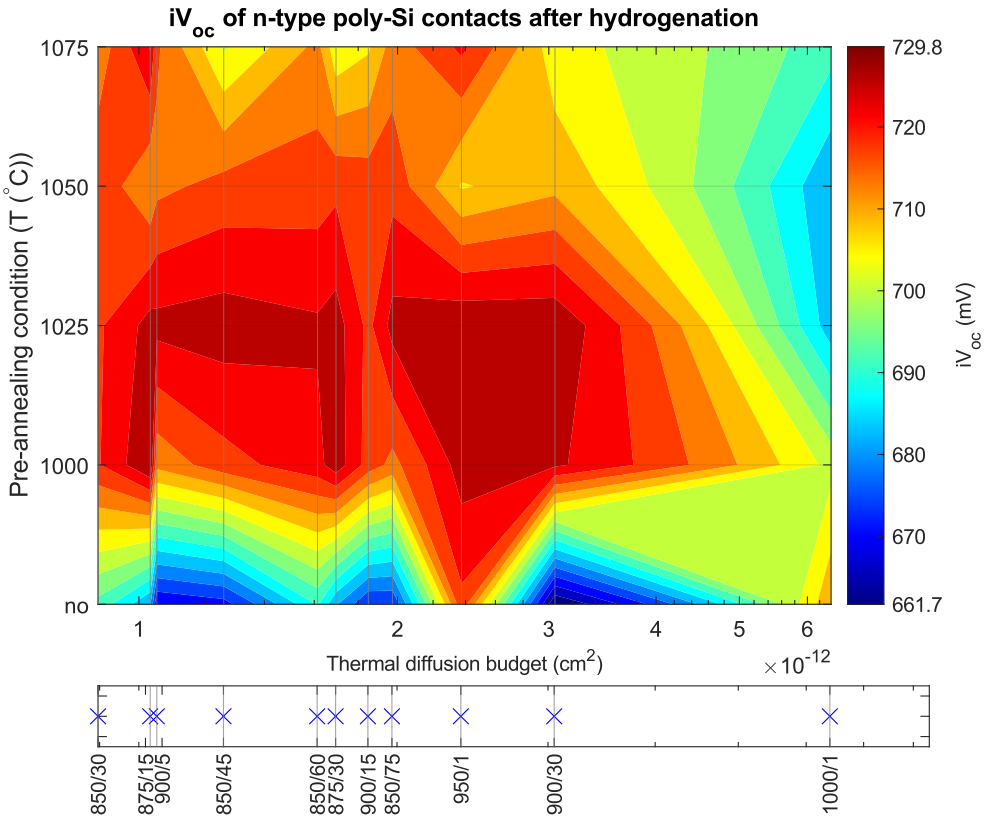

Figure 4.3: Passivation quality in terms of iV_{oc} of the phosphorus-doped poly-Si based passivating contacts after hydrogenation. Post-annealing conditions are compared by the thermal diffusion budget on the x-axis.

Table 4.3: Best passivation results achieved for phosphorus implanted poly-Si contacts with pre-annealing before implantation. As a comparison, state-of-the-art values from literature are presented from double-side textured samples, which followed a similar process flow.

Literature		iV_{oc} (mV)	J_0 (fA/cm^2)
ThOx + 200nm LPCVD poly-Si [66]		736	3.0
ThOx + 200nm LPCVD poly-Si [65]		732	4.2
Pre-annealing	Post-annealing		
1000^{o}C	875/15	729.8	5.3
1025^{o}C	950/1	729.3	5.7
1025^{o}C	900/30	729.0	5.7
1000^{o}C	875/30	728.1	5.1

is significantly lower for the samples that did not undergo a pre-annealing step. For some samples, the difference in iV_{oc} is even more than 50 mV compared to the best results, which shows that the pre-annealing can have a positive effect on the passivation quality of the contacts. When performing the 1000^{o}C or 1025^{o}C pre-annealing, a wide range of post-annealing conditions resulted in an iV_{oc} of >715 mV, making this the optimal process window. Figure 4.3 shows that the passivation degrades for 1000/1 post-annealing, which excludes 1000^{o}C post-annealing from the optimal process window for n-type contacts.
In the complete heat map, a large optimal process window for n-type contacts can be observed. For no or the 1075^{o}C pre-annealing treatment or an increase in thermal diffusion budget above $3{\cdot}10^{-12}$ cm^2, the passivation quality decreases, clearly showing a correlation between the thermal diffusion budget, pre-annealing treatment and the passivation quality.

Comparing the passivation quality of samples with and without pre-annealing, the passivation difference is mainly expressed in iV_{oc}, rather than J_0. No significant difference in J_0 can be observed for post-annealing below 1000^{o}C, while the iV_{oc} increases with up to 50 mV for the pre-annealed samples. This result is not expected, because both iV_{oc} and J_0 represent the passivation quality of the sample based on carrier recombination. Since the determination of J_0 is based on fitting the inverse corrected lifetime curve, it is highly sensitive to the excess carrier density at which the fit is created. To qualitatively assess the passivation quality, the effective carrier lifetime curves will be the most accurate, together with the iV_{oc}.

The recombination current densities of all combinations of annealing conditions are added in Appendix B, which shows a large range of conditions where J_0 is lower than 10 fA/cm^2. Some interesting results include low recombination for the samples without the pre-annealing treatment, several post-annealing treatments resulted in a J_0 lower than 7 fA/cm^2. The lowest value for J_0 was measured to be 5.1 fA/cm^2, for the sample subjected to 1000^{o}C pre-annealing and 875/30 post-annealing. The optimal process window considering iV_{oc} is similar to that of the J_0 values. Regarding this optimal process window (1000-1025^{o}C pre-annealing and <1000^{o}C post-annealing), all samples show similar J_0 values ranging from 5.1 fA/cm^2 to 9.6f A/cm^2. Considering there is room for optimization, this process window is suitable for further investigation and optimization of the passivation quality.

Effective lifetime analysis to interpret passivation quality

The effective lifetime curves, extracted with the photoconductance decay lifetime measurement, will be useful to interpret the differences in passivation quality between the different annealing conditions. Figure 4.4 compares the lifetime curves of two pre-annealing conditions and four post-annealing conditions. Two samples are chosen with contradictory high and low thermal budget annealing treatments, 1000/1 and 850/30, respectively. Another two samples subjected to a similar thermal diffusion budget, 875/30 and 900/15, are compared as well. The dotted line shows the lifetime curves of the pre-annealed samples (1025^{o}C) and the solid line represents the samples without pre-annealing. This comparison will show the influence of the presence of pinholes on the effective lifetime of minority charge carriers. Figure 4.4 clearly shows a significant difference in lifetime which is almost an order of magnitude between the dotted and solid lines, for 850/30, 875/30 and 900/15 post-annealing. Except for 1000/1

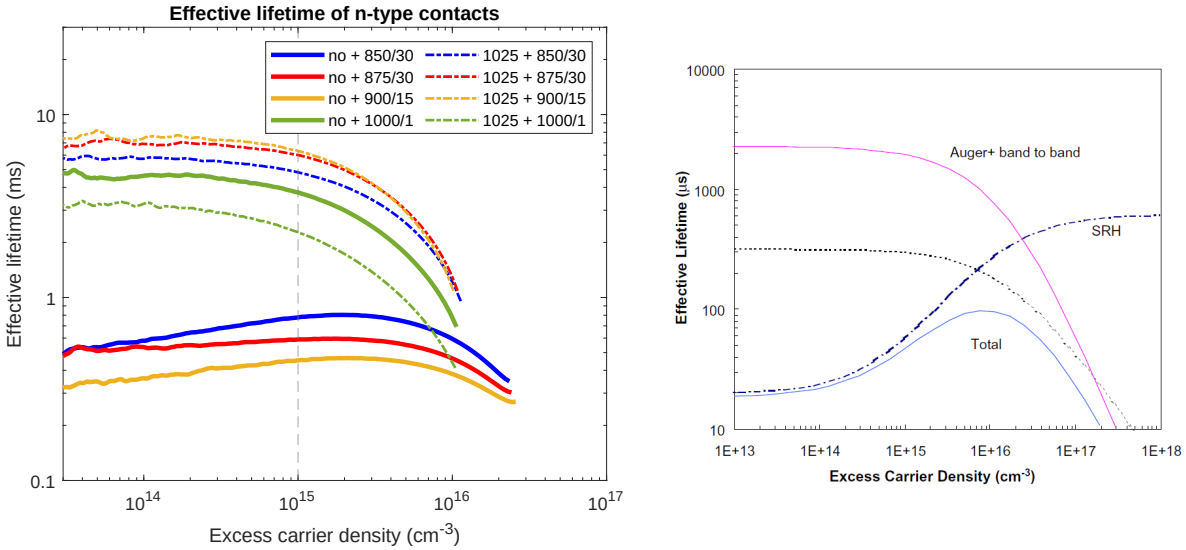

Figure 4.4: (left) Effective lifetime curves for the operating range of excess carrier density. No pre-annealing (solid line) is compared to 1025^{o}C pre-annealing (dotted line), where four post-annealing conditions are compared to interpret the passivation quality in n-type contacts. τ_{eff} is determined at 10^{15} cm^{-3}. (right) Recombination mechanisms that influence the shape of the lifetime curves according to Cuevas and MacDonald [48].

post-annealing, for which the difference in effective lifetime is much smaller and opposite. Since the effective lifetime is a measure of passivation quality, this parameter can be compared to the recombination current density J_0 and iV_{oc}.
The lifetime curve of the '1025^{o}C + 1000/1' shows to be much lower than the curves with the same pre-annealing condition. This could point to excessive dopant diffusion into the bulk through the pinholes already present in the tunnelling layer, or interface degradation caused by SiO_x rearrangement, e.g. extra pinhole formation. For the 'no + 1000/1' case, the pinhole formation and dopant diffusion/activation is combined into one processing step. Figure 4.4 shows that this results in a lower passivation than the '1025 + 850/30' combination of conditions that includes the lowest thermal diffusion/activation budget.

A shape change is visible in the lifetime curve for the samples that are assumed to contain pinholes in the tunnelling layer. This implies that different recombination mechanisms are dominant in these contacts. Using the lifetime curve interpretation from Cuevas and MacDonald [48], Auger recombination is dominant at high excess carrier densities and at high doping, where SRH recombination is dominant for lower excess carrier densities and high defect densities. No pre-annealing in combination with 850/30, 875/30 or 900/15 post-annealing demonstrates that both Auger and SRH recombination affect the shape of the lifetime curve, based on the findings of Cuevas and MacDonald [48]. The shape of the other lifetime curves demonstrates that Auger recombination is dominant at the interface. This indicates that the interface trap density (D_{it}) of the c-Si is low, resulting in a negligible SRH recombination contribution.

The passivation difference could be explained by local in-diffusion of dopants through existing pinholes. When looking at the theoretical approximations of SRH and Auger recombination [6], the dominance of Auger recombination is expected, since it scales with $\sim N_{dop}^2$ and the in-diffused area contains much higher doping levels than the surrounding areas. SRH recombination scales with the trap density ($\sim N_T$), which is higher at the pinhole sites. However, the E-field that is increased locally by the dopants will repel minority carriers from the pinholes sites, reducing SRH recombination.

Thermal diffusion budget compared to doping profiles

To be able to link the thermal diffusion budget to actual dopant diffusion into the c-Si bulk, ECV measurements have been performed on a selection of samples from the passivation experiment, which will reveal a depth profile of the concentration of activated dopants in the contact and bulk. As this experimental section is comparing pre-annealing conditions and post-annealing conditions, two sample series were selected. The first series takes three types of pre-annealing, with the same post-annealing

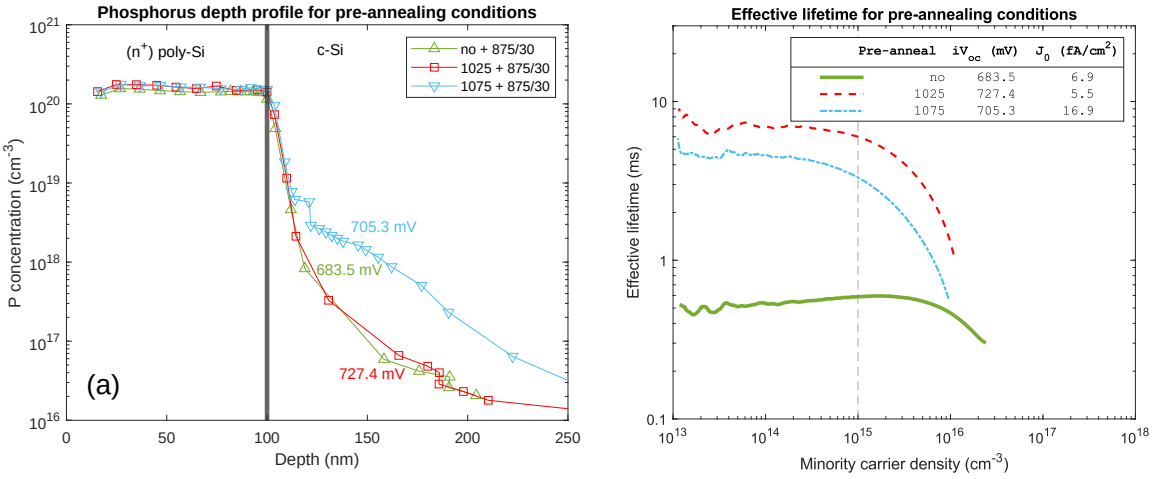

Figure 4.5: (a) Phosphorus depth profiles in ion implanted poly-Si contacts. Three pre-annealing conditions are compared with a fixed 875/30 post-annealing. The poly-Si/SiO_x/c-Si interface is marked by the black line. (b) Effective lifetime curves of the samples in (a) after hydrogenation. The corresponding values of iV_{oc} and J_0 are added in the legend.

treatment (875/30) and the second series takes another three types of post-annealing, all with the same pre-annealing condition (1025^{o}C).

Figure 4.5a shows the doping profiles of three samples, which are compared by their pre-annealing conditions, while the post-annealing condition was identical for all. The c-Si/SiO_x/poly-Si interface is marked at 100 nm, which is the expected thickness of the poly-Si. The dopant distribution in the n^+-poly-Si shows to be uniform, where the dopant concentration is around $1.5{\cdot}10^{20}$ cm^{-3}. This confirms the high doping level of the poly-Si layer. At the interface, there is a sharp drop in P concentration for all contacts. However this drop is much less for the contact with 1075^{o}C pre-annealing, which implies excessive dopant diffusion in the c-Si bulk. The pinhole detection experiment has shown that the oxide layer is close to breaking up at 1075^{o}C (Figure 3.7), which explains why dopants can diffuse more into the c-Si. Already at 50 nm in the c-Si, there are >10x more dopants present when compared to the other samples. This dopant diffusion has resulted in a significant drop in iV_{oc} when compared to the sample with 1025^{o}C pre-annealing.

Figure 4.5b shows the effective lifetime curves that belong to the samples of which the dopant profile is shown in Figure 4.5a. The corresponding iV_{oc} and J_0 are noted inside. When comparing iV_{oc} and J_0 with the dopant profiles, two conclusions can be drawn. First, the excessive dopant diffusion into the bulk has affected the passivation quality of the sample with 1075^{o}C pre-annealing. The shape of the lifetime curve point towards a larger contribution of Auger recombination, which is then caused by the higher doping concentration in the bulk, resulting in a lower τ_{eff} and higher J_0. Second, the sample without pre-annealing shows an excellent passivation quality in terms of J_0, but a rather low iV_{oc}. This could be explained by the fact that the oxide is still intact for this sample. Uniform tunnelling transport will occur, relying on the E-field created by the poly-Si to repel minority carriers. Without local in-diffusion of dopants, the internal E-field will be less strong, resulting in a higher minority carrier concentration at the interface. When some minority carriers still reach the interface, they can either recombine in defects (SRH recombination) or by Auger recombination. However, then it would also be expected that J_0 is higher.

A similar comparison of dopant concentration profiles can be made in a post-annealing series, where all samples have undergone the same pre-annealing treatment (1025^{o}C). As already shown in Figure 4.5a, the moderate pinhole density formed in the 1025^{o}C pre-annealing process does not contribute to dopant diffusion into the bulk for a post-annealing with an average thermal diffusion budget. Figure 4.6a shows that the 1000/1 condition results in excessive dopant diffusion, which is more than that for the '1075 + 875/30' conditions. At 1000^{o}C, the SiO_x will rearrange further, while simultaneously adding a high thermal diffusion budget to the contact. It has resulted in passivation degradation, which

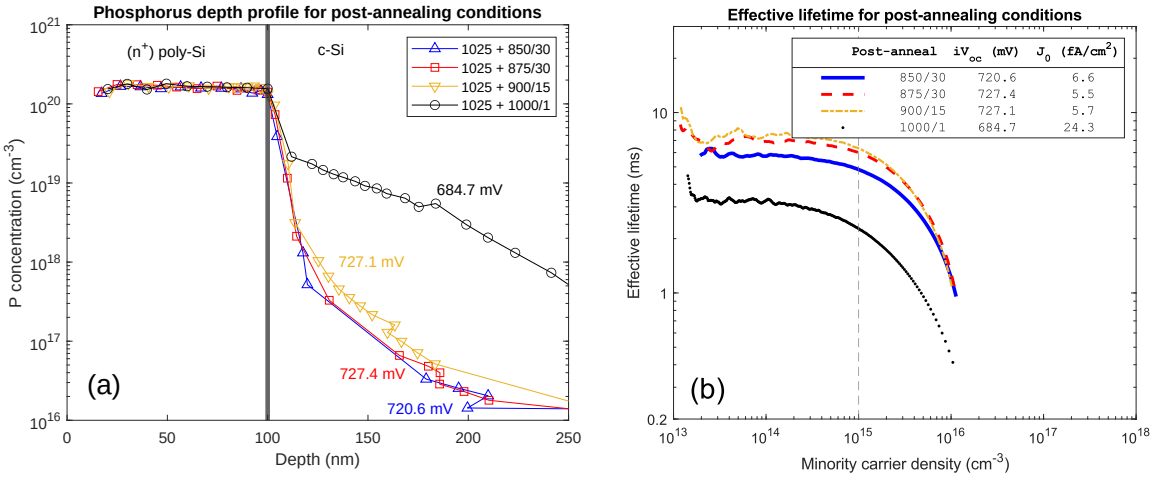

Figure 4.6: (a) Phosphorus depth profiles in ion implanted poly-Si contacts. Four post-annealing conditions are compared with a fixed 1025^{o}C pre-annealing. The poly-Si/SiO$_x$/c-Si interface is marked by the black line. (b) Effective lifetime curves of samples in (a) after hydrogenation. The corresponding values of iV_{oc} and J_0 are shown in the legend.

is represented by its iV_{oc} and J_0, 684.7 mV and 24.3 fA/cm^{-2} respectively.

Comparing the 875/30 and 900/15 post-annealing conditions can be useful, since their thermal diffusion budget is similar. Figure 4.6a shows that the dopant diffusion into the bulk for 900/15 is slightly higher, however not resulting in a decreased lifetime yet. This result shows that excessive dopant diffusion starts to happen from this thermal diffusion budget combined with 1025^{o}C pre-annealing, while it does not yet influence the passivation quality.

Pinhole-enhanced passivation in n-type poly-Si contacts

When comparing samples with and without pre-annealing (pinholes), as shown in Figure 4.4, it can be interpreted that there are different recombination mechanisms at the contact interface. Auger recombination in samples with pinholes points to a role of dopants in the carrier transport, since Auger recombination scales quadratically with dopant concentration ($\sim N_{dop}^2$).

To explain this difference in passivation, increased carrier transport through pinholes is considered. Dopant atoms will always diffuse into the bulk to some extent, even if the oxide is still intact. But when pinholes are present, there will be paths for dopant atoms to diffuse more and faster through the tunnelling layer. This will create a locally diffused area around the pinhole, which induces a higher internal field that contributes to the contact performance in terms of passivation and carrier transport. The higher conductivity and E-field around the pinhole will create a current path for the majority carriers into the poly-Si, while repelling the minority carriers from the pinhole sites. This is necessary, since the pinhole sites are usually significant recombination centers. A comparison of the carrier transport across the c-Si/SiO$_x$/(n$^+$)poly-Si interface is shown in Figure 4.7. Figure 4.7a

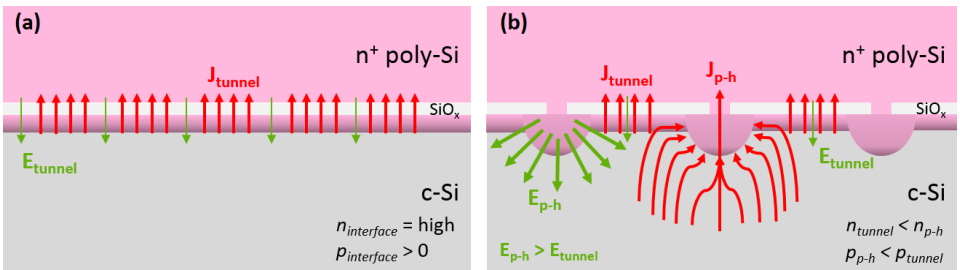

Figure 4.7: Schematic of the carrier transport in an n-type poly-Si contact through (a) an intact SiO$_x$ layer and (b) a SiO$_x$ layer with pinholes. Abbreviation p-h, n and p represent pinhole, electron concentration and hole concentration, respectively.

represents an intact SiO_x layer, where the carrier transport is assumed to be homogeneous. Figure 4.7b shows the aforementioned case, where the E-field is enhanced at the pinhole sites, which increases the majority carrier transport to the poly-Si and repels the minority carrier concentration at these pinhole sites.
This additional local diffusion is probably not visible in the ECV measurements, since the ECV profile provides the average dopant concentration of a relatively large area. The size of pinholes is usually in the order of nm, so the areal fraction of these pinholes is negligible. This results in a negligible contribution of these sites to the ECV dopant profiles.

4.4. Boron implanted p-type poly-Si based passivating contacts

The approach for the analysis of the passivation quality of p-type passivating contacts was similar to that of the n-type contacts. All post-annealing conditions are projected on the thermal diffusion budget axis and the passivation quality (in terms of iV_{oc}) after different pre-annealing conditions is compared in a heat map. Note that the distribution of post-annealing conditions for p-type contacts is slightly different on the x-axis than for n-type contacts, since the thermal diffusion budget distribution for boron is different from phosphorus.

Passivation quality for a wide range of annealing conditions

Figure 4.8 shows an overview of the passivation quality after hydrogenation for all combined annealing conditions, where the red color represents a high passivation quality. The measured iV_{oc} clearly shows a decrease in passivation for the samples prepared with 1000/1 post-annealing condition, where iV_{oc} drops with around 30 mV compared to the red areas. The samples processed without the pre-annealing step show also significantly lower passivation quality, which is roughly 15 mV lower than the best obtained passivation quality in this sample series.

It can be seen in Figure 4.8 that the post-annealing conditions have slightly more impact on the passivation quality than the pre-annealing conditions, since several vertical red areas are present in the heat map. Compared to the n-type contacts, p-type contacts seem to result in a high passivation quality for certain specific post-annealing conditions, rather than showing a high passivation quality for a wide process window. However, p-type contacts show an $iV_{oc} > 680$ mV for 1000-1050^{o}C pre-annealing and $<$1000^{o}C post-annealing. The overall passivation quality of the p-type contacts show not to be of high quality when compared to state-of-the-art double-side textured p-type contacts (Table 4.4, [65, 67]), which shows a gap of $>$10 mV and $>$10 fA/cm^2 in lesser passivation quality. This can be explained by the choice of hydrogenation procedure in this experiment for the p-type contacts, since an AlO_x/SiN_x stack can result in iV_{oc} values above 700 mV for in combination with FGA [13]. Nevertheless, the impact

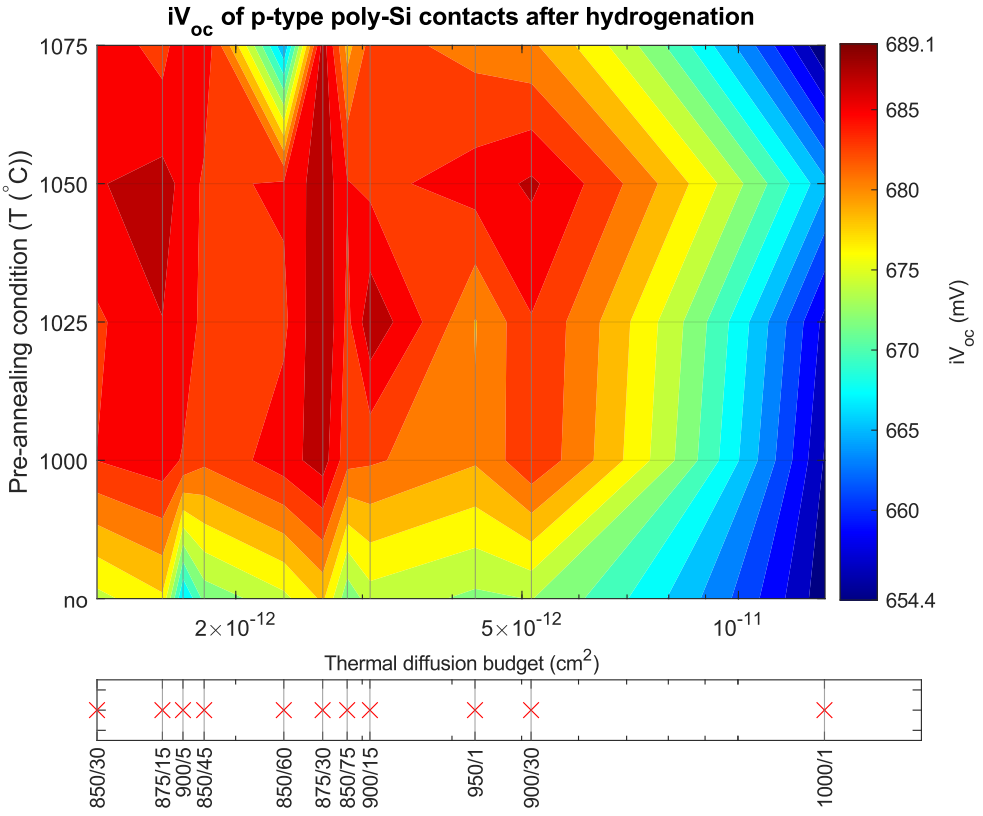

Figure 4.8: Passivation quality in terms of iV$_{oc}$ of the boron-doped poly-Si based passivating contacts.

Table 4.4: Best passivation results achieved for boron implanted poly-Si contacts with pre-annealing before implantation. As a comparison, state-of-the-art values from literature are presented from double-side textured samples, which followed a similar process flow.

Literature		iV_{oc} (mV)	J_0 (fA/cm^2)
ThOx + 150nm LPCVD poly-Si [67]		705	21
ThOx + 200nm LPCVD poly-Si [65]		703	25
Pre-annealing	Post-annealing		
1025^{o}C	875/30	689.1	37.3
1025^{o}C	900/15	688.5	38.0
1050^{o}C	875/30	688.4	38.6
1075^{o}C	875/30	688.1	36.3

of pre-annealing on the passivation quality of p-type poly-Si contacts can still be assessed.

The best passivation quality was achieved for the sample prepared with 875/30 post-annealing, combined with 1000-1075^{o}C pre-annealing. This particular post-annealing condition resulted in an iV_{oc} of 688.0-689.1 mV for the samples that had undergone pre-annealing. The maximum passivation was achieved for the sample subjected to 1025^{o}C pre-annealing and 875/30 post-annealing, resulting in an iV_{oc} of 689.1 mV and a J_0 of 37.3 fA/cm^2. These results show that a combination of pre-annealing and 875/30 post-annealing is the optimal combination to achieve high passivation in p-type ion-implanted poly-Si contacts. The passivation degradation at the 1000^{o}C post-annealing could be explained by the high diffusion constant of boron, which could cause a deep dopant diffusion into the bulk. It could thus be said that the passivation degrades for a thermal diffusion budget exceeding $6{\cdot}10^{-12}$ cm^2.

The experimental results have shown that there is a significant difference in passivation quality between samples with and without pre-annealing ($\geq$ 10 mV). The passivation in the p-type contacts shows to improve significantly by the presence of pinholes, which can enhance the surface passivation. For post-annealing below 1000^{o}C, the iV_{oc} increases with at least 10 mV when pre-annealing is done. This shows that the impact of the pinholes on the passivation quality is less for p-type contacts than that for n-type contacts. This difference in passivation is similarly expressed in the recombination current density J_0, where a decrease of at least 20 fA/cm^2 was observed when applying pre-annealing. For 1000^{o}C post-annealing, the passivation quality shows to be low, independent of the pre-annealing temperature (e.g. pinhole density). It stresses the sensitivity of the p-type contacts to the post-annealing thermal diffusion budget compared to that of the n-type contacts.

Effective lifetime analysis to interpret passivation quality

To go further into the passivation differences for the range of pre- and post-annealing conditions, it is useful to look at the effective minority lifetime curves of a selection of annealing conditions. Figure 4.9 compares the lifetime curves of two pre-annealing conditions and four post-annealing conditions. Similarly to the n-type contacts, two conditions show contradictory high and low thermal diffusion budget annealing treatments, 1000/1 and 850/30, respectively. Two other post-annealing conditions (875/30 and 900/15) with a similar thermal diffusion budget are compared as well. The dotted line shows the lifetime curves for 1025^{o}C pre-annealing and the solid line represents no pre-annealing. This comparison will show the influence of the presence of pinholes on the effective lifetime of minority carriers in the samples. The different colors show the post-annealing conditions, with increasing thermal diffusion budget.

The lifetime curves in Figure 4.9 show that the effective lifetime is mainly determined by the post-annealing condition which is responsible for dopant activation and diffusion. Comparing no pre-annealing to 1025^{o}C pre-annealing, it becomes clear that the lifetime increases when applying pre-annealing. These are results that are consistent with the iV_{oc} values from Figure 4.8. The lowest effective lifetime is obtained when post-annealing at 1000^{o}C is performed, which can be explained by excessive dopant diffusion into the c-Si. Boron can cause many defects in the c-Si and SiO_x, while simultaneously decreasing the field-effect passivation. The effective lifetime seems to be less dependent

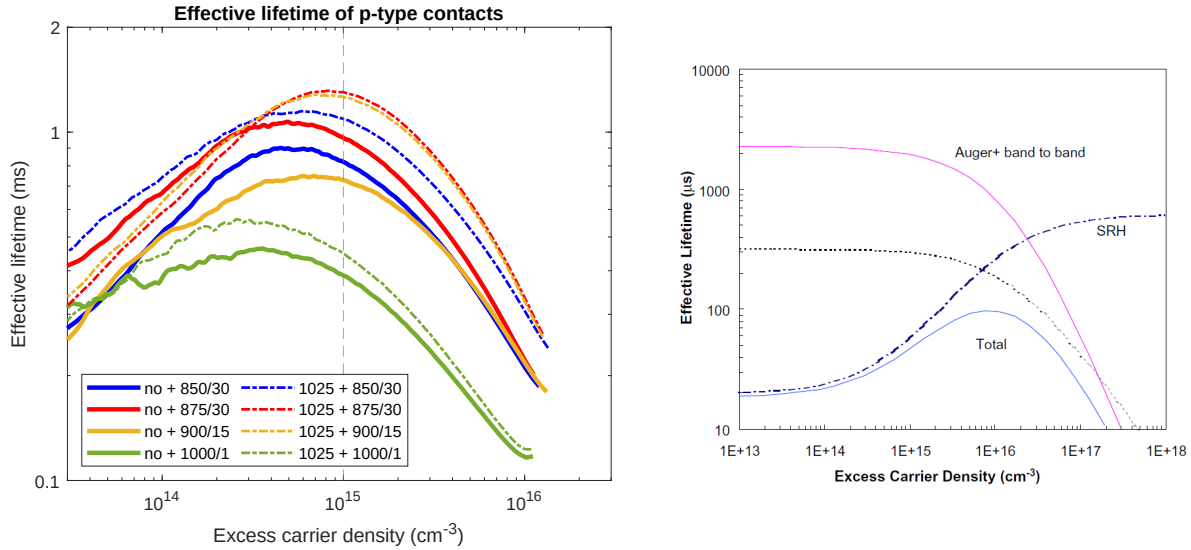

Figure 4.9: (left) Effective lifetime curves for the operating range of excess carrier density. No pre-annealing (solid line) is compared to 1025^{o}C pre-annealing (dotted line), where four post-annealing conditions are compared to interpret the passivation quality in p-type contacts. τ_{eff} is determined at 10^{15} cm^{-3}. (right) Recombination mechanisms that influence the shape of the lifetime curves according to Cuevas and MacDonald [48].

on the specific thermal diffusion budget for the samples with 1025^{o}C pre-annealing, since $\tau_{eff} >$ 1 ms for post-annealing below 1000^{o}C.
For the samples without pre-annealing, the 875/30 post-annealing results in the highest effective lifetime where slight decreases can be seen for 850/30 and 900/15. It is expected that the 875/30 post-annealing condition is the best trade-off between dopant activation and diffusion, which are usually beneficial and detrimental for the passivation quality, respectively. The dopant diffusion profiles measured by ECV should provide more insight into this.

The shape of the effective lifetime curves is similar for all samples, which could imply that the minority carrier lifetimes of all samples are limited by the same recombination mechanism. Comparing these results to the the lifetime curve interpretation by Cuevas and MacDonald [48], it can be concluded that SRH recombination is dominant below an excess carrier density of 10^{15} cm^{-3}. This indicates that the interface trap density D_{it} is probably higher than in n-type contacts, induced by the boron atoms that create defects in the c-Si lattice and interfacial SiO_x. This hypothesis can be confirmed by the dopant depth profiles obtained with ECV measurements.

Thermal diffusion budget compared to doping profiles

The thermal diffusion budget has shown to impact the passivation quality quite significantly, so the dopant profiles could confirm the occurrence of excessive dopant diffusion into the c-Si bulk. The dopant depth profiles are measured with ECV measurements, which will reveal the amount of activated boron inside the contacts. For this experiment, the identical pre- and post-annealing conditions are chosen with respect to the n-type contacts. A series with constant post-annealing (875/30) compares the influence of the pinhole density on the dopant diffusion. Another series with fixed pre-annealing condition (1025^{o}C) will compare the thermal diffusion budget to the actual dopant diffusion into the c-Si.

Figure 4.10a show three dopant profiles, where the post-annealing condition is kept constant for all samples. 1025^{o}C and 1075^{o}C pre-annealing are compared to no pre-annealing. The c-Si/SiO_x/poly-Si interface is marked at 100 nm, which is the expected thickness of the poly-Si. The dopant distribution show to be not very uniform, as accumulation of dopants at the surface and at the interface can be seen for all samples. The dopant concentration is approximately 1.5·10^{20} cm^{-3} in the p$^+$-poly-Si, which is similar to the doping level in the n$^+$-poly-Si. At the surface, the doping level is 2-3· 10^{20} cm^{-3} and at the interface it is approaching 2·10^{20} cm^{-3}, showing accumulation of dopants at the SiO_x interface.

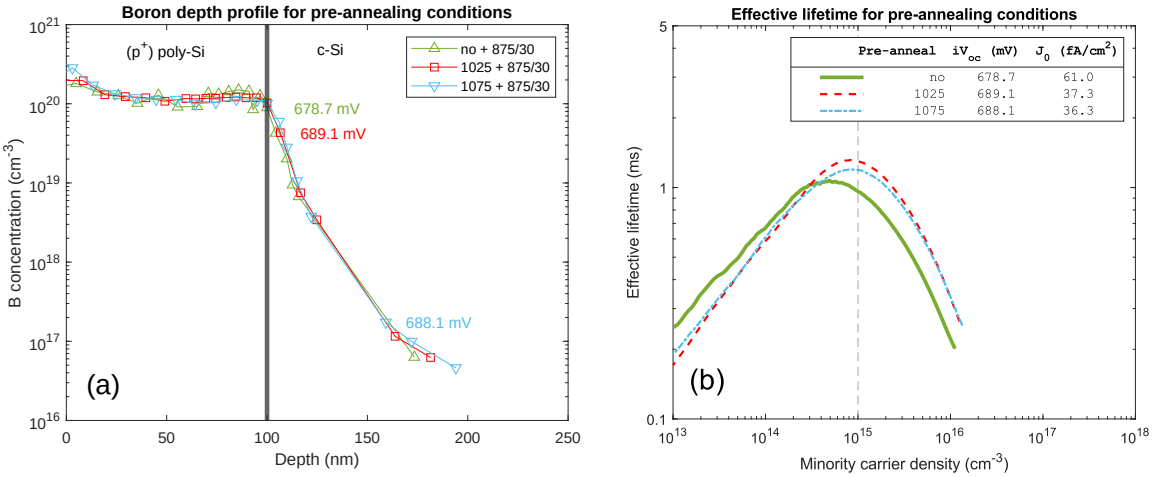

Figure 4.10: (a) Boron depth profiles in ion implanted poly-Si contacts. Three pre-annealing conditions are compared with a fixed 875/30 post-annealing. The poly-Si/SiO_x/c-Si interface is marked by the black line. (b) Effective lifetime curves of the samples in (a) after hydrogenation. The corresponding values for iV_{oc} and J_0 a shown in the legend.

From the interface, a drop in dopant concentration can be seen, reducing over one order of magnitude in the first 20 nm of c-Si. It can be seen that the dopant profiles are similar for all pre-annealing conditions. This shows that pinholes in the SiO_x do not significantly influence the diffusion of boron into the c-Si. Similarly, a pre-annealing treatment does not change the diffusion barrier properties of the SiO_x. However, a notable difference in passivation quality is measured for the sample that did not undergo pre-annealing. Figure 4.10b shows the effective lifetime curves of the corresponding ECV profiles, where the values of iV_{oc} and J_0 are also shown to aid in the interpretation of the data. A lower peak for the samples without pre-annealing points to the active contribution of pinholes in passivation quality improvement of p-type contacts. The decrease in passivation is expressed in both iV_{oc} and J_0, which are ~10 mV and ~25 fA/cm^2, respectively.

A comparison of the post-annealing conditions is also made, of which the dopant depth profiles are shown in Figure 4.11a. The samples from this series have all undergone a 1025^{o}C pre-annealing treatment. Already shown in Figure 4.10a, the pre-annealing treatment does not contribute to excessive dopant diffusion into the c-Si for a post-annealing condition with an average thermal diffusion budget.

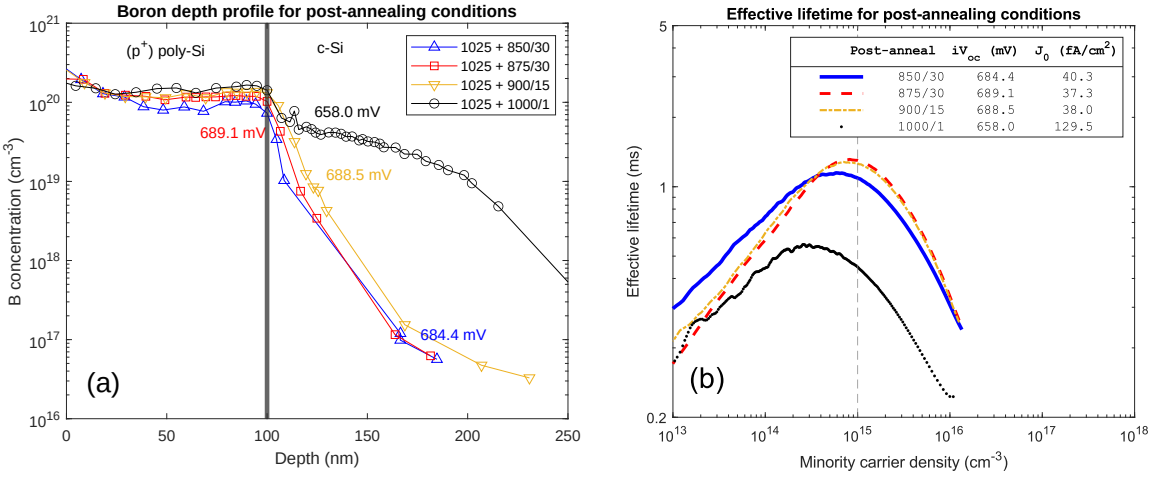

Figure 4.11: (a) Boron depth profiles in ion implanted poly-Si contacts. Four post-annealing conditions are compared with a fixed 1025^{o}C pre-annealing. The poly-Si/SiO_x/c-Si interface is marked by the black line. (b) Effective lifetime curves of the samples in (a) after hydrogenation. The corresponding values for iV_{oc} and J_0 a shown in the legend.

Figure 4.11a shows that the post-annealing thermal diffusion budget influences the activated dopant distribution inside the poly-Si. For increasing thermal diffusion budget, the dopant distribution in the poly-Si becomes more uniform, where the amount of activated dopants (e.g. the doping level) almost doubles when comparing the lowest (850/30) to the highest (1000/1) thermal diffusion budget. Considering the field-effect passivation of the passivating contact, a high doping concentration is expected to result in a high selectivity, given that there is a sharp drop in dopant concentration at the SiO_x interface.

Looking at the dopant concentration inside the c-Si, it can be seen that the extent of dopant in-diffusion is determined by the post-annealing thermal diffusion budget. For 1000^oC post-annealing, a drastic amount of dopant diffusion into the c-Si is measured, resulting in a decrease in iV_{oc} of 30 mV and an increase in J_0 of over 90 fA/cm^2. Comparing the samples subjected to 875/30 and 900/15 post-annealing, which have similar thermal diffusion budgets, a slight increase in excessive dopant diffusion can be observed. For the case of 900/15 post-annealing, the iV_{oc} and the J_0 values are similar. It seems like the 900/15 post-annealing, with a thermal diffusion budget of $3{\cdot}10^{-12}$ cm^2, is showing an amount of excessive dopant diffusion which is not yet affecting the passivation quality of the contact. Comparing this observation to the results from Figure 4.8, it is expected that excessive dopant diffusion will cause passivation degradation from a thermal diffusion budget of $6{\cdot}10^{-12}$ cm^{-2}.

Figure 4.11b shows the corresponding effective lifetime curves, which show the passivation difference between the samples that are investigated with ECV measurements shown in Figure 4.11a. The samples with 875/30 and 900/15 post-annealing show overlapping effective lifetime curves, which can be explained by the similar thermal diffusion budget of the annealing treatments. The effective lifetime is much lower for the 1000/1 post-annealing condition, which is directly related to the high concentration of diffused dopants in the c-Si surface region. This diffusion causes many defects in the c-Si and SiO_x interface and reduces the field-effect passivation of the poly-Si contact. Finally, the sample with 850/30 post-annealing shows a slight decrease in passivation quality. As mentioned, the active dopant concentration inside the poly-Si is almost twice as low as for the other post-annealing conditions, which could result in a lesser field-effect passivation of the interface.

Boron diffusion as a limit for p-type poly-Si contacts

It can be concluded that the overall dopant diffusion of boron into the c-Si is higher than that of phosphorus in the n-type contacts. It is already known that the diffusion coefficient of boron in c-Si is two orders of magnitude higher than that of phosphorus [27] which explains the extent to which boron atoms have diffused before they were activated. The desired doping profile in the p-type contacts is desired to be uniform in the poly-Si, while showing a strong decrease at the SiO_x interface. This could be achieved in the future by increasing the SiO_x thickness, increasing the diffusion barrier for boron to reach the c-Si. However, this will also affect the carrier transport through the interface. A thicker oxide could be more dependent on the presence of pinholes for effective carrier transport, since the tunnelling probability will be lower.

An explanation of the excessive in-diffusion could also be the duration of the post-annealing conditions, since the ramp-up time to the peak temperature takes up a large part of the total process. A solution could be to implement rapid-thermal-annealing, which minimizes the process time, but still employs the desired high-temperature annealing. The excessive in-diffusion of boron is now determining the passivation quality, so it is more challenging to assess the true influence of pinholes on the passivation quality. Reducing this in-diffusion will improve the overall passivation quality of p-type contacts and create the possibility to reassess the impact of pre-annealing on the passivation quality of p-type passivating contacts.

4.5. Summary

Passivation in ion-implanted poly-Si contacts was investigated in this section. It was attempted to study the influence of two separate annealing conditions on the passivation quality of textured poly-Si. Pre-annealing before dopant introduction was performed to create pinholes in the SiO_x and changes the post-annealing conditions were made to analyse the passivation quality. All post-annealing conditions were compared by the concept of thermal diffusion budget that quantifies the degree of diffusion of dopant atoms into the c-Si at the contact interface.

N-type contacts implanted with phosphorus have shown an increased passivation when applying pre-annealing. However, 1075^{o}C pre-annealing results in passivation degradation, caused by excessive dopant diffusion into the c-Si. A high pinhole density contributes to this, since many diffusion paths decreases the diffusion barrier properties of the SiO_x. The passivation also degraded for a combination of pre-annealing with 1000^{o}C post-annealing, which can also be attributed to excessive dopant diffusion into the c-Si bulk.

The optimal process window for n-type contacts is large, showing an iV_{oc}>720 mV and J_0<10 fA/cm^2 for using 1000-1025^{o}C pre-annealing and 850-950^{o}C post-annealing. The best passivation was achieved by 1000^{o}C pre-annealing and 875/15 post-annealing, resulting in iV_{oc} = 729.8 mV and J_0 = 5.3 fA/cm^2. The effective lifetime curves show that contacts without pinholes in the SiO_x show different dominant recombination mechanisms at lower excess carrier densities than contacts with pinhole in the SiO_x. Auger recombination is dominant in the contacts with pinholes, where SRH recombination plays a bigger role in the contacts without pinholes. ECV measurements confirm the excessive doping into the c-Si bulk for 1075^{o}C pre-annealing and 1000/1 post-annealing, where the 1025^{o}C pre-annealing does not result in extra dopant diffusion, compared to the SiO_x without pinholes.
The passivation difference between the samples with and without pinholes can be explained by pinhole-enhanced passivation. Local in-diffusion of phosphorus creates an addition to the internal field, which attracts majority carriers and repels minority carriers from the pinhole sites. As long as the pre-annealing treatment does not affect the chemical passivation quality of the SiO_x or its related recombination does not dominate the c-Si/SiO_x/poly-Si interface recombination, this mechanism can positively affect the passivation quality of the n^+-poly-Si contact.

P-type contacts implanted with boron have shown an increased passivation as well when applying a pre-annealing step before implantation. Compared to the n-type contacts, the benefit of pre-annealing seems to be much less for the p-type contacts. On the contrary, 1075^{o}C pre-annealing results in lesser passivation degradation for the n-type contacts. The passivation quality seems to be more dependent on the post-annealing thermal diffusion budget than the pinhole density. This indicates that the barrier effect of the SiO_x is significantly lower for boron than for phosphorus. Nevertheless, the presence of pinholes has shown to improve the passivation of the contact.

The optimal process window for p-type contacts is narrow, since only 875/30 post-annealing, combined with pre-annealing, and a few specific combinations of annealing conditions result in a high passivation quality. The best passivation was achieved for for the sample subjected to 1025^{o}C pre-annealing and 875/30 post-annealing, resulting in iV_{oc} = 689.1 mV and J_0 = 37.3 fA/cm^2. The passivation of all p-type contacts seems to be limited by SRH recombination, going from the shape of the effective lifetime curves. This indicates a high interface trap state density for p-type contacts at the SiO_x interface, which is expected to be caused by boron atoms. No difference in the shape of the effective lifetime curves can be observed between contacts with and without pinholes, which implies that there the dominant recombination mechanisms in the contacts are similar.

ECV measurements confirm this, since there is excessive boron diffusion into the c-Si for each post-annealing condition. The presence and density of pinholes in the SiO_x have shown to have no impact on this diffusion, which shows the porosity of the SiO_x towards the boron. On the other hand, the dopant diffusion is strongly dependent on the post-annealing thermal diffusion budget, which was observed by ECV measurements. Degradation of the contacts by excessive boron diffusion is estimated to happen around a thermal diffusion budget above $6{\cdot}10^{-12}$ cm^2. To improve the passivation of the p-type contacts from this study, the excessive in-diffusion of boron should be minimized, which could be done by introducing a thicker oxide or use an RTP process for post-annealing. Combining this with a state-of-the-art hydrogenation procedure should result in an iV_{oc} above 700 mV.

5

Extraction of metal-induced recombination in poly-Si based passivating contacts

To be able to understand the origin and mechanism behind metal-induced recombination ($J_{0,metal}$), a method to extract this parameter has been conceptualised. A simple approach to retrieve the metal-induced recombination after contact formation could be an opportunity to extensively investigate factors that impact the recombination during or after metallization. This part of the thesis project was focused on the method, while trying several contact configurations to try to observe differences between them. The contact annealing time is also investigated, for monitoring the evolution of the recombination.

5.1. Existing measurement methods

The quality of a contact in a solar cell is expressed in two parameters: the recombination current density (J_0) and the contact resistivity (ρ_c). To achieve a Fill Factor (FF) and open-circuit voltage (V_{oc}) that are as high as possible, both of these parameters should be minimized [14]. Usually this comes to a tradeoff between the relative influence of J_0 and ρ_c. In a way, J_0 and ρ_c are related since they are both dependent on the conductivity of charge carriers in the contact (σ_n for electrons and σ_p for holes). Initially, J_0 is defined by the chemical passivation (defect passivation) of the interface(s), but it also depends on the conductivity of minority carriers.
Melskens et al. have performed simulations on the relative impact of J_0 and ρ_c on the cell efficiency, neglecting other losses on the front side of the cell. They found that below a ρ_c value of ~100mΩcm^2, no significant improvement in solar cell efficiency should be expected when further reducing ρ_c. Therefore it is critical to further reduce J_0, rather than reducing ρ_c.

The area with the most potential for J_0 improvement is the metal-induced recombination after metallization, which causes a significant increase in the total recombination current density. The surface recombination at non-metallized areas in state-of-the-art poly-Si based passivating contacts are reaching values below 1 fA/cm^2 [68], where the local metal-induced recombination is still estimated to be around 100-2500 fA/cm^2 [34, 69]. So this metallization is becoming more and more important to improve the solar cell efficiency.
The metal-induced recombination current density is commonly expressed as $J_{0,metal}$ or $J_{0,m}$, describing the total recombination current density between the metal and semiconductor. There exist several ways to extract this $J_{0,metal}$, of which all are indirect methods. Two examples of the most used methods are photo-luminescence (PL) imaging [70] and the I-V method [71, 72]. Photo-luminescence imaging and the I-V method both perform measurements on cell structures with varying metal contact fractions (F_{met}).
The PL method requires measurements on a special test pattern [73, 74], which consists of mini solar cells with a varying metal fraction, by changing the metal line widths or the finger spacing. The luminescence of the cells are imaged while simultaneously measuring the V_{oc} at 1 sun illumination. This

Table 5.1: Previous results from metal-induced recombination measurements on diffused emitters and poly-Si on oxide contacts. The metallization procedure for all results was screen-printing (combined with a fire-through process), but the metal pastes that were used are different for all experiments.

	Author	Year	Contact type	Contact technology	$J_{0,m}$ (fA/cm^2)	Extraction Method
Emitter technology	Comparotto et al. [70]	2018	n-type	emitter	600-1300	PL method
			p-type	emitter	400-600	PL method
	Inns [72]	2016	n-type	emitter	400-4000	IV method
	Shanmugam et al. [73]	2015	n-type	emitter	800-900	PL method
	Fellmeth et al. [71]	2011	n-type	emitter	550-2700	IV method
	Mihailetchi et al. [76]	2018	n-type	emitter	500-1900	PL method
			p-type	emitter	600-4000	PL method
	Padhamnath et al. [77]	2019	n-type	emitter	700-800	PL method
poly-Si on oxide	Padhamnath et al. [77]	2019	n-type	200 nm poly-Si	35	PL method
	Stodolny et al. [67]	2017	n-type	200 nm poly-Si	100-200	IV method
	Ciftpinar et al. [75]	2017	n-type	100 nm poly-Si	1084+/- 461	PL method
			p-type	100 nm poly-Si	796 ± 103	PL method
			n-type	200 nm poly-Si	386 ± 22	PL method
			p-type	200 nm poly-Si	319 ± 40	PL method
	Chaudhary et al. [78]	2019	n-type	200 nm poly-Si	70-890	PL method
	Chaudhary et al. [79]	2021	n-type	150 nm poly-Si	70	PL method

will reveal changes in recombination for the areas with different metal fraction.
In the I-V method, $J_{0,metal}$ can be extracted from observing changes in the total recombination for different metal fractions. Suns-V_{oc} measurements will determine V_{oc} and J_{sc}, which can be used to calculate $J_{0,total}$ of each cell. A linear fit through the recombination current density at different metal fractions will reveal $J_{0,metal}$.
The downside of the IV or PL method is that it requires a finished solar cell, which makes it difficult to investigate one type of contact. It also requires metallization on both sides, which could induce a large amount of recombination in the cell, when it is desired to see the differences between several percentages of metal fraction.

Previous research into the metal-recombination in solar cells has resulted in a wide range of $J_{0,metal}$ for several types of contacts. Some ten years ago, the metal-induced recombination was first investigated in PERC solar cells, where the emitter was investigated. Later on, also poly-Si passivating contacts were investigated. An overview of some experimental results is shown in Table 5.1. All studies have investigated screen-printed metals, while the contact technology and type were different. The metal-induced recombination shows a wide range, from 70 to 1500 fA/cm^2. The results from Ciftpinar et al. [75] show a slightly higher $J_{0,metal}$ for n-type contacts than for p-type poly-Si passivating contacts, which could mean that the n-type layer is more sensitive to interactions with the metal. They also found that $J_{0,metal}$ is lower when the poly-Si layer is thicker. Mihailetchi et al. have found a slightly higher metal-induced recombination in n-type contacts for textured surfaces when compared to flat surfaces [76]. For p-type contacts, $J_{0,metal}$ almost doubled on a textured surface compared to a flat surface.

5.2. Experimental Method in this work

Despite the existence of methods to extract $J_{0,metal}$, it was attempted in this experimental section to use a new, more straightforward, method to achieve the same goal. Instead of fabricating solar cells with both polarities and double side metallization, a more lean process flow and straight on interpretation of measurements was investigated.
Just as for the PL method and IV method, $J_{0,metal}$ should be extracted by varying the metal fraction on the surface. In this way, the areal influence of the metal on the total recombination current density ($J_{0,total}$) can be monitored. Since $J_{0,total}$ can be determined quite accurately with photo-conductance lifetime measurements, this is an opportunity to investigate any metal-induced recombination at the c-Si/SiO_x/poly-Si interface.
Before metallization, the sample structure consists of poly-Si based passivating contacts in a symmetrical structure. Since both sides of the wafer are identical, their passivation is assumed to be identical as well. This assumption will be used to define the recombination at the passivated areas ($J_{0,passiv}$).
As described by Feldmann et al. [59], the total recombination current density of a metallized surface

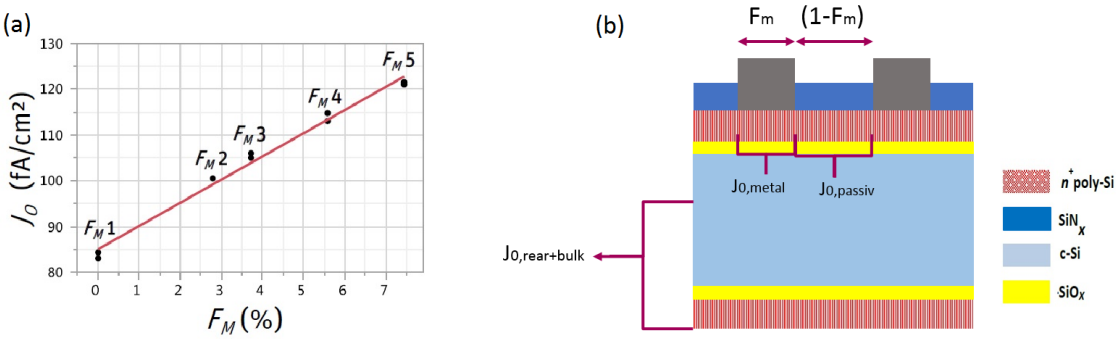

Figure 5.1: Experimental approach to (a) measure the recombination current density ($J_{0,total}$) for varying metal fraction [70], by (b) considering the total recombination as a combination of bulk+rear, passivated front and metallized front.

can be divided into areal sections. The recombination at the non-metallized surface will be defined as $J_{0,passiv}$, which is a passivated surface. The recombination at the metallized area is defined as $J_{0,metal}$, which contributes to the total recombination by the areal fraction of the metallization. This results in equations 5.1, which concludes to a linear relation between the metal fraction (F_m) and the total recombination current density ($J_{0,total}$).

$$J_{0,total} = J_{0,bulk+rear} + (1 - F_m) * J_{0,passiv} + F_m * J_{0,metal} \tag{5.1a}$$

$$J_{0,total} = (J_{0,bulk+rear} + J_{0,passiv}) + F_m * (J_{0,metal} - J_{0,passiv}) \tag{5.1b}$$

Here, $J_{0,total}$ is the sum of the rear, bulk and front recombination, where the front recombination is divided into the metallized and non-metallized areas. Compared to the surface recombination, bulk recombination is assumed negligible, so $J_{0,rear+bulk}$ will become $J_{0,rear}$. The advantage of symmetrical contact structures will now be that $J_{0,passiv,front} = J_{0,passiv,rear}$, which makes equation 5.1 only consist of four variables, of which three can be determined. A representation of the method is shown in Figures 5.1a [70] and 5.1b, where the different components of $J_{0,total}$ are addressed.

$J_{0,total}$ will be measured for each metallized area with photo-conductance lifetime measurements in the experimental part of the $J_{0,metal}$ extraction. To determine $J_{0,passiv}$, the passivation of the symmetrical contacts is monitored during contact fabrication. After hydrogenation, the final passivation quality is determined by photo-conductance lifetime measurements, from which $J_{0,total}$ is obtained. The assumption is now that $J_{0,total} = 2 \cdot J_{0,passiv}$.

However, to make these assumptions, it is required to show a sufficient uniformity of the surface passivation across the whole wafer. Only then it can be assumed that the passivation quality is similar on every position of the wafer. In the metallization structure, the metal fractions are chosen to be 0%, 5.17%, 9.33% and 17%. One area will have 0% of metal, because passivation degradation of the passivated area can then be monitored. The mask design that was used to obtain the test structure is shown in Figure 5.2. This mask divides the wafer into four quarters, which area will be sufficiently large to perform independent lifetime measurement, while keeping the wafer intact.
The determination of $J_{0,metal}$ was eventually done by creating a linear fit through four data points that represent $J_{0,total}$ of the four areas of the wafer, of which an example is shown in Figure 5.1a. This linear curve is assumed to represent the relation between $J_{0,total}$ and F_m as described in equation 5.1. The slope of the curve will then result in $J_{0,metal} - J_{0,passiv}$, of which $J_{0,passiv}$ was already determined earlier.

To investigate this metal-induced recombination, the samples are subjected to contact annealing, which is done to initiate degrading effects of the metal. Temperature and time will be varied during the experiment, where the temperature range will be 400^{o}C to 550^{o}C. It will be attempted to observe the evolution of the metal-induced recombination during this contact annealing, by interrupting the contact annealing for every few minutes and performing the lifetime measurements. Eventually, the metal will be stripped from the samples to observe the actual damage that the metal has done to the poly-Si(O_x), SiO_x and/or c-Si.

5.3. Sample preparation

The sample preparation in this experiment was not based on a single flowchart. Due to problems with consistent passivation quality and layer deposition in one of the processing steps, the sample preparation steps needed to be adapted several times during the experiment. This resulted in three different types of contact structures for the measurement of $J_{0,metal}$. This experimental section was primarily based on testing the measurement method, rather than characterising the $J_{0,metal}$ parameter of the specific contacts. It was thus not relevant for the sake of the experiment to make identical contact structures or use identical process flows.
The experiment was aimed at making symmetrical contact structures, similar to that in Chapter 'Ion implanted LPCVD poly-Si passivating contacts'. N-type contacts were chosen, since these resulted in the most consistent depositions and passivation quality. Both flat and textured surfaces are tested, so the textured wafers will require several extra processing steps. Since implantation was not possible anymore in the EKL, doping of the poly-Si layer is now done by depositing in-situ doped PECVD a-Si:H to replace this implantation step. This a-Si:H has not been optimized a lot in the used deposition setup, so oxygen-alloyed amorphous silicon (a-SiO_x:H) layers were also used to create a working contact structure. The following subsections will address the processing steps in fabrication the different contacts structures.

Textured LP- + PECVD poly-Si contacts

Figure 5.3 shows the processing steps involved in fabricating the contacts, where cleaning steps are left out. The samples were based on flat (100) n-type FZ wafers, which were subjected to a texturing process. As described in 'Fabrication', TMAH is used to create pyramidal features on the surface with a (111) orientation. To smoothen the sharp features, the wafers are submerged in a Si etching solution. Before entering this solution, the wafers need Standard Cleaning. Before the oxide growth, the surface needs to be ultra clean, which is done by the Standard Cleaning process, followed by and HF (0.55%) and Marangoni drying.
The tunnelling oxide is grown by thermal oxidation, as is described in 'Fabrication'. This resulted in a SiO_x layer of approximately 1.36 nm. This oxidation step was immediately followed by a 20 nm a-Si:H deposition by LPCVD. The LPCVD process was performed at 580^oC, which resulted in a deposition rate of 2.21 nm/s on a flat surface. Based on Chapter 'Ion implanted LPCVD poly-Si passivating contacts', a 20 nm layer required 11.33 minutes of deposition time.

After a-Si:H deposition, a pre-annealing step of 1025^oC was performed, to create pinholes in the SiO_x. When planning this experiment, the goal was also to characterise the metal-induced recombination, so

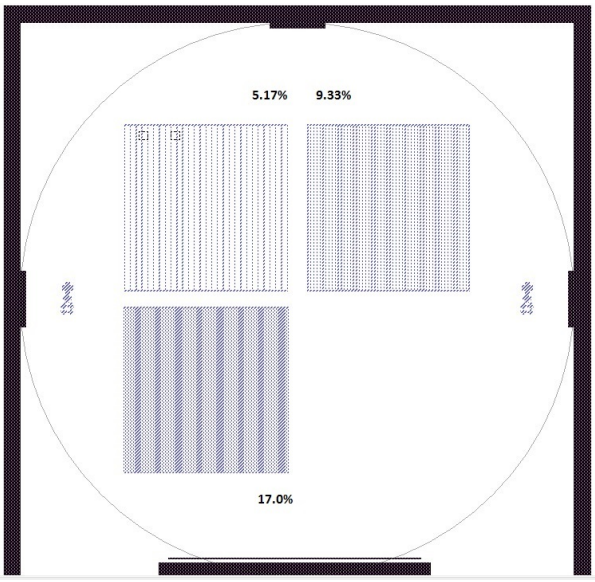

Figure 5.2: Lithography mask used to obtain the test structures with varying metal fraction.

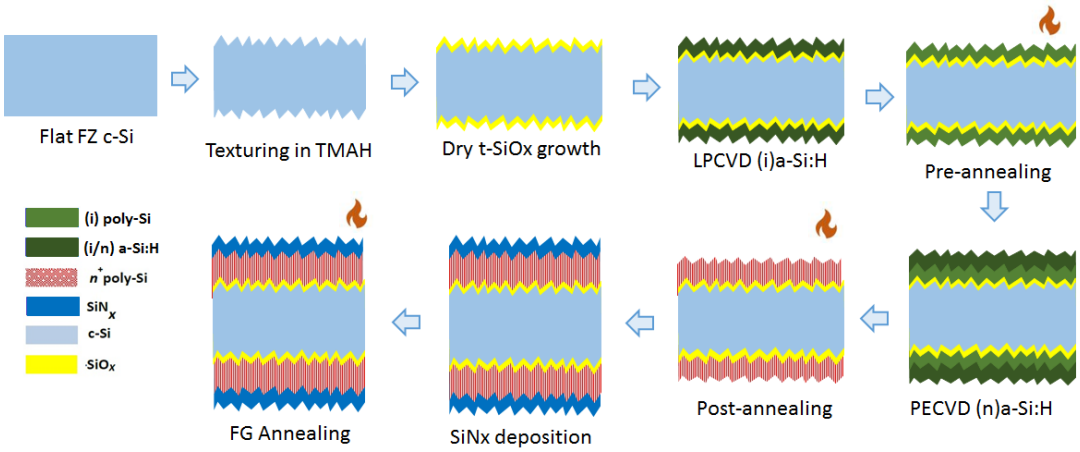

Figure 5.3: Processing steps involved in the samples preparation of poly-Si contacts with thermal oxide and LP- + PECVD poly-Si stack.

the impact of pinholes was included. However, this part was not addressed anymore later on. After the pre-annealing step, it is assumed that a thin oxide layer has formed on the surface, so this is removed by an HF dip (0.55%) and IPA drying (Marangoni). Immediately after this cleaning step, a P-doped (n^+)a-Si:H layer was deposited on both sides of the wafer in the AMOR deposition setup. The vacuum was not broken in this process.

To activate the dopants and crystallize the (i-n^+)a-Si:H, the samples were subjected to a post-annealing process with a peak temperature of 900^{o}C, which was maintained for 15 minutes (900/15). This specific condition was chosen, based on a test before executing this experiment, where the 900/15 condition resulted in decent passivation ($iV_{oc} \approx 700$ mV and $J_0 \approx 20$ fA/cm^2). For all samples the passivation was measured after post-annealing by photo-conductance decay lifetime measurements to monitor the quality, but also the uniformity of the passivation. Hydrogenation was done by deposition of a SiN$_x$:H layer by PECVD and providing a Forming gas annealing (FGA) treatment to passivate the dangling bonds and thus reducing the defect density at the interfaces in the contact. The conditions for the SiN$_x$:H deposition and FGA are fixed, as described in 'Fabrication'. After hydrogenation the passivation was measured again to check the quality and uniformity.

Flat and textured poly-SiO$_x$ contacts

The samples were based on flat, n-type FZ (100) oriented wafers, where some were textured and the others have been left flat. As mentioned, the texturing of the wafers added several steps to the process flowchart. The texturing was done with TMAH, as described in 'Fabrication' (Chapter 2). This was followed by Standard Cleaning and a Si etch to round the pyramidal structures on the surface. To make the surface ultra clean and remove any 'native' oxide from it, a Standard Cleaning step was done, followed by an HF dip (0.55%) and IPA drying (Marangoni).
For these contacts, a different oxidation step was used, because an already existing flowchart was followed to obtain working contacts. The oxidation was done by Nitric Acid Oxidation of Silicon (NAOS), which is described in 'Fabrication' (Chapter 2). Here the nitric acid forms a uniform oxide with a fixed thickness (~1.4 nm, [30]). Immediately after, a stack of two a-Si:H layers is grown by PECVD in the AMOR deposition setup. First, an intrinsic layer of a-SiO$_x$:H is deposited with an expected thickness of 10 nm. On top, a 20 nm thick layer of P doped a-SiO$_x$:H is deposited to supply the dopants needed in the contact. Both sides of the wafer are deposited without breaking the vacuum of the deposition chamber.

To crystallize and merge the two layers, a post-annealing treatment with a peak temperature of 850^{o}C for 30 minutes was performed. The thermal budget of this process is quite low, but research in the PVMD group has shown that thinner poly-Si based contacts are more sensitive to these high temperature processes like post-annealing. After this post-annealing, the passivation was measured by photo-conductance decay lifetime measurements to monitor the quality and uniformity. Hydrogenation was done by deposition of a 80 nm SiN$_x$:H layer by PECVD, which provided the hydrogen for passivating

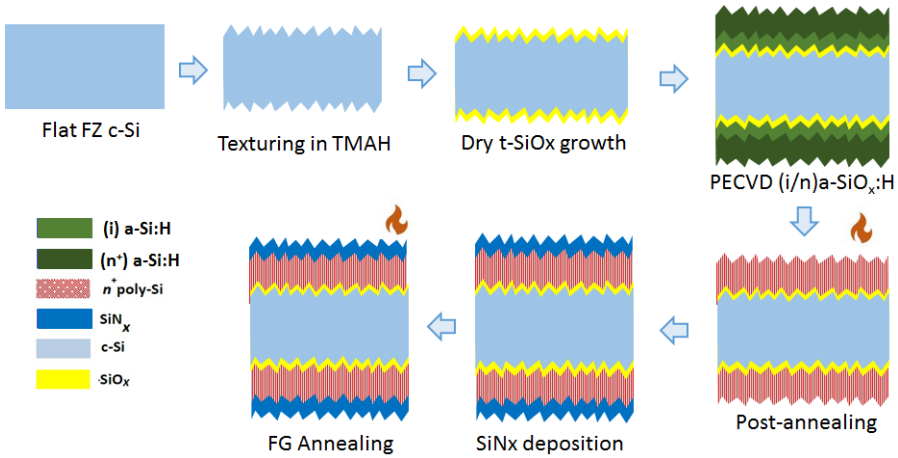

Figure 5.4: Processing steps involved in the samples preparation of poly-Si contacts with NAOS oxide and (i/n) PECVD poly-SiO_x stack. The deposition and annealing steps were identical for flat and textured samples.

dangling bonds. Subsequently, Forming gas annealing provided even more hydrogen and drive the hydrogen into the contact from the SiN_x:H layer. The passivation was measured again after finalizing the contact structures. The processing steps are shown in Figure 5.4, where the cleaning steps are not mentioned.

Metallization

To extract the metal-induced recombination, areas with varying metal fraction are created on the samples. To be able to compare the recombination current density at those sites, it is crucial to have a uniform passivation quality in the whole wafer. That is the reason for monitoring the passivation quality and uniformity throughout the experiment. It should be noted that the metallization procedure is identical for all types of samples.

To get the different metal fractions, photo-lithography was used to pattern the surface. Precise alignment was not necessary, since the features in the finger structure are in the range of 0.1-1 mm. The coating of the front side was done with positive photo-resist, which dissolves in developer solution after it is exposed with UV light. The thickness of the coating was kept constant at 4 μm. The samples were aligned manually and exposed for 40 seconds. The exposed finger areas are dissolved in the solution, leaving opened areas to deposit the metal fingers. The mask that is used for the exposure is shown in Figure 5.2, where the metal fraction of the four quarters is shown to be 0%, 5.17%, 9.33% and 17.0%.

To create a contact junction, the SiN_x layer on top of the poly-Si needs to be removed at the exposed area before metal deposition. However, prevent changing too much on the sample structure, the back side is also protected by photo-resist. In this way, the SiN_x is protected from etching. This is done by etching the samples in BHF 1:7, which etches only the SiN_x, but not the poly-Si. The etch time was chosen to be 10 minutes, which was determined with a test sample. This resulted in a slight under-etch of the fingers, but considering the size of the fingers, this under-etch was negligible. To keep the backside

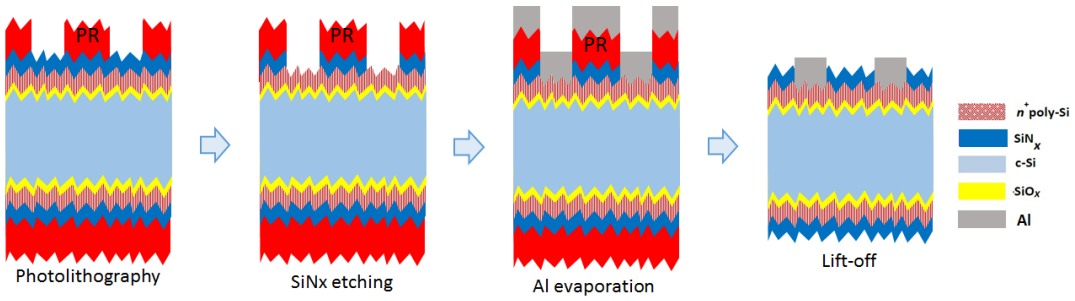

Figure 5.5: Processing steps involved in the metallization of the samples. This is the example for a textured sample with poly-Si contacts, where PR indicates photo-resist.

intact, the backside of the samples were also covered with photo-resist to prevent SiN_x etching of the backside. Aluminum was then deposited with e-beam evaporation, which is explained in 'Fabrication'. The expected thickness on a flat surface was 500 nm, which resulted in a 400 nm layer on a textured surface. In the experiment, the thickness of the Al is not expected to influence the metal-induced recombination. Te exact thickness is not relevant since this experimental section was not focused on the characterisation of the metal-induced recombination.

To remove the excess metal and the photo-resist from the not exposed area, a lift-off process is used. The photo-resist is dissolved in acetone, while enhancing this dissolution in an ultrasonic bath. Dissolving the photo-resist will result in the 'lift-off' of the Al from the sample, only leaving behind the Al on the exposed parts. This finalizes the sample fabrication. The processing sequence for the metallization in this experimental section is shown in Figure 5.5, which shows a example of the process steps for a textured sample.

Contact annealing and metal removal

To form the metal-semiconductor junction, the samples are subjected to contact-annealing. Contact annealing involves heating the finalized samples to temperatures above 400^oC in ambient air on a hot plate. Annealing times and temperatures vary, but the experiment was designed to perform accumulative annealing, while monitoring the passivation quality of all four quarters in between the annealing steps.

Eventually the metal is removed afterwards and the passivation is measured again, which will show the effect of the metal on the passivation quality of the c-Si/SiO_x/poly-Si interface. Al can be dissolved in PES 77-19-04, of which the composition is a combination of H_3PO_4, HNO_3 and CH_3COOH dissolved in H_2O. The etch time was determined to be 8 minutes by tests.

5.4. Metal-induced recombination in poly-Si based contacts

This section is focused on presenting the findings from the experimental methods described previously. First the uniformity of the passivation quality will be discussed, after which the results from accumulative contact annealing will be explained. The aim of this experiment was to try out an easy and relatively fast method to extract metal-induced recombination, in order to optimize the passivation quality of the poly-Si based contacts in the future.

Uniformity of the passivation quality

Not for all samples it was possible to achieve acceptable uniformity in terms of $J_{0,total}$. Since this is the key parameter, the analysis of the experiment should account for this. The non-uniformity was the highest for the samples with the LP- + PECVD stack. Table 5.2 shows the measured total recombination current density extracted from the photo-conductance decay lifetime measurements for each position on the wafer. The marked rows represent the regions of interest in the $J_{0,metal}$ extraction. It can be seen that sample A2 and A3 with thermal oxide (TO) and an LP- + PECVD stack do not show good uniformity. Nevertheless, the samples were used in the experiment. It could be useful to just look at the relative increase of $J_{0,total}$ for each quarter, which will provide a more accurate slope of the $J_{0,total}$ vs. F_m curve. However, areas with lesser passivation quality could possibly degrade faster, which will affect the measurement. The regions of interest, which will be metallized, are marked in Table 5.2 in green, which represent the four quarters that will be investigated by accumulative annealing. The passivation of the poly-SiO_x contacts on a flat surface show to be better than textured, which is related to a lower defect density at the c-Si/SiO_x/poly-SiO_x interface for a flat surface.

Table 5.2: Uniformity of the passivation expressed in $J_{0,total}$. All values listed are in the unit of fA/cm^2. The abbreviations that indicate the position mean the following: t = top, b = bottom, l = left, r = right, c = center.

$J_{0,total}$ (fA/cm^2)	TO & i-n LP- + PECVD stack			NAOS & i-n PECVD stack			
Position	**A1**	**A2**	**A3**	**B1**	**B2**	**C1**	**C2**
tl (5.17%)	14.0	13.4	30.4	14.5	18.0	13.1	6.6
t	18.1	16.4	37.5	19.2	20.6	10.3	8.3
tr (9.33%)	17.1	21.4	61.3	13.6	18.5	9.7	6.9
l	16.6	15.8	35.4	12.7	12.8	11.1	7.0
bl (17.0%)	17.5	23.7	41.7	13.5	12.2	11.3	7.0
r	19.7	31.1	83.8	13.2	12.5	12.1	7.1
br (0.00%)	24.0	42.2	83.2	13.3	12.8	8.3	7.3
b	22.2	30.8	52.6	17.4	14.5	8.4	7.6
c	21.7	22.8	53.9	22.5	21.6	8.3	9.2
	Textured					**Flat**	

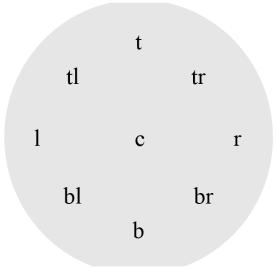

Textured thermal oxide/LP- + PECVD poly-Si contact stack

Figure 5.6a-c shows the results for each sample with this particular contact stack. The blue bars indicate that the uniformity before metallization is not acceptable for samples A2 and A3, while the uniformity of A1 is somewhat acceptable. The passivation measurements after metallization show counter-intuitive results. The passivation quality seems to increase when metal is deposited, resulting in an increasingly lower $J_{0,total}$ for increasing F_m. To understand this, the measurement method should be considered. The lifetime measurement with a Sinton WCT-120 measures the photo-conductance inside the c-Si. Now the recombination at the c-Si/SiO_x/poly-Si interface is the area of which the passivation can be measured, considering that the bulk recombination is negligible. Directly after metallization, the Al is not in contact with the c-Si surface, so it cannot induce recombination there. Two options are possible, the presence of Al has a positive effect on the recombination at the interface, or the metal is influencing the measurement and the results do not represent the actual passivation quality of the contact. The latter is most likely the case, as Al is a highly conductive material that could impact the free charge carriers at the interface.

In sample A1, $J_{0,total}$ shows an increase of 8.1 fA/cm^2, which is considered significant when looking at the relative increase. It could be a sign of damage to the contact quality, but uncertainty in fitting

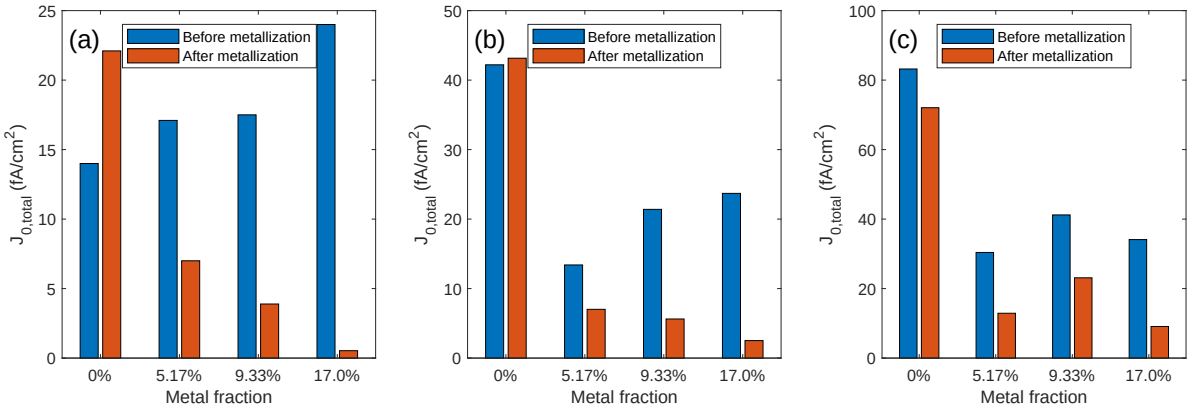

Figure 5.6: Passivation of the investigated areas on the samples (a) A1, (b) A2 and (c) A3 with TO & LP- + PECVD contact structure.

$J_{0,total}$ also plays a big role. For a passivated surface the slope that determines J_0 can be extracted quite easily, but when it is more challenging when this slope is not constant.

Despite several uncertainties in the experiment, it was continued anyhow, due to the limited passivation quality of the available process recipes that was achieved in the project timeline. Accumulative annealing is expected to drive the recombination to higher values, which could at one point dominate the recombination at the contact, showing an increased recombination current density for increasing metal fraction.
To test the impact of the contact annealing on the recombination current density measured by lifetime measurements, sample A1 was first annealed for 10 minutes set at 400^oC with steps of one or two minutes. After these 10 minutes, still no change was visible regarding J_0 of the four areas. It was attempted to induce recombination by increasing the temperature setting to 500^oC and increasing the time step to 5 minutes. Afterwards, the Al was removed, where the passivation quality was measured again. The evolution of $J_{0,total}$ for each (non-)metallized area in sample A1 is shown in Figure 5.7.
The 400^oC setting shows to have no impact on the passivation quality according to the lifetime measurements, but $J_{0,total}$ shows a decrease for the metallized areas. When applying a higher temperature

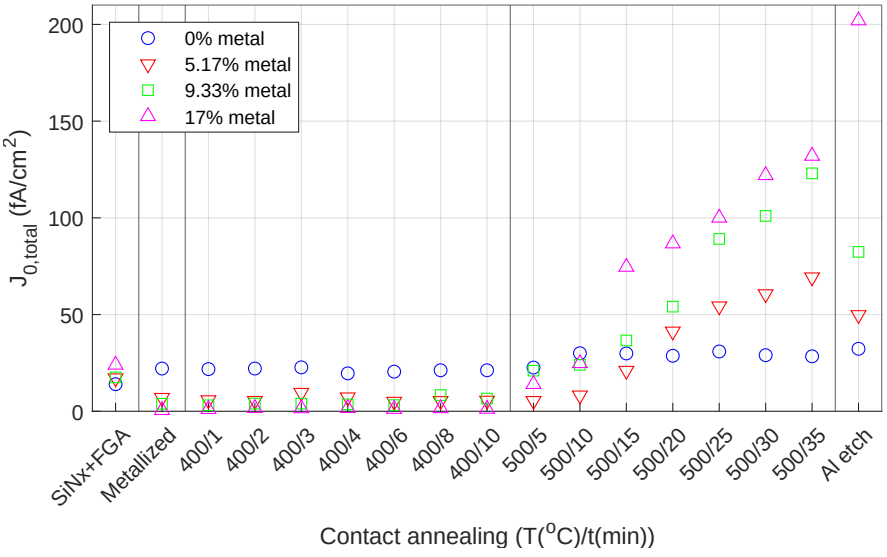

Figure 5.7: $J_{0,total}$ evolution of sample A1 during accumulative contact annealing. The $J_{0,total}$ values before metallization, after metallization and after metal removal are added for comparison.

setting, the metal-induced recombination starts to become dominant over the influence of Al on the measurement. However, this is only after 10 minutes at 400^{o}C and additionally 20 minutes at 500^{o}C. The 0% area also shows a slight increase in $J_{0,total}$ pointing towards passivation degradation of the contact when too much thermal energy is supplied. This could be attributed to effusion of hydrogen, which is a process that occurs at elevated temperatures (≥400^{o}C) [28]. When the Al is removed, $J_{0,total}$ changes again at all metallized areas. Now, the expected increase of $J_{0,total}$ for increasing metal fraction can be visible, pointing toward the fact that this final measurement is believed to be the most accurate estimation of the metal-induced recombination in the contact.

The same analysis of the contact passivation has been performed for samples A2 and A3, but with a different accumulative annealing sequences. Figure C.1 in Appendix C shows a similar passivation evolution for sample A2, when compared to sample A1. For this sample, the area with no metallization has shown no passivation degradation over the course of many contact annealing steps. During the accumulative contact annealing, a significant increase in $J_{0,total}$ could not be observed for the metallized areas. However, when the metal was removed, a clear relation between F_m and $J_{0,total}$ could be observed.
Similar observations can be made for sample A3, where the metal-induced recombination became clear after metal removal (Figure C.2, Appendix C). For sample A3, $J_{0,total}$ is much higher than in the other quarters, so the average $J_{0,total}$ of the three metallized areas before metallization is taken as the $J_{0,total}$ with 0% metal.

The derivation of the metal-induced recombination ($J_{0,metal}$) was based on equation 5.1. Accounting for the non-uniformity of the surface passivation (as shown in Table 5.2), relative increase of $J_{0,total}$ is considered for the $J_{0,total}$-F_m data fitting. Since the metal-induced recombination was already measurable for sample A1 during contact annealing, an analysis was made by calculating $J_{0,metal}$. Figure 5.8 shows the relative increase in $J_{0,total}$ for each quarter, compared to the passivation quality after hydrogenation. A linear fit through the data points shows the estimation of the linear relation as defined in equation 5.1. Figure 5.8 provides a representation of the approach that was used to estimate the metal-induced recombination.
The calculated values of $J_{0,metal}$ are listed in the legend, which show an increasing $J_{0,metal}$ for increasing annealing time. A large difference can be seen when the Al is removed, where $J_{0,metal}$ jumps from 593.2 ± 160.8 fA/cm^2 to 968.6 ± 170.1 fA/cm^2. The calculation of $J_{0,metal}$ is less straightforward that in equation 5.1, since $\Delta J_{0,total}$ is considered now. A derivation of the uncertainty boundaries can be found in Appendix C.

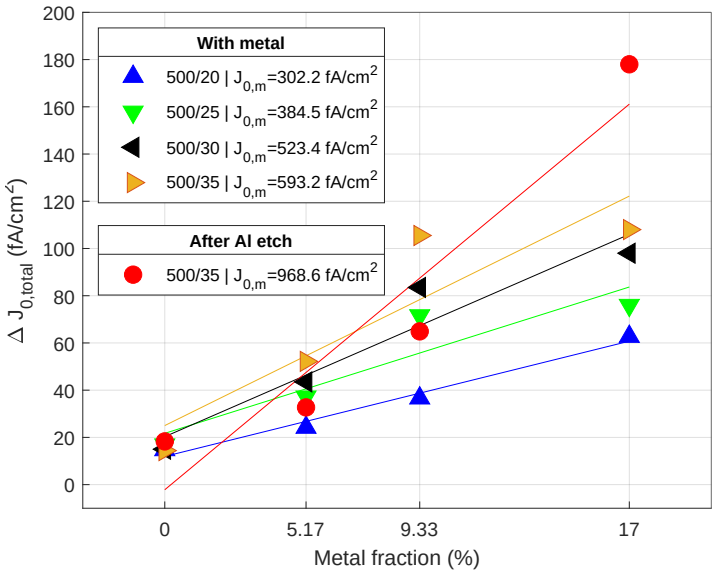

Figure 5.8: Linear fitting of the metal-induced recombination during contact annealing in sample A1 with TO & LP- + PECVD poly-Si contacts. $J_{0,m}$ after Al removal is also shown. The solid lines represent the linear fit through the experimental data.

To get the right slope, the relative increase in $J_{0,total}$ is considered, but this changes the y-axis intersection that determines $J_{0,passiv}$. Since this value is required to calculate $J_{0,metal}$, the right estimation of this $J_{0,passiv}$ is needed. This is one of the reasons why a uniform passivation is crucial to get a truly accurate value for $J_{0,metal}$. If the passivation is uniform, this correction is not needed, and the determination of $J_{0,metal}$ will be directly with equation 5.1. For this experiment, $J_{0,total}$ at 0% metal is calculated by adding the average $J_{0,total}$ after hydrogenation to the y-axis intersection of the linear fit. This will combine the starting point of the passivation with the estimated increase in $J_{0,total}$, which is caused by contact annealing. For the passivated area, it is estimated that the front and back are the main contributors to $J_{0,total}$, so it is assumed that the bulk recombination is negligible. The samples are made symmetrical, so it is also assumed that the contribution of the front and back contact is identical. This results in the following assumptions:

$$J_{0,total}(0\%) = J_{0,front}(0\%) + J_{0,back} = 2J_{0,passiv}$$

with

$$J_{0,total}(0\%) = \Delta J_{0,total}(0\%)\Big|_{fit} + \bar{J}_{0,SiNx+FGA}$$

which concludes to

$$J_{0,metal} = \frac{d(\Delta J_{0,total})}{dF_m}\Big|_{fit} + J_{0,passiv}$$

which follows from equation 5.1. For sample A2 and A3, the values for $J_{0,metal}$ are calculated in a similar way. except that the 0% area is not taken into account for the calculation of $J_{0,passiv}$, because $J_{0,total}$ of this area deviated too much from the other areas. Here, only the metallized areas are considered in the fitting, where a fixed value (equal to the average of the metallized areas) is taken for the calculation of $J_{0,passiv}$. For sample A3, it was not possible to measure a $J_{0,metal}$ during contact annealing, so only $J_{0,metal}$ after Al removal was extracted.
Figure 5.8 provides all $J_{0,metal}$ values of sample A1 that were obtained during contact annealing, but also the ones after metal removal. The results show an increase in the measured $J_{0,metal}$ when the Al is removed. This confirms the idea that the metal is influencing the passivation measurement. The $J_{0,metal}$ fits of samples A2 and A3 can be found in Appendix C.2. These values can only be compared when the samples have undergone identical contact annealing and also displayed similar passivation quality. This is not the case, so comparing $J_{0,metal}$ values for research purposes is not possible. Nevertheless, the measurement method has shown to be able to detect metal-induced recombination in these poly-Si contacts, so characterisation of this $J_{0,metal}$ could be an option in the future.

Textured NAOS/PECVD poly-SiO$_x$ contact stack

The textured samples with NAOS oxide and an i-n PECVD poly-SiO$_x$ stack showed already a more promising uniformity of passivation quality, as can be seen in Figure 5.2. This will make the analysis

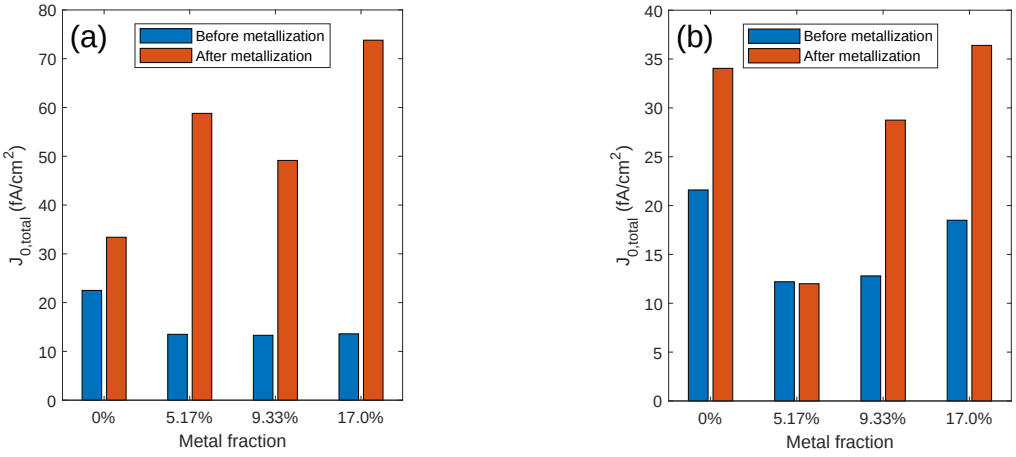

Figure 5.9: $J_{0,total}$ of the investigated areas on the samples (a) B1 and (b) B2 with NAOS & i-n PECVD poly-SiO$_x$ contact structure on a textured surface. $J_{0,total}$ before and after metallization are compared.

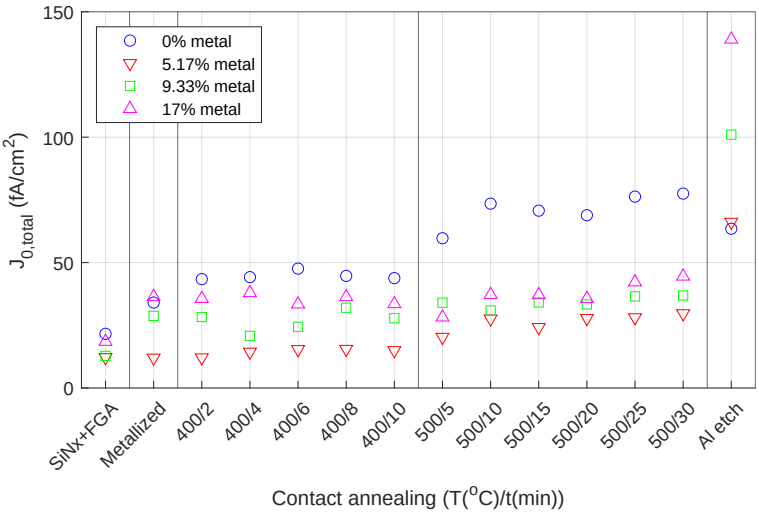

Figure 5.10: $J_{0,total}$ evolution of sample B2 during accumulative contact annealing. The $J_{0,total}$ values before metallization, after metallization and after metal removal are added for comparison.

of the passivation during contact annealing a little more straightforward, but especially more accurate. To determine the status of the contacts after metallization, the passivation of each quarter is compared before and after metallization.

Figure 5.9 displays this comparison, where it can be concluded that the metallization has degraded the passivation quality of the contacts for almost every quarter. Sample B1 (Figure 5.9a) shows a large increase in $J_{0,total}$ for all quarters, but a clear trend regarding the metal fraction could not be derived from this data. For sample B2 (Figure 5.9b) this increase of $J_{0,total}$ was less, but still significant. The quarter with 5.17% metal showed no passivation degradation, which could not be explained, considering the available data. It could be related to the poly-SiO_x layer, which is thin (~30 nm) and could thus be more sensitive to processes like Al evaporation. Nevertheless, the contact annealing experiment was executed in an attempt to observe the impact of metal on the interface with such a thin layer of poly-SiO_x.

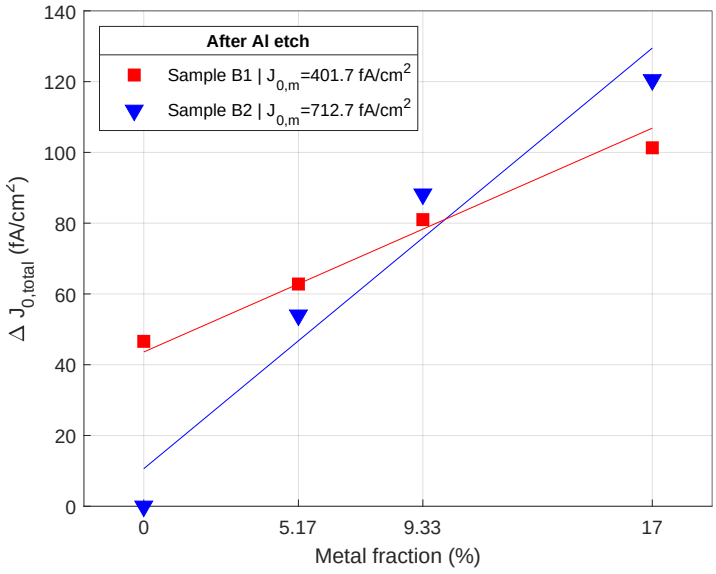

Figure 5.11: Linear fitting of the metal-induced recombination in samples B1 and B2 with NAOS & i-n PECVD poly-SiO_x contacts after Al removal. The solid lines represent the linear fit through the experimental data.

The evolution of $J_{0,total}$ in sample B2 for each quarter has been measured during contact annealing, as shown in Figure 5.10. It can be seen that the passivation quality of the area with no metal degrades fast, showing its sensitivity to the contact annealing. When the temperature setting is increased to 500^oC, $J_{0,total}$ increases even more in this area. The metallized areas show only a small increase of $J_{0,total}$ during the contact annealing, so no sign of $J_{0,metal}$ was interpreted. The small increase in $J_{0,total}$ can be attributed to the passivation loss of the non-metallized areas. However, after metal removal, the metal-induced recombination is measured, showing a steep increase of $J_{0,total}$ for the metallized areas. The non-metallized area shows a decrease after etching away the Al, which could not be explained with the available data.
The passivation evolution of sample B1 can be found in Figure C.3 (Appendix C), which shows a similar increase of $J_{0,total}$ in the non-metallized area. During contact annealing, no clear trend could be extracted from the passivation measurements on the metallized areas. Where $J_{0,total}$ is expected to increase for a higher accumulative time and temperature, $J_{0,total}$ did not show any correlation to the contact annealing time and temperature or metal fraction. Eventually, when the metal was removed, $J_{0,total}$ of the metallized areas showed and increase which resulted in the expected relation between metal fraction and $J_{0,total}$.

As mentioned, the $J_{0,metal}$ could only be observed after removing the metal. This has resulted in only two calculations of $J_{0,metal}$ for the textured NAOS & i-n PECVD poly-SiO_x contacts. Just as for the TO & LP- + PECVD poly-Si contacts, $J_{0,passiv}$ was estimated by combining the passivation measurement after hydrogenation with the y-axis crossing of the linear fit. The calculation of $J_{0,metal}$ resulted in 401.7 $\pm$ 37.3 fA/cm^2 and 712.7 $\pm$ 98.7 fA/cm^2, for sample B1 and B2 respectively. Figure 5.11 shows the linear fitting through the corrected $J_{0,total}$ values.
Sample B1 and B2 show a quite large difference in $J_{0,metal}$, but this cannot yet be explained by a single cause. Until now, there are still too many uncertainties that should be eradicated in following experiments. Contact degradation by contact annealing could also impact $J_{0,total}$ of each quarter differently, which will change the slope of the linear fit. Nevertheless, $J_{0,metal}$ was extracted from the samples, provided that the metal is removed after a certain contact annealing treatment. Going from these results, it is probably not possible to monitor $J_{0,metal}$ by accumulative contact annealing, but only for one condition.

Flat NAOS/PECVD poly-SiO_x contact stack

The purpose of investigating flat poly-Si based contacts was to check the compatibility of the measurement method, but also to see if there will be any difference between the metal-induced recombination on a flat or textured surface. Table 5.2 has shown that the uniformity of the passivation is acceptable after hydrogenation, where $J_{0,total}$ only varies several fA/cm^2 from the average $J_{0,total}$.
The effect of metallization on the passivation was again addressed by comparing the passivation mea-

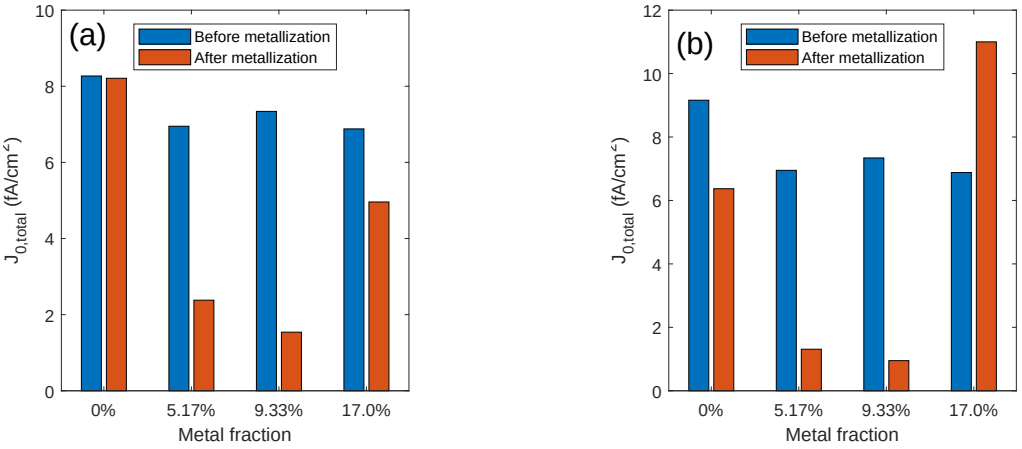

Figure 5.12: Passivation of the investigated areas on the samples (a) C1 and (b) C2 with NAOS & i-n PECVD contact structure on a flat surface.

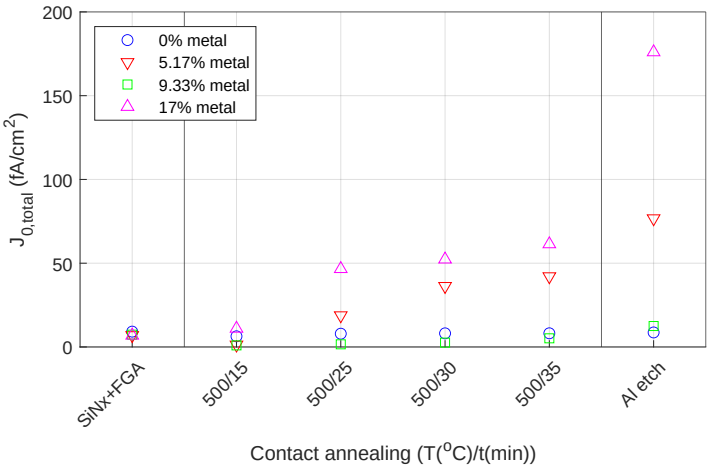

Figure 5.13: $J_{0,total}$ evolution for several contact annealing treatments to sample C2 with flat NAOS & i-n PECVD contacts. $J_{0,total}$ values after hydrogenation and after metal removal are added for comparison.

surements of each separate quarter before and after metallization. Sample C1 (Figure 5.12a) shows an almost identical $J_{0,total}$ on the non-metallized area, pointing to no negative effects of the metallization process on the passivation quality of the non-metallized areas. $J_{0,total}$ of all metallized areas have decreased, showing a similar observation as was already shown in Figure 5.6 for the TO & LP- + PECVD poly-Si contacts. Sample C2 (Figure 5.12b) showed a slight decrease in $J_{0,total}$ of the non-metallized area, which can be attributed to measurement uncertainty, since the difference is only 2.8 fA/cm^2. The areas with 5.17% and 9.33% show a similar decrease in $J_{0,total}$ as discussed before, but $J_{0,total}$ of the area with 17% metal has increased after metallization. It shows that the metal does not have a positive effect on $J_{0,total}$. One explanation could be that there is still a thin layer of SiN_x left in between the poly-SiO_x and the Al that prevents contact between the poly-SiO_x and the Al. No definite conclusions can be drawn about this with the available data.

The evolution of the passivation during contact annealing was monitored during contact annealing. Figure 5.13 shows the evolution of $J_{0,total}$ of sample C2, which was subjected to 500^{o}C for 35 minutes and a final 10 minutes at 550^{o}C. After 25 minutes of contact annealing at 500^{o}C, the first signs of metal-induced recombination become visible. However, this happens only in the areas with 5.17% and 17% metal, while $J_{0,total}$ of the area with 9.33% metal remains low. $J_{0,total}$ of the non-metallized area

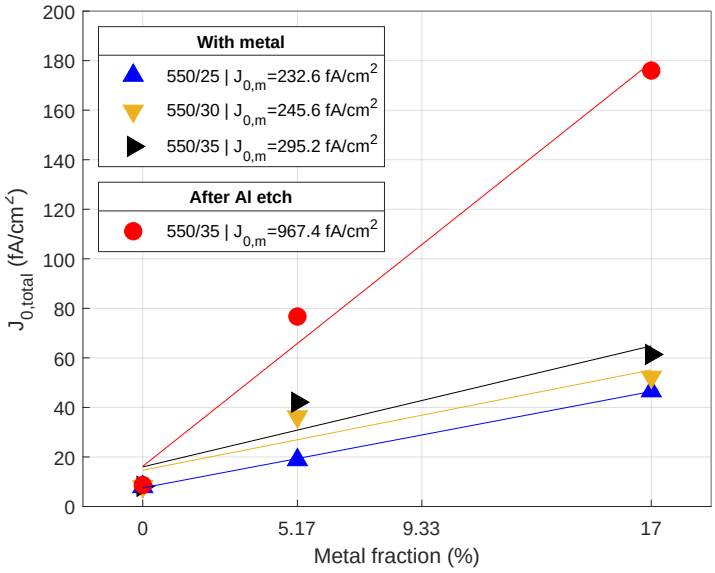

Figure 5.14: Linear fitting of experimental data from sample C2 with NAOS & i-n PECVD poly-SiO_x contacts.

remains constant, which shows that the contact annealing has a negligible impact on these areas. After metal removal, $J_{0,total}$ of the metallized areas increases, showing high values of $J_{0,total}$ for the areas with 5.17% and 17% metal.
The evolution of $J_{0,total}$ of sample C1 is shown in Figure C.4 (Appendix C), which shows a lesser impact of the contact annealing to the metal-induced recombination. Only after many steps of contact annealing, an increase in $J_{0,total}$ was measurable for the metallized areas. However, $J_{0,total}$ of the non-metallized area also increased, pointing to contact degradation. Remarkably, when the metal was removed, $J_{0,total}$ of the 5.17% metallized area decreased below the $J_{0,total}$ of the non-metallized area.

The $J_{0,total}$ of the area with 9.33% metal on sample C2 deviates significantly from the other metallized areas, so this area is left out of the $J_{0,metal}$ calculation. However, the uniformity of the passivation was acceptable, so a correction to $J_{0,total}$ was not needed before the linear fitting of the data. The y-axis crossing of the linear fit was assumed to be an acceptable estimate of $2J_{0,passiv}$, which made the interpretation of the fit parameter more straightforward. Figure 5.14 shows the linear fitting of the $J_{0,metal}$ data from sample C2, which resulted in an increasing slope for increasing contact annealing time. After Al removal, the slope has increased firmly, resulting in a $J_{0,metal}$ of 967.4 $\pm$ 196.8 fA.cm^2. The calculation of $J_{0,metal}$ has resulted in the values noted in Figure 5.14, showing relatively low values for $J_{0,metal}$ before metal removal when compared to the TO & LP- + PECVD poly-Si contacts. However, when the metal is removed, both contacts show similar values for $J_{0,metal}$,
For sample C1, the contact annealing treatments have resulted in a $J_{0,metal}$ of 1243.3 $\pm$ 348.4 fA/cm^2. This value was obtained by fitting the $J_{0,total}$ data after metal removal. As already mentioned, since there are too many uncertainties in the experiment, the comparison of $J_{0,metal}$ values will not lead to conclusions considering the different contact types of contact annealing conditions. However, this measurement method shown to result in the detection of metal-induced recombination in several types of poly-Si based contacts.

5.5. Discussion

As this experiment relies on some assumptions about the fabricated contact, there can be large uncertainties in the determination of $J_{0,metal}$. To tackle uncertainty created by non-uniformity of the passivation in the sample, it is crucial to fabricate poly-Si based contacts that show a high level of uniformity. Depending on the average $J_{0,total}$ of the sample, the acceptable deviation changes. When the uniformity is within acceptable margins, it is also crucial to obtain a reproducible passivation in different samples. This opens the way to investigate and characterise $J_{0,metal}$ in poly-Si contacts.
Following up on the uniformity, the metal fraction can cause uncertainty in the measurement. Before metal deposition, the SiN_x layer is opened with isotropic etching to make contact between the poly-$Si(O_x)$ and the metal (Al). When the underetch of the fingers is too large, it can affect the actual metal fraction on the wafer. This can be solved in two ways. First, the etch time can be optimized to reduce the under etch to several tens of nanometers. Or second, the actual metal fraction on the wafer can be determined by measuring the finger width and spacing. The fitting of the measured $J_{0,total}$ should then be adapted to the right values of F_m.

An more extensive study on the impact of contact annealing on the passivation of non-metallized areas could provide insight to which extent the contact annealing can be performed without damaging the passivation. This subject was addressed in this thesis project, but experiments have shown that this can be different for any type of poly-Si based contact.
It has resulted from the measurements that $J_{0,metal}$ of samples with the metal still on the contact has resulted in lower values than $J_{0,metal}$ of the same samples with the metal removed. It is clear that the metal is affecting the recombination at the interface, but it could not be explained physically from the collected data. Until this can be explained, the best interpretation of metal-induced recombination is achieved by removing the metal after contact annealing. This will ensure there is no external factor influencing the measurement. It will also truly show recombination induced by the metal, meaning passivation degradation of other layers caused by the metal.

The uncertainty in the fitting of $J_{0,metal}$ could also be reduced by fabricating multiple identical samples. Reproducibility will be crucial here, since the absolute values of $J_{0,total}$ are compared to each other. A linear regression through the extracted $J_{0,total}$ values for each metal fraction could become

more accurate to characterise and investigate $J_{0,metal}$.
For future research and further optimization of poly-Si based contacts, it could be useful to investigate if there is any difference in $J_{0,metal}$ between n-type and p-type contacts, which could possibly help to determine is a front junction or a back junction in an FBC solar cell configuration is the most efficient option. Exploring $J_{0,metal}$ for different types of metallization and metals could also be done to characterise this metal-induced recombination.

5.6. Summary

The aim of this experimental section was to test a simple approach to be able to extract the metal-induced recombination ($J_{0,metal}$) in poly-Si based passivating contacts. The method was based on the already existing IV method and PL method [70, 71, 72, 73, 74], which uses a varying metal fraction on poly-Si based passivating contacts to derive the impact of the metal on the total recombination. By fabricating symmetrical sample structures with single-side metallization, the interpretation of the measurements could become more straightforward. The metal fractions chosen for the $J_{0,metal}$ extraction were 0%, 5.17%, 9.33%, 17.0%.
For this experimental section, three types of samples were fabricated, (i) thermal oxide with LP- + PECVD poly-Si, (ii) textured NAOS with i-n PECVD poly-SiO_x and (iii) flat NAOS with i-n PECVD poly-SiO_x. To know the starting point of the samples before metallization, the uniformity of the passivation in the samples was monitored during sample fabrication. Not all samples in the experiment resulted in acceptable uniformity of passivation, but in view of time, the experiment was continued anyway.

The three textured samples with TO/LP- + PECVD poly-Si have shown an improved passivation after metallization. This result was unexpected, but it showed that the metal is influencing the measurement of the passivation quality. The contact annealing did not directly result in an increase of recombination at the metallized areas, but after 20 minutes of annealing at 500^{o}C the dominance of $J_{0,metal}$ became clear from the measurements. From this moment the metal-induced recombination became larger than the influence of the Al on the passivation measurement. $J_{0,metal}$ could be extracted from the linear fit, which resulted in an increase of $J_{0,metal}$ for increasing annealing time for sample A1. However, after removing the metal, the measured $J_{0,metal}$ of sample A1 jumped from 593.2 fA/cm^2 to 968.6 fA/cm^2, which could indicate that the metal is affecting the passivation measurement.
Two textured samples with NAOS/i-n PECVD poly-SiO_x showed a degradation of the passivation after metallization. This degradation was also visible for the non-metallized area, which indicates that the passivation quality is not stable for the fabricated contact structures. The impact of $J_{0,metal}$ was not visible during contact annealing, but after metal removal it became measurable. This resulted in $J_{0,metal}$ values of 401.7 fA/cm^2 and 712.7 fA/cm^2, for sample B1 and B2 respectively. No any characterisation or comparison could not be made wit these values, since the amount of uncertainties in the performed experiments were too many to draw any conclusions.
Two flat samples with NAOS/i-n PECVD poly-SiO_x showed also a decrease of $J_{0,total}$ upon metallization, but for these samples the uniformity of passivation was acceptable. No degradation of the passivated area has been observed during contact annealing, which means that any increase in $J_{0,total}$ could be attributed to metal-induced recombination. $J_{0,metal}$ showed a slight increase for increasing annealing time for sample C2. A similar increase of $J_{0,metal}$ after metal removal is observed for these samples. $J_{0,metal}$ of sample C2 jumped from 295.2 fA/cm^2 to 967.4 fA/cm^2.

It can be concluded that there were many uncertainties in this experiment that need to be resolved to be able to characterise and investigate the metal-induced recombination further. Firstly, a sufficient uniformity and reproducibility of the surface passivation is crucial to compare different parts of a sample and different samples. The metal-fraction should be accurately determined to reduce the uncertainty in the fitting. To investigate a certain contact type, the degradation during the contact annealing should be known or be negligible, so it cannot influence the slope of $J_{0,total}$ vs. F_m.
In future research, it could be interesting to investigate n-type contacts compared to p-type contacts to determine if a front junction or back junction is the best option in a FBC solar cell with double side poly-Si based passivating contacts. The impact of pinholes of the metal-induced recombination could also provide insight into the advantages and disadvantages of pinholes in a poly-Si based contact.

6

Conclusions and Outlook

The main goal of this thesis project was to investigate the impact of thermal treatments on the passivation quality poly-Si based passivating contacts. The approach was based on the concept of pinholes in the interfacial SiO_x layer between the c-Si and doped poly-Si. This thesis project included the introduction of an additional annealing step prior to dopant introduction to separate the pinhole formation from the dopant activation. To confirm the existence of pinholes, this annealing study was backed up by a pinhole detection experiment. Additionally, a novel and simple approach to extract the metal-induced recombination was conceptualised.

6.1. Conclusions

Chapter 3 describes the determination of the pinhole density by anisotropic underetching of the c-Si through pinholes in the SiO_x. The contact structure for the pinhole detection consisted of a flat c-Si wafer with thermal oxide and LPCVD poly-Si layer, which was annealed at temperatures $\geq 1000^oC$. A test experiment has shown that it was possible to detect pinholes with this method. It appeared that the etch time should be chosen carefully, since the etch pit size is dependent on the etch time. Different types of pinholes could affect the etch pit detection, resulting in an under- or overestimation of the actual pinhole density.
The pinhole density measurement for a range of annealing temperatures $\geq 1000^oC$ has resulted in an exponential relation between the pinhole density and the temperature. For the range of 1000-1075^oC, the pinhole density ranged from 10^6-$2{\cdot}10^8$ cm^{-2}. These values are within the optimal range for effective charge carrier transport through pinholes according to literature [24]. The measurements have shown that there exists no specific optimal etch time for pinhole detection, but it depends on the extent of rearrangement of the SiO_x.

Assessing the passivation quality of poly-Si passivating contacts was done by fabricating double-side textured contact structures with thermal oxide and LPCVD poly-Si, capped with SiN_x for hydrogenation. The investigation of the passivation quality in poly-Si passivating contacts was divided into two parts, namely the n-type and p-type contacts.

For n-type contacts, the best passivation was achieved for the sample that was subjected to a combination of 1000^oC pre-annealing and 875/15 post-annealing after hydrogenation. It resulted in iV_{oc} = 729.8 mV and $J_0 = 5.3$ fA/cm^2, which was approaching the state-of-the-art passivation quality [65, 66]. Pre-annealing has shown to have a positive impact on the passivation quality, which resulted in a wide process window for the post-annealing conditions when this pre-annealing was performed. This optimal process window was in the lower thermal diffusion budget range, which is beneficial when trying to minimize excessive in-diffusion of dopants in the bulk. The passivation quality degraded for the samples with 1000^oC post-annealing and/or 1075^oC pre-annealing, which is caused by excessive dopant diffusion into the c-Si. It reduces the field-effect passivation at the SiO_x interface, but also introduces more defects in the surface region of the c-Si, reducing the chemical passivation and increasing Auger recombination.
The shape of the effective lifetime curves has shown that Auger recombination is the dominant recombi-

nation mechanisms in the samples that were subjected to pre-annealing. However, SRH recombination plays a more significant role in the samples without pre-annealing, where the effective lifetime was reduced from >5 ms to below 1 ms. The positive effect of pinholes on the passivation quality in n-type contacts has become clear by these passivation measurements.
The passivation difference between the samples with and without pinholes could be explained by the enhanced field-effect passivation at the pinhole sites. Local in-diffusion of phosphorus through the pinholes increases the internal electric field, which attracts majority carriers and repels minority carriers from the pinhole sites. This idea is in accordance with the dominant Auger recombination that was observed in the samples with pinholes, which scales with the dopant concentration. As long as the pre-annealing treatment does not significantly affect the chemical passivation quality of the SiO_x layer or its related recombination does not dominate the c-Si/SiO_x poly-Si interface recombination, this principle of locally enhanced field-effect passivation could positively affect the passivation quality of the n^+-poly-Si contact.

For p-type contacts, the best passivation was achieved for the sample that was subjected to a combination of 1025^{o}C pre-annealing and 875/30 post-annealing. This resulted in iV_{oc} = 689.1 mV and J_0 = 37.3 fA/cm^2, which was >10 mV lower than state-of-the-art passivation in textured p-type contacts [65, 67]. Pre-annealing has shown to increase the passivation quality, but the influence of the post-annealing conditions was more pronounced. The effective lifetime increased when applying pre-annealing, showing its positive impact on the passivation quality of p-type contacts. The passivation degraded for 1000^{o}C post-annealing, which was caused by a large concentration of diffused boron in the c-Si surface region.
The thermal diffusion budget was a critical parameter in the investigated samples, which determined the excessive in-diffusion of boron into the c-Si. The depth of this in-diffusion was completely dependent on the thermal diffusion budget in the investigated samples, but significant passivation degradation was only measurable for a thermal diffusion budget larger than $6{\cdot}10^{12}$ cm^2. The pinhole density did not show any impact on the dopant diffusion through the SiO_x layer. The experiment has shown that the SiO_x in this experiment is more or less transparent for boron, which stresses the importance of the post-annealing thermal diffusion budget. Pre-annealing showed to positively affect the passivation quality in p^+-poly-Si contacts, but the boron-induced recombination is limiting the passivation quality in the investigated samples.

A new method to extract the metal-induced recombination in poly-Si based passivating contacts was done by fabricating symmetrical contact structures and creating four areas with varying metal fraction. Three different poly-Si based contacts were investigated in the experiment. The method has shown to be able to extract metal-induced recombination, but many improvements are still needed to be able to use this method for characterisation of the metal-induced recombination in poly-Si based passivating contacts.
Monitoring the passivation after metallization and during contacts annealing has shown that the presence of metal on the sample is influencing the passivation measurement. The high conductivity of the metal is believed to affect the photoconductance measurement, resulting in couter-intuitive measurement results for the metallized samples. After a non-specific time of contact annealing at ≥500^{o}C, the metal-induced recombination became dominant, which was measured in the photoconductance measurements. However, after removing the metal, this metal-induced recombination showed to be more pronounced. It is thus expected that the most accurate determination of the metal-induced recombination can be made after removing the metal fingers from the samples.
Samples also showed passivation degradation of the non-metallized area, which was accounted for in the calculation of $J_{0,metal}$. This passivation degradation could be attributed to hydrogen effusion from the poly-Si contact, but a low quality SiO_x/poly-Si stack is believed to be more sensitive to the contact annealing, which could affect the layers and result in a lower passivation quality.
It can be concluded that the experimental method managed to extract the metal-induced recombination in several types of poly-Si based passivating contacts. However, the occurrence of too many uncertainties in the experiment of this work has limited this experimental section to a proof-of-concept, rather than characterising the metal-induced recombination in poly-Si contacts.

6.2. Outlook

This thesis projects has led to some new insights into the interpretation and knowledge about passivation in poly-Si passivating contacts. The experiments have shown that there is still much room for improvement, which could be accelerated by further research into pinholes in the SiO_x, combinations of pre- and post-annealing treatments and metal-induced recombination. This section will briefly assess an outlook for future research into poly-Si passivating contacts.

For future research into pinholes in the interfacial tunnelling oxide of a poly-Si contact, it can be interesting to explore the pinhole density for several different types of oxides. Wet-chemical (NAOS) oxides are also used frequently in poly-Si based passivating contacts, but its stoichiometry and density varies from thermal oxides. This could influence the pinhole density at certain temperature treatments. It will also be extremely useful to explore the pinhole density for varying thickness of the SiO_x layer. As the thickness of the SiO_x increases, the poly-Si contact will depend more on the pinhole transport, increasing their importance.
A study into the impact of pre-annealing on the chemical passivation of the SiO_x could provide insight in how to maintain the chemical passivation of the interface, while still utilizing the advantage of pinholes to enhance the carrier transport. Performing pinhole density measurements after lower temperature annealing treatment (800-1000^{o}C) could reveal the impact of high temperature annealing on the passivation of the SiO_x layer, without forming any pinholes.

The pinhole-enhanced carrier transport in poly-Si passivating contact could be an interesting field of investigation, since it could help to understand the passivation mechanisms at the interface. To be able to conclude anything about the carrier transport in the contact it is essential to determine the contact resistivity of similar contact structures that show a similar passivation quality. The selectivity of the contacts can then be derived, showing the effectivity of the carrier transport at the interface.
To see the performance of both n-type and p-type contacts in a solar cell, the p-type contact will need further optimization that minimizes the boron diffusion into the c-Si bulk. The exploration of a thicker SiO_x layer could be investigated, which is expected to improve the diffusion barrier properties of the SiO_x. Additionally, a pinhole density study is required to determine the pinhole density in a thicker SiO_x. Another method to decrease the in-diffusion of boron is to shorten the post-annealing process, which will reduce the thermal diffusion budget, while still reaching the required temperatures for a-Si crystallization and dopant activation. Rapid Thermal Annealing (RTP) could provide a solution to this challenge.

To be able to use the proposed approach for $J_{0,metal}$ characterisation, several uncertainties need to be tackled. These uncertainties are listed below, which provide the opportunity to characterise $J_{0,metal}$, provided that they are all mitigated.

- Uniformity of the passivation quality: simplifies the analysis and enlarges the reliability of the result
- Actual metal fraction: Determines the actual ratio between metallized and non-metallized surface recombination
- Passivation degradation of passivated areas: Assures that only the metal-induced recombination is assessed
- Metal influence on passivation measurement: Removes any external influence on passivation measurement
- Reprodicibility of contact fabrication: creates the possibility to assess multiple identical samples and perform a linear regression with smaller fitting uncertainty

Tackling the uniformity and reproducibility could be done by optimizing process recipes, concerning the poly-Si(O_x) depositions. This creates the opportunity to characterise $J_{0,metal}$ of poly-Si based contacts for certain contact configurations. Exploring $J_{0,metal}$ in n-type and p-type contact can open the discussion to use either a front or back junction in a double-side poly-Si contacted solar cell. Furthermore, the impact of pinholes in the SiO_x on $J_{0,metal}$ can be investigated.

Appendix A: Procedure for pinhole density measurement

The pinhole density was determined by taking three regions of interest (ROIs) from every sample and averaging this to rule out a large uncertainty in the choice of ROI. For each specific etch time and annealing temperature, three ROIs were taken, so eventually 9 ROIs are considered for each annealing temperature.
Since the pinhole density differs by two orders of magnitude, the size of the ROI is different for each annealing temperature. As shown in Figure A.1, the ROIs cover 1600 μm^2, 900 μm^2, 400 μm^2, 200 μm^2 for 1000^{o}C, 1025^{o}C, 1050^{o}C, 1075^{o}C, respectively.

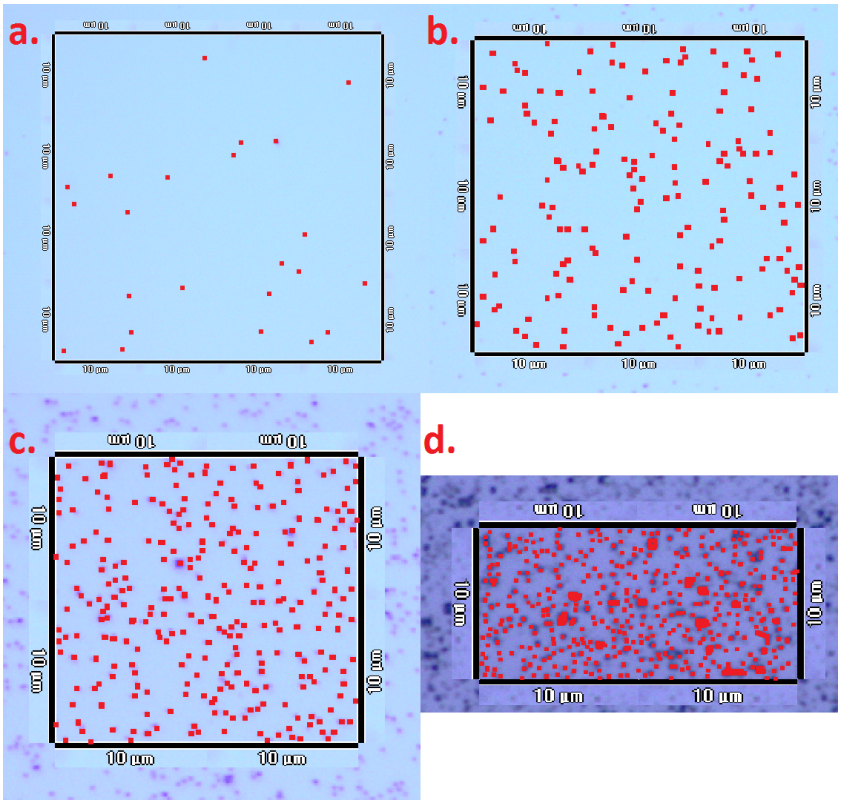

Figure A.1: ROIs for the different annealing temperatures: (a.) 1000^{o}C, (b.) 1025^{o}C, (c.) 1050^{o}C, (d.) 1075^{o}C.

B

Appendix B: J_0 of ion implanted poly-Si contacts

B.1. N-type poly-Si contacts

Figure B.1 provides the measured J_0 that corresponds with the values of iV_{oc} that are presented in Figure 4.3.

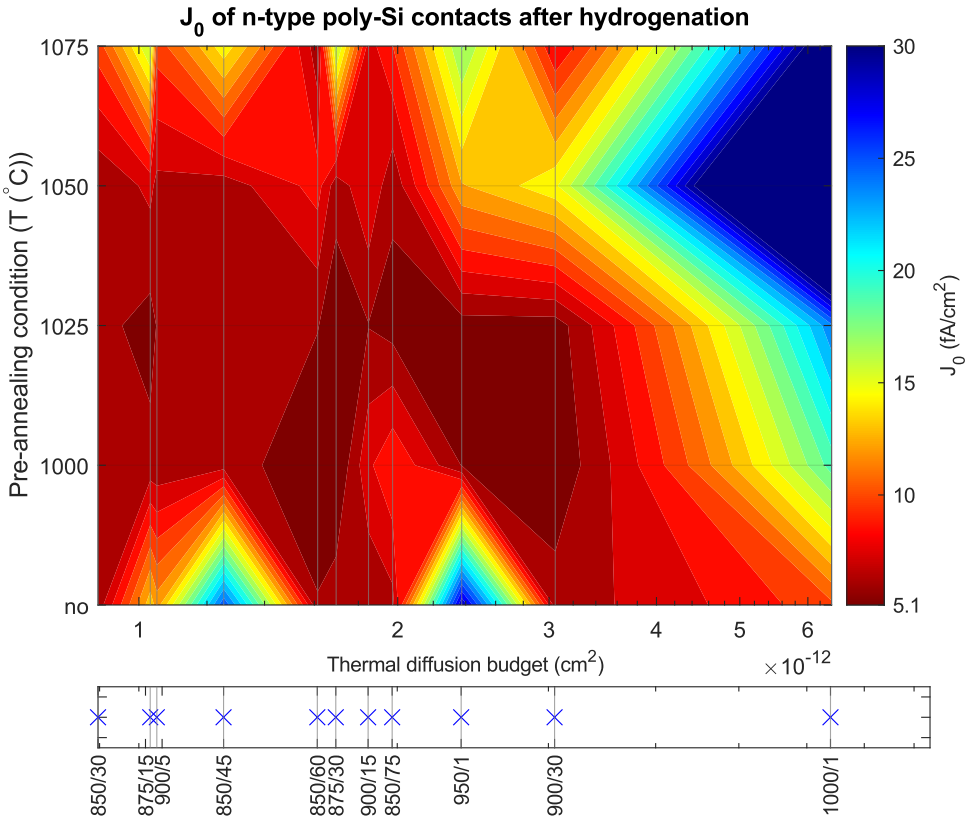

Figure B.1: Passivation quality in terms of J_0 of the phosphorus-doped poly-Si based passivating contacts. Post-annealing conditions are compared by the thermal diffusion budget on the x-axis.

B.2. P-type poly-Si contacts

Figure B.2 provides the measured J_0 that corresponds with the values of iV_{oc} that are presented in Figure 4.8.

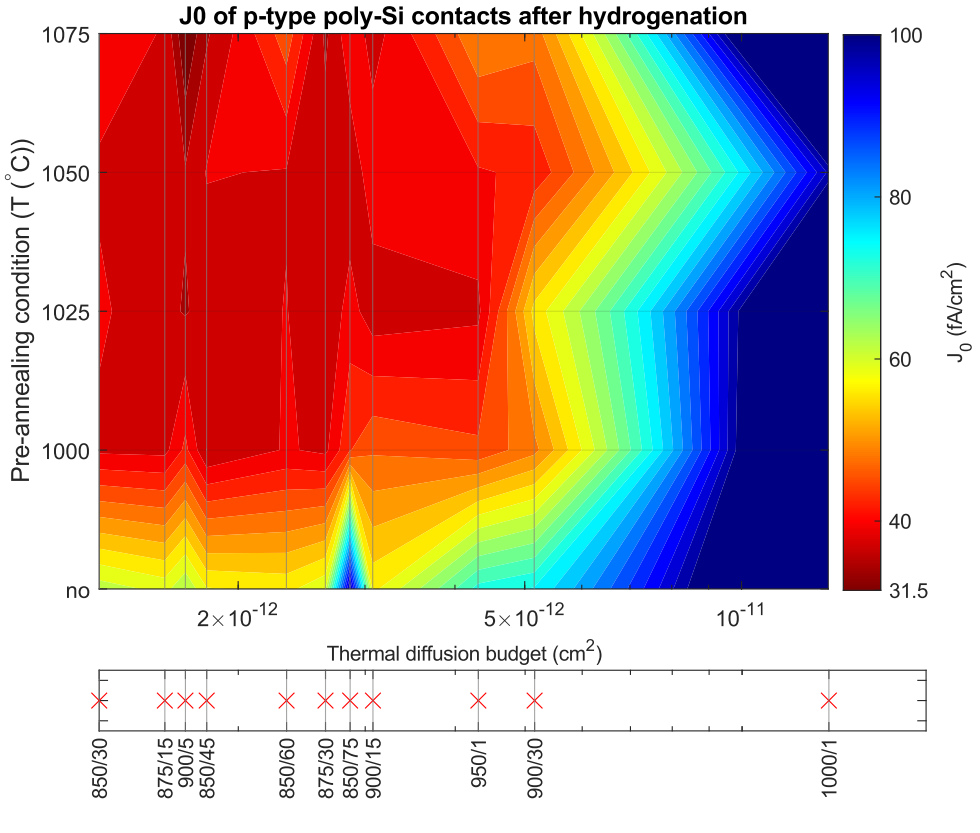

Figure B.2: Passivation quality in terms of J_0 of the boron-doped poly-Si based passivating contacts. Post-annealing conditions are compared by the thermal diffusion budget on the x-axis.

Appendix C: $J_{0,total}$ evolution during contact nnealing

C.1. Evolution of $J_{0,total}$ during contact annealing

The following figures show the evolution of the measured $J_{0,total}$ during contact annealing of the samples that were not highlighted in Chapter 'Extraction of metal-induced recombination of poly-Si based passivating contacts'. Figure C.1 and C.2 show the results from the textured TO & LP- + PECVD contact batch, sample A2 and A3 respectively. Figure C.3 presents the evolution of $J_{0,total}$ in sample B1 from the textured i-n PECVD contact batch. Finally, Figure C.4 shows the results of sample C1 from the flat i-n PECVD contact batch. Remarkable results are discussed in Chapter 'Extraction of metal-induced recombination of poly-Si based passivating contacts'.

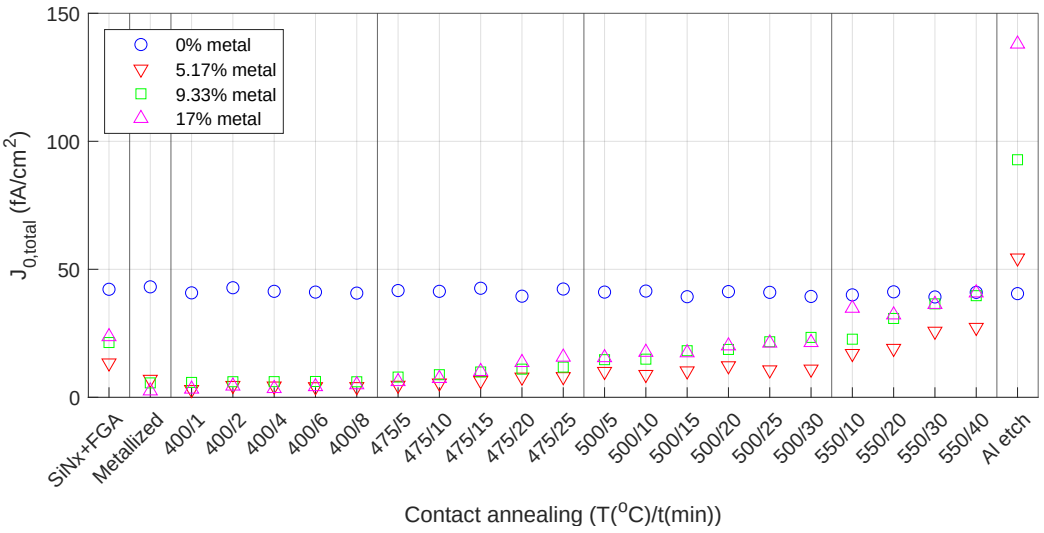

Figure C.1: Evolution of $J_{0,total}$ in sample A2 of the textured TO & LP- + PECVD contact batch.

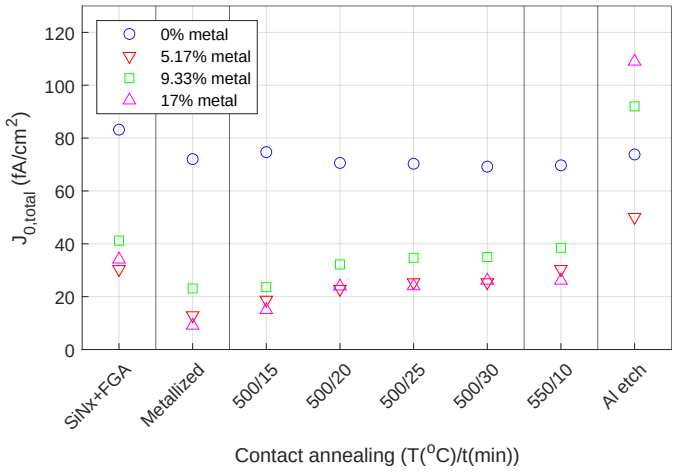

Figure C.2: Evolution of $J_{0,total}$ in sample A3 of the textured TO & LP- + PECVD contact batch.

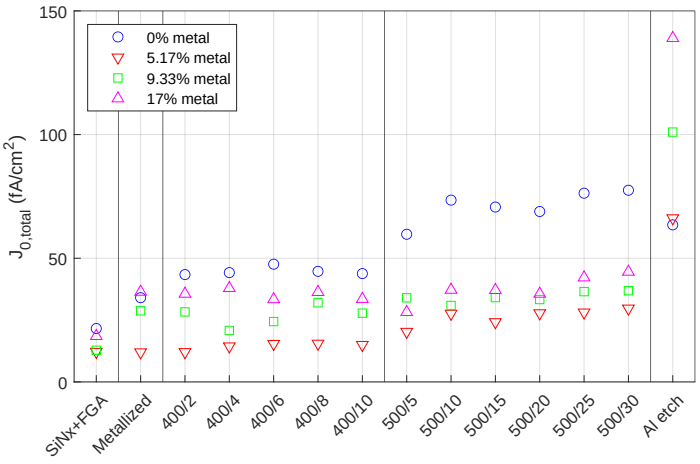

Figure C.3: Evolution of $J_{0,total}$ in sample B1 of the textured NAOS/i-n PECVD contact batch.

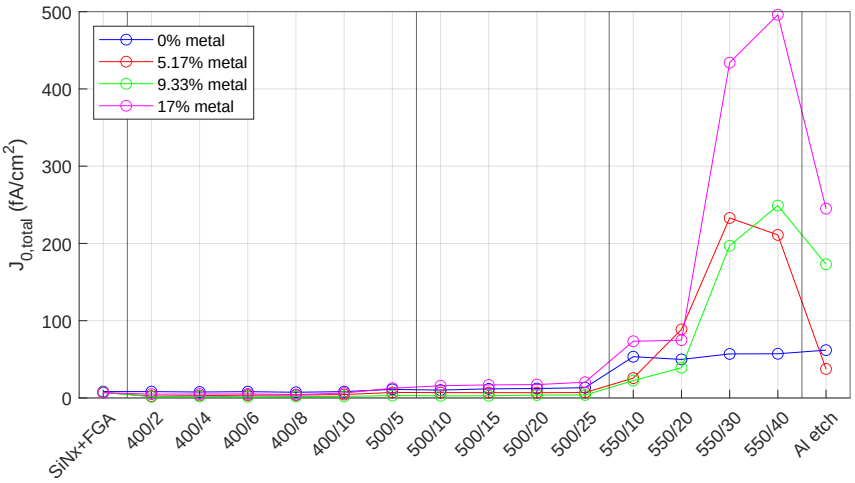

Figure C.4: Evolution of $J_{0,total}$ in sample C1 of the flat NAOS/i-n PECVD contact batch.

C.2. Linear fitting of experimental data

This section provides the additional fit curves of the investigated samples in Chapter 'Extraction of metal-induced recombination in poly-Si passivating contacts'. Figure C.5 shows the linear fitting of samples A2 and A3 with thermal oxide and LP- + PECVD poly-Si contacts (textured). Figure C.6 shows the linear fitting of sample C1 with a flat NAOS and i-n PECVD poly-SiO$_x$ stack, on a flat surface.

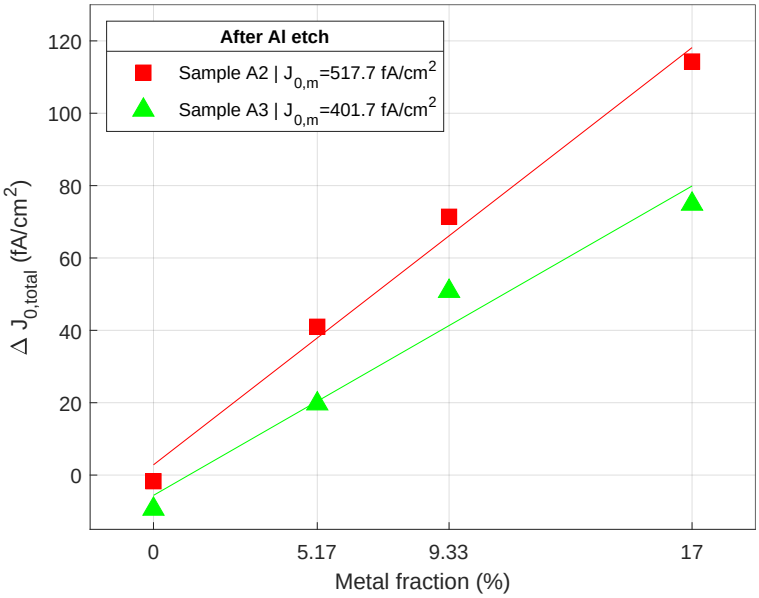

Figure C.5: Linear fitting through the experimental data from samples A2 and A3 from the textured TO & LP- + PECVD contact batch. For both samples, the data represents the corrected $J_{0,total}$ after metal removal.

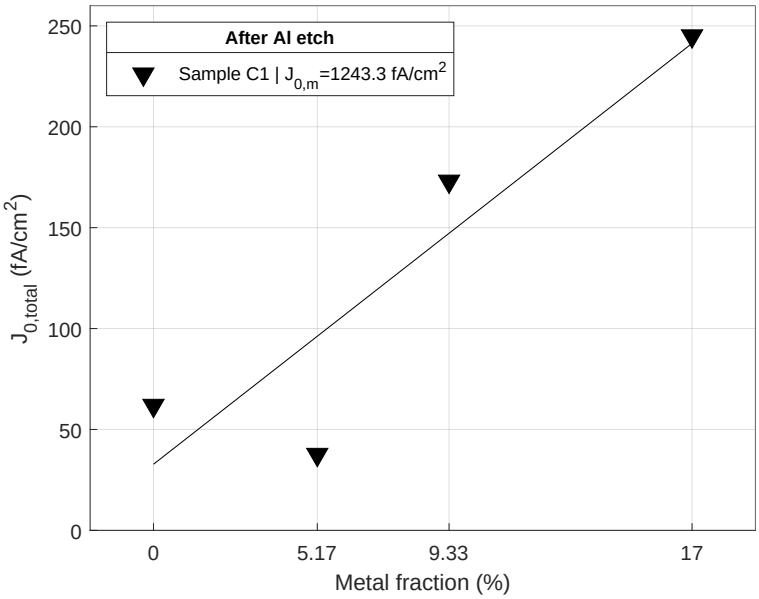

Figure C.6: Linear fitting through the experimental data from sample C1 from the flat NAOS/i-n PECVD contact batch. The data point represent the measured $J_{0,total}$ after metal removal.

C.3. Uncertainty of $J_{0,metal}$

When fitting through data points, an error always exists between the data points and the fit. This error can be defined in many ways, such as the standard deviation, standard error, variance and, for example, the confidence interval.
The fitting method that is used, relies on creating a function $y = ax + b$, where y is $J_{0,total}$ (or $\Delta J_{0,total}$), x is F_m and a and b are the fitting parameters. The fitting is based on obtaining the least squared deviation (ε^2) from each data point, also referred to as linear regression [80]. This simple linear regression is based on minimizing the sum of all squared errors ($Q(a,b)$) as defined in equation C.1.

$$Q(a,b) = \sum_{i=1}^{n} \varepsilon_i^2 = \sum_{i=1}^{n} (y_i - b - ax_i) \tag{C.1}$$

To fit through the data points, the model $polyfit$ in MATLAB [81] is used, which returns the values for a and b, with the corresponding deviation from the data points. The deviation is then converted to the standard error, calculated with equation C.2 [82].

$$SE = \frac{\sigma}{\sqrt{n}} \tag{C.2}$$

Here, σ is the standard deviation of the data points to the fit and n is the amount of data points. This standard error is interpreted as described in Figure C.7, where the standard error of the fit is shown as a confidence interval of the linear curve. From this interval, the relative uncertainty in the slope (a) can be determined. This approach was used to determine the uncertainty in $J_{0,metal}$, which was thus dependent on the goodness of the fit.

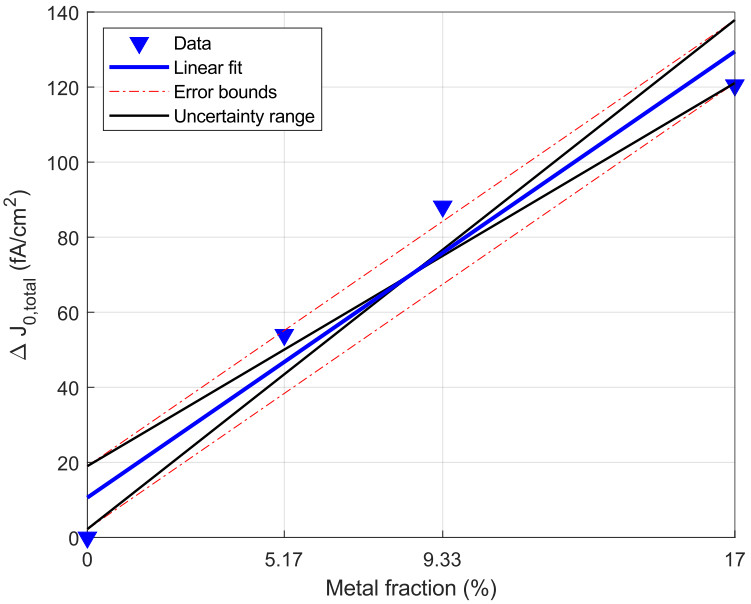

Figure C.7: Representation of the interpretation of the uncertainty in the slope of the linear fit that determines $J_{0,metal}$. The black lines represent the maximum deviation from the fitted slope.

Bibliography

[1] International Energy Agency, "Global Energy Review 2021," 2021.

[2] S. Philipps and W. Warmuth, "Photovoltaics Report Fraunhofer ISE," Fraunhofer Institute for Solar Energy Systems ISE, Freiburg im Breisgau, Germany., 2021.

[3] K. Yoshikawa, W. Yoshida, T. Irie, H. Kawasaki, K. Konishi, H. Ishibashi, T. Asatani, D. Adachi, M. Kanematsu, H. Uzu, et al., "Exceeding conversion efficiency of 26% by heterojunction interdigitated back contact solar cell with thin film Si technology," Solar Energy Materials and Solar Cells, vol. 173, pp. 37–42, 2017.

[4] M. Green, E. Dunlop, J. Hohl-Ebinger, M. Yoshita, N. Kopidakis, and X. Hao, "Solar cell efficiency tables (version 57)," Progress in photovoltaics: research and applications, vol. 29, no. 1, pp. 3–15, 2021.

[5] Y. Chen, D. Chen, C. Liu, Z. Wang, Y. Zou, Y. He, Y. Wang, L. Yuan, J. Gong, W. Lin, et al., "Mass production of industrial tunnel oxide passivated contacts (i-TOPCon) silicon solar cells with average efficiency over 23% and modules over 345 W," Progress in Photovoltaics: Research and Applications, vol. 27, no. 10, pp. 827–834, 2019.

[6] A. H. Smets, K. Jäger, O. Isabella, R. A. Swaaij, and M. Zeman, Solar Energy: The physics and engineering of photovoltaic conversion, technologies and systems. UIT Cambridge, 2015.

[7] M. Fedkin and J. A. Dutton, "P-N Junction," 2020. Accessed on 05-11-2021: https://www.e-education.psu.edu/eme812/node/606.

[8] A. Abass, Light absorption enhancement and electronic properties of thin-film solar cells. PhD thesis, Ghent University, 2014.

[9] B. Nemeth, D. L. Young, H.-C. Yuan, V. LaSalvia, A. G. Norman, M. Page, B. G. Lee, and P. Stradins, "Low temperature Si/SiO x/pc-Si passivated contacts to n-type Si solar cells," in 2014 IEEE 40th Photovoltaic Specialist Conference (PVSC), pp. 3448–3452, IEEE, 2014.

[10] Y. Zhao, "Contact Stack Evaluation for SHJ Solar Cells and Process Development of IBC-SHJ Solar Cells," 2018.

[11] A. J. Hof, Deuterium in the gate dielectric of CMOS devices. PhD thesis, Ph. D. dissertation, Universiteit Twente, Netherlands, 2004.

[12] B. Zhang, Y. Yao, R. Patterson, S. Shrestha, M. Green, and G. Conibeer, "Electrical properties of conductive Ge nanocrystal thin films fabricated by low temperature in-situ growth," Nanotechnology, vol. 22, no. 12, p. 125204, 2011.

[13] B. W. van de Loo, B. Macco, M. Schnabel, M. K. Stodolny, A. A. Mewe, D. L. Young, W. Nemeth, P. Stradins, and W. M. Kessels, "On the hydrogenation of Poly-Si passivating contacts by Al_2O_3 and SiN_x thin films," Solar Energy Materials and Solar Cells, vol. 215, p. 110592, 2020.

[14] J. Melskens, B. W. van de Loo, B. Macco, L. E. Black, S. Smit, and W. Kessels, "Passivating contacts for crystalline silicon solar cells: From concepts and materials to prospects," IEEE Journal of Photovoltaics, vol. 8, no. 2, pp. 373–388, 2018.

[15] R. Preu, E. Lohmüller, S. Lohmüller, P. Saint-Cast, and J. M. Greulich, "Passivated emitter and rear cell—Devices, technology, and modeling," Applied Physics Reviews, vol. 7, no. 4, p. 041315, 2020.

[16] P. Stradins, S. Essig, W. Nemeth, B. Lee, D. Young, A. Norman, Y. Liu, J.-W. Luo, E. Warren, A. Dameron, et al., "Passivated tunneling contacts to n-type wafer silicon and their implementation into high performance solar cells," tech. rep., National Renewable Energy Lab.(NREL), Golden, CO (United States), 2014.

[17] Y. Tao, V. Upadhyaya, C.-W. Chen, A. Payne, E. L. Chang, A. Upadhyaya, and A. Rohatgi, "Large area tunnel oxide passivated rear contact n-type Si solar cells with 21.2% efficiency," Progress in Photovoltaics: Research and Applications, vol. 24, no. 6, pp. 830–835, 2016.

[18] Z. C. Holman, S. De Wolf, and C. Ballif, "Improving metal reflectors by suppressing surface plasmon polaritons: a priori calculation of the internal reflectance of a solar cell," Light: Science & Applications, vol. 2, no. 10, pp. e106–e106, 2013.

[19] R. Chen, M. Wright, D. Chen, J. Yang, P. Zheng, X. Zhang, S. Wenham, and A. Ciesla, "24.58% efficient commercial n-type silicon solar cells with hydrogenation," Progress in Photovoltaics: Research and Applications, vol. 29, no. 11, pp. 1213–1218, 2021.

[20] F. Feldmann, C. Reichel, R. Müller, and M. Hermle, "The application of poly-Si/SiO_x contacts as passivated top/rear contacts in Si solar cells," Solar Energy Materials and Solar Cells, vol. 159, pp. 265–271, 2017.

[21] M. F. Vos, B. Macco, N. F. Thissen, A. A. Bol, and W. Kessels, "Atomic layer deposition of molybdenum oxide from (NtBu)2(NMe_2)$_2$Mo and O_2 plasma," Journal of Vacuum Science & Technology A: Vacuum, Surfaces, and Films, vol. 34, no. 1, p. 01A103, 2016.

[22] R. Peibst, U. Römer, Y. Larionova, M. Rienäcker, A. Merkle, N. Folchert, S. Reiter, M. Turcu, B. Min, J. Krügener, et al., "Working principle of carrier selective poly-Si/c-Si junctions: Is tunnelling the whole story?," Solar Energy Materials and Solar Cells, vol. 158, pp. 60–67, 2016.

[23] Y. Zeng, H. Tong, C. Quan, L. Cai, Z. Yang, K. Chen, Z. Yuan, C.-H. Wu, B. Yan, P. Gao, et al., "Theoretical exploration towards high-efficiency tunnel oxide passivated carrier-selective contacts (TOPCon) solar cells," Solar Energy, vol. 155, pp. 654–660, 2017.

[24] T. Wietler, D. Tetzlaff, J. Krügener, M. Rienäcker, F. Haase, Y. Larionova, R. Brendel, and R. Peibst, "Pinhole density and contact resistivity of carrier selective junctions with polycrystalline silicon on oxide," Applied Physics Letters, vol. 110, no. 25, p. 253902, 2017.

[25] K. Lancaster, S. Großer, F. Feldmann, V. Naumann, and C. Hagendorf, "Study of pinhole conductivity at passivated carrier-selected contacts of silicon solar cells," Energy Procedia, vol. 92, pp. 116–121, 2016.

[26] A. S. Kale, W. Nemeth, S. U. Nanayakkara, H. Guthrey, M. Page, M. Al-Jassim, S. Agarwal, and P. Stradins, "Tunneling or Pinholes: Understanding the Transport Mechanisms in SiO_x Based Passivated Contacts for High-Efficiency Silicon Solar Cells," in 2018 IEEE 7th World Conference on Photovoltaic Energy Conversion (WCPEC)(A Joint Conference of 45th IEEE PVSC, 28th PVSEC & 34th EU PVSEC), pp. 3473–3476, IEEE, 2018.

[27] J. Christensen, H. H. Radamson, A. Y. Kuznetsov, and B. Svensson, "Phosphorus and boron diffusion in silicon under equilibrium conditions," Applied physics letters, vol. 82, no. 14, pp. 2254–2256, 2003.

[28] J.-I. Polzin, S. Lange, S. Richter, A. Moldovan, M. Bivour, C. Hagendorf, M. Hermle, S. W. Glunz, and F. Feldmann, "Temperature-induced stoichiometric changes in thermally grown interfacial oxide in tunnel-oxide passivating contacts," Solar Energy Materials and Solar Cells, vol. 218, p. 110713, 2020.

[29] J. S. You, D. Kim, J. Y. Huh, H. J. Park, J. J. Pak, and C. S. Kang, "Experiments on anisotropic etching of Si in TMAH," Solar energy materials and solar cells, vol. 66, no. 1-4, pp. 37–44, 2001.

[30] H. Kobayashi Asuha, O. Maida, M. Takahashi, and H. Iwasa, "Nitric acid oxidation of Si to form ultrathin silicon dioxide layers with a low leakage current density," Journal of Applied Physics, vol. 94, no. 11, pp. 7328–7335, 2003.

[31] L. Filipovic, Topography simulation of novel processing techniques. PhD thesis, 2012.

[32] H. Proksche, G. Nagorsen, and D. Ross, "The Influence of NH_4F on the Etch Rates of Undoped SiO_2 in Buffered Oxide Etch," Journal of the Electrochemical Society, vol. 139, no. 2, p. 521, 1992.

[33] L. Fesquet, S. Olibet, J. Damon-Lacoste, S. De Wolf, A. Hessler-Wyser, C. Monachon, and C. Ballif, "Modification of textured silicon wafer surface morphology for fabrication of heterojunction solar cell with open circuit voltage over 700 mV," in 2009 34th IEEE Photovoltaic Specialists Conference (PVSC), pp. 000754–000758, IEEE, 2009.

[34] L. Geerligs, M. Stodolny, Y. Wu, G. Janssen, I. Romijn, M. Lenes, and J.-M. Luchies, "LPCVD polysilicon passivating contacts for crystalline silicon solar cells," Solar Energy, vol. 2017, p. 2016, 2018.

[35] G. Yang, A. Ingenito, N. van Hameren, O. Isabella, and M. Zeman, "Design and application of ion-implanted polySi passivating contacts for interdigitated back contact c-Si solar cells," Applied Physics Letters, vol. 108, no. 3, p. 033903, 2016.

[36] D. Yan, A. Cuevas, J. Bullock, Y. Wan, and C. Samundsett, "Phosphorus-diffused polysilicon contacts for solar cells," Solar Energy Materials and Solar Cells, vol. 142, pp. 75–82, 2015.

[37] S. Gates and S. Kulkarni, "Kinetics of surface reactions in very low-pressure chemical vapor deposition of Si from SiH_4," Applied physics letters, vol. 58, no. 25, pp. 2963–2965, 1991.

[38] J. Melskens, "Optimisation of a protocrystalline hydrogenated amorphous silicon top solar cell for highest stabilised efficiency," 2007.

[39] MKS Instruments, "Ion Implantation". United States, 2021.

[40] Z. Asalieh, "High energy yield Bifacial-IBC solar cells enabled by poly-SiO_x carrier selective passivating contacts," 2021.

[41] K. Lucas, S. Postnikov, C. Henderson, and S. Hector, "Lithography: Concepts, Challenges and Prospects," in Nano and Giga Challenges in Microelectronics, pp. 69–128, Elsevier, 2003.

[42] T. Awan, A. Bashir, A. Tehseen, and T. E. Orders, "Chemistry of Nanomaterials," 2004.

[43] PROVAC GmbH, PRO 500/1000 High Vacuum PVD Coating System, 2021. Infosheet.

[44] R. A. Sinton and A. Cuevas, "Contactless determination of current–voltage characteristics and minority-carrier lifetimes in semiconductors from quasi-steady-state photoconductance data," Applied Physics Letters, vol. 69, no. 17, pp. 2510–2512, 1996.

[45] R. A. Sinton, A. Cuevas, and M. Stuckings, "Quasi-steady-state photoconductance, a new method for solar cell material and device characterization," in Conference Record of the Twenty Fifth IEEE Photovoltaic Specialists Conference-1996, pp. 457–460, IEEE, 1996.

[46] H. Haug, "New methods for investigation of surface passivation layers for crystalline silicon solar cells," 2014.

[47] D. Kane and R. Swanson, "Measurement of the emitter saturation current by a contactless photoconductivity decay method," in IEEE photovoltaic specialists conference. 18, pp. 578–583, 1985.

[48] A. Cuevas and D. Macdonald, "Measuring and interpreting the lifetime of silicon wafers," Solar Energy, vol. 76, no. 1-3, pp. 255–262, 2004.

[49] E. Peiner, A. Schlachetzki, and D. Krüger, "Doping profile analysis in Si by electrochemical capacitance-voltage measurements," Journal of the Electrochemical Society, vol. 142, no. 2, p. 576, 1995.

[50] Probion Analysis, "Electrochemical CV-Profiling," 2020. Accessed on 16-09-2021: https://probion.fr/ecv-en/.

[51] WEP, “Wafer Profiler CVP21: ECV Measurement of Doping Profiles,” 2019. Datasheet.

[52] R. Rottenfusser, E. E. Wilson, and M. W. Davidson, ”Education in Microscopy and Digital Imaging”. Carl Zeiss, Germany, 2021.

[53] Y. Smith, ”Optical Microscopy Techniques”. AZoNetwork, 2018.

[54] J. A. Woollam Co., ”Ellipsometry FAQ”. United States, 2021.

[55] Y. Huang, M. Liao, Z. Wang, X. Guo, C. Jiang, Q. Yang, Z. Yuan, D. Huang, J. Yang, X. Zhang, et al., “Ultrathin silicon oxide prepared by in-line plasma-assisted N_2O oxidation (PANO) and the application for n-type polysilicon passivated contact,” Solar Energy Materials and Solar Cells, vol. 208, p. 110389, 2020.

[56] H. Guthrey, C. Lima Salles, A. S. Kale, W. Nemeth, M. Page, S. Agarwal, D. L. Young, M. Al-Jassim, and P. Stradins, “Effect of Surface Texture on Pinhole Formation in SiO_x-Based Passivated Contacts for High-Performance Silicon Solar Cells,” ACS Applied Materials & Interfaces, vol. 12, no. 50, pp. 55737–55745, 2020.

[57] C. L. Salles, H. Guthrey, V. LaSalvia, W. Nemeth, M. Page, S. Theingi, D. L. Young, S. Agarwal, and P. Stradins, “Pinhole formation in poly-Si/SiO_x passivating contacts on Si(111)-oriented textures,” in 2020 47th IEEE Photovoltaic Specialists Conference (PVSC), pp. 0736–0738, 2020.

[58] D. Tetzlaff, J. Krügener, Y. Larionova, S. Reiter, M. Turcu, F. Haase, R. Brendel, R. Peibst, U. Höhne, J.-D. Kähler, et al., “A simple method for pinhole detection in carrier selective POLO-junctions for high efficiency silicon solar cells,” Solar Energy Materials and Solar Cells, vol. 173, pp. 106–110, 2017.

[59] F. Feldmann, G. Nogay, J.-I. Polzin, B. Steinhauser, A. Richter, A. Fell, C. Schmiga, M. Hermle, and S. W. Glunz, “A study on the charge carrier transport of passivating contacts,” IEEE Journal of Photovoltaics, vol. 8, no. 6, pp. 1503–1509, 2018.

[60] MicroChemicals GmbH, “Wet chemical etcing of silicon and SiO_2,” 2017.

[61] J. O. Borland, “Low Temperature Activation of Ion Implanted Dopants: A Review,” in Extended Abstracts of the Third International Workshop on Junction Technology, 2002. IWJT., pp. 85–88, IEEE, 2002.

[62] F. Feldmann, J. Schoen, J. Niess, W. Lerch, and M. Hermle, “Studying dopant diffusion from poly-Si passivating contacts,” Solar Energy Materials and Solar Cells, vol. 200, p. 109978, 2019.

[63] R. Regner, “An analytical approach to quantify the thermal budget in consideration of consecutive thermal process steps,” in 10th IEEE International Conference of Advanced Thermal Processing of Semiconductors, pp. 15–20, IEEE, 2002.

[64] Integrated Microfabrication Lab, Diffused Ion Implantation Profile Calculator. Bringham Young University, 2021.

[65] A. Mewe, M. Stodolny, J. Anker, M. Lenes, X. Pagès, Y. Wu, K. Tool, B. Geerligs, and I. Romijn, “Full wafer size IBC cell with polysilicon passivating contacts,” in AIP Conference Proceedings, vol. 1999, p. 040014, AIP Publishing LLC, 2018.

[66] M. Stodolny, M. Lenes, Y. Wu, G. Janssen, I. Romijn, J. Luchies, and L. Geerligs, “n-Type polysilicon passivating contact for industrial bifacial n-type solar cells,” Solar Energy Materials and Solar Cells, vol. 158, pp. 24–28, 2016.

[67] M. Stodolny, J. Anker, C. Tool, M. Koppes, A. Mewe, P. Manshanden, M. Lenes, and I. Romijn, “Novel schemes of P+ poly-Si hydrogenation implemented in industrial 6 bifacial front-and-rear passivating contacts solar cells,” in International Conference EU PVSEC for Photovoltaic Research, Brussels, Belgium, pp. 24–28, 2018.

[68] J. Schmidt, R. Peibst, and R. Brendel, “Surface passivation of crystalline silicon solar cells: Present and future,” Solar Energy Materials and Solar Cells, vol. 187, pp. 39–54, 2018.

[69] M. K. Stodolny, J. Anker, B. L. Geerligs, G. J. Janssen, B. W. Van De Loo, J. Melskens, R. Santbergen, O. Isabella, J. Schmitz, M. Lenes, et al., "Material properties of LPCVD processed n-type polysilicon passivating contacts and its application in PERPoly industrial bifacial solar cells," Energy Procedia, vol. 124, pp. 635–642, 2017.

[70] C. Comparotto, J. Theobald, J. Lossen, and V. D. Mihailetchi, "Understanding contact formation on n-PERT-RJ solar cells," in Proc. 33rd Eur. Photovolt. Sol. Energy Conf. Exhib., pp. 832–836, 2017.

[71] T. Fellmeth, A. Born, A. Kimmerle, F. Clement, D. Biro, and R. Preu, "Recombination at metal-emitter interfaces of front contact technologies for highly efficient silicon solar cells," Energy Procedia, vol. 8, pp. 115–121, 2011.

[72] D. Inns and D. Poplavskyy, "Measurement of metal induced recombination in solar cells," in 2015 IEEE 42nd Photovoltaic Specialist Conference (PVSC), pp. 1–4, IEEE, 2015.

[73] V. Shanmugam, T. Mueller, A. G. Aberle, and J. Wong, "Determination of metal contact recombination parameters for silicon wafer solar cells by photoluminescence imaging," Solar Energy, vol. 118, pp. 20–27, 2015.

[74] R. Hoenig, M. Glatthaar, F. Clement, J. Greulich, J. Wilde, and D. Biro, "New measurement method for the investigation of space charge region recombination losses induced by the metallization of silicon solar cells," Energy Procedia, vol. 8, pp. 694–699, 2011.

[75] H. E. Çiftpınar, M. K. Stodolny, Y. Wu, G. J. Janssen, J. Löffler, J. Schmitz, M. Lenes, J.-M. Luchies, and L. Geerligs, "Study of screen printed metallization for polysilicon based passivating contacts," Energy Procedia, vol. 124, pp. 851–861, 2017.

[76] V. D. Mihailetchi, H. Chu, and R. Kopecek, "Insight into metal induced recombination losses and contact resistance in industrial silicon solar cells," in 2018 IEEE 7th World Conference on Photovoltaic Energy Conversion (WCPEC)(A Joint Conference of 45th IEEE PVSC, 28th PVSEC & 34th EU PVSEC), pp. 2673–2677, IEEE, 2018.

[77] P. Padhamnath, J. Wong, B. Nagarajan, J. K. Buatis, L. M. Ortega, N. Nandakumar, A. Khanna, V. Shanmugam, and S. Duttagupta, "Metal contact recombination in monoPoly solar cells with screen-printed & fire-through contacts," Solar Energy Materials and Solar Cells, vol. 192, pp. 109–116, 2019.

[78] A. Chaudhary, J. Hoß, J. Lossen, R. van Swaaij, and M. Zeman, "Screen printed Ag contacts for n-type polysilicon passivated contacts," in AIP Conference Proceedings, vol. 2147, p. 040002, AIP Publishing LLC, 2019.

[79] A. Chaudhary, J. Hoß, J. Lossen, R. van Swaaij, and M. Zeman, "Advancement in screen printed fire through silver paste metallisation of polysilicon based passivating contacts," in AIP Conference Proceedings, vol. 2367, p. 020003, AIP Publishing LLC, 2021.

[80] J. F. Kenney and E. Keeping, "Linear regression and correlation," Mathematics of statistics, vol. 1, pp. 252–285, 1962.

[81] The MathWorks Inc., Natick, Massachussetts, Matlab, v. r2020a ed., 2010.

[82] D. G. Altman and J. M. Bland, "Standard deviations and standard errors," Bmj, vol. 331, no. 7521, p. 903, 2005.